BRNO UNIVERSITY OF TECHNOLOGY
VYSOKÉ UČENÍ TECHNICKÉ V BRNĚ

FACULTY OF MECHANICAL ENGINEERING
INSTITUTE OF PHYSICAL ENGINEERING

FAKULTA STROJNÍHO INŽENÝRSTVÍ
ÚSTAV FYZIKÁLNÍHO INŽENÝRSTVÍ

CHARACTERIZATION OF MAGNETIC NANOSTRUCTURES BY MAGNETIC FORCE MICROSCOPY

MASTER'S THESIS
DIPLOMOVÁ PRÁCE

AUTHOR   Bc. MICHAL STAŇO
AUTOR PRÁCE

BRNO 2014

BRNO UNIVERSITY OF TECHNOLOGY
VYSOKÉ UČENÍ TECHNICKÉ V BRNĚ

FACULTY OF MECHANICAL ENGINEERING
INSTITUTE OF PHYSICAL ENGINEERING

FAKULTA STROJNÍHO INŽENÝRSTVÍ
ÚSTAV FYZIKÁLNÍHO INŽENÝRSTVÍ

CHARACTERIZATION OF MAGNETIC NANOSTRUCTURES BY MAGNETIC FORCE MICROSCOPY
CHARAKTERIZACE MAGNETICKÝCH NANOSTRUKTUR POMOCÍ MIKROSKOPIE MAGNETICKÝCH SIL

MASTER'S THESIS
DIPLOMOVÁ PRÁCE

AUTHOR   Bc. MICHAL STAŇO
AUTOR PRÁCE

SUPERVISOR   Ing. MICHAL URBÁNEK, Ph.D.
VEDOUCÍ PRÁCE

BRNO 2014

Vysoké učení technické v Brně, Fakulta strojního inženýrství

Ústav fyzikálního inženýrství
Akademický rok: 2013/2014

ZADÁNÍ DIPLOMOVÉ PRÁCE

student(ka): Bc. Michal Staňo

který/která studuje v **magisterském navazujícím studijním programu**

obor: **Fyzikální inženýrství a nanotechnologie (3901T043)**

Ředitel ústavu Vám v souladu se zákonem č.111/1998 o vysokých školách a se Studijním a zkušebním řádem VUT v Brně určuje následující téma diplomové práce:

Charakterizace magnetických nanostruktur pomocí mikroskopie magnetických sil

v anglickém jazyce:

Characterization of magnetic nanostructures by magnetic force microscopy

Stručná charakteristika problematiky úkolu:

Současný výzkum v oblasti magnetismu zažívá bouřlivý vývoj zejména díky rozvoji mikro- a nanolitografických metod, kterými je možné vytvářet nanostruktury s novými vlastnostmi. Pro jejich studium je zapotřebí zvládnutí vhodných metod, pro pozorování rozložení magnetizace. Jednou z nejpoužívanějších metod je mikroskopie magnetických sil (MFM). Tématem diplomové práce je vývoj sond vhodných pro zobrazování magnetizace v magneticky měkkých nanostrukturách.

Cíle diplomové práce:

Proveďte rešeršní studii k problematice měření nanostruktur z magneticky měkkých materiálů pomocí MFM.

Připravte sérii MFM sond s nízkým magnetickým momentem pomocí depozice tenkých vrstev magnetických materiálů na standardní AFM sondy.

Připravte vzorky magnetických nanostruktur, proveďte měření MFM a naměřená data interpretujte s pomocí mikromagnetických simulací.

Seznam odborné literatury:

HOPSTER, H a H OEPEN. Magnetic microscopy of nanostructures. 1st ed. New York: Springer, 2004, xvi, 313 p. ISBN 35-404-0186-5.

Vedoucí diplomové práce: Ing. Michal Urbánek, Ph.D.

Termín odevzdání diplomové práce je stanoven časovým plánem akademického roku 2013/2014.

V Brně, dne 22.11.2013

<div align="center">L.S.</div>

_____   _____
prof. RNDr. Tomáš Šikola, CSc.   prof. RNDr. Miroslav Doupovec, CSc., dr. h. c.
        Ředitel ústavu   Děkan fakulty

ABSTRACT

The thesis deals with magnetic force microscopy of soft magnetic nanostructures, mainly NiFe nanowires and thin-film elements such as discs. The thesis covers almost all aspects related to this technique - i.e. from preparation of magnetic probes and magnetic nanowires, through the measurement itself to micromagnetic simulations of the investigated samples. We observed the cores of magnetic vortices, tiny objects, both with commercial and our home-coated probes. Even domain walls in nanowires 50 nm in diameter were captured with this technique. We prepared functional probes with various magnetic coatings: hard magnetic Co, CoCr and soft NiFe. Hard probes give better signal, whereas the soft ones are more suitable for the measurement of soft magnetic structures as they do not influence significantly the imaged sample. Our probes are at least comparable with the standard commercial probes. The simulations are in most cases in a good agreement with the measurement and the theory. Further, we present our preliminary results of the probe-sample interaction modelling, which can be exploited for the simulation of magnetic force microscopy image even in the case of probe induced perturbations of the sample.

KEYWORDS

Magnetic force microcopy, probe, soft magnetic nanostructure, magnetic vortex, nanowire, micromagnetic simulation.

ABSTRAKT

Práce pojednává o mikroskopii magnetických sil magneticky měkkých nanostruktur, zejména NiFe nanodrátů a různě tvarovaných tenkých vrstev - například disků. Práce se zaměřuje na téměř vše, co s touto mikroskopickou technikou souvisí: přípravu měřicích sond a vzorků, samotná pozorování a mikromagnetické simulace magnetického stavu vzorků. Byla pozorována jádra magnetických vírů, jak s komerčními, tak s námi připravenými sondami. Podařilo se zobrazit i magnetické doménové stěny v nanodrátech o průměru pouhých 50 nm. Připravili jsme fungující sondy s různými magnetickými vrstvami: magneticky tvrdého kobaltu, slitiny CoCr a magneticky měkké slitiny NiFe. Magneticky tvrdé sondy poskytovaly lepší signál, zatímco magneticky měkké byly vhodnější pro pozorování magneticky měkkých vzorků, protože je příliš neovlivňují. Námi připravené sondy jsou přinejmenším srovnatelné se standardními komerčními sondami. Simulace se ve většině případů shodují jak s měřením, tak teorií. Dále představujeme také naše prvotní výsledky modelování interakce vzorku s magnetickou sondou, které mohou složit k simulaci měření pomocí mikroskopie magnetických sil, a to i v případě, kdy sonda ovlivňuje magnetický stav vzorku.

KLÍČOVÁ SLOVA

Mikroskopie magnetických sil, sonda, magneticky měkká nanostruktura, magnetický vír, nanodrát, mikromagnetická simulace.

DECLARATION

I declare that I have written my master's thesis on the theme of "Characterization of magnetic nanostructures by magnetic force microscopy" independently, under the guidance of the master's thesis supervisor and using the technical literature and other sources of information which are all quoted in the thesis and detailed in the list of literature at the end of the thesis.

As the author of the master's thesis I furthermore declare that, as regards the creation of this master's thesis, I have not infringed any copyright. In particular, I have not unlawfully encroached on anyone's personal and/or ownership rights and I am fully aware of the consequences in the case of breaking Regulation §11 and the following of the Copyright Act No 121/2000 Sb., and of the rights related to intellectual property right and changes in some Acts (Intellectual Property Act) and formulated in later regulations, inclusive of the possible consequences resulting from the provisions of Criminal Act No 40/2009 Sb., Section 2, Head VI, Part 4.

Brno   . . . .
                                                      (author's signature)

ACKNOWLEDGEMENT

CONTENTS

LIST OF FIGURES

LIST OF TABLES

1 INTRODUCTION

Magnetic nanostructures have great applications in the field of magnetic recording, e.g. a Hard Disc Drive (HDD). Other promising spintronic (spin-electronic) devices have been proposed such as magnetic non-volatile memories (MRAMs) and other based on magnetic nanowires or discs hosting magnetic vortices. Even some commercially available MRAMs exist [1]. The miniaturization impetus, demand for smaller bits and higher data density, requires techniques that are suitable for magnetic imaging at nanoscale. One of the proven techniques is Magnetic Force Microcopy (MFM) [2], which is based on Atomic Force Microscopy (AFM) [3] with a magnetic probe. Even though it is quite slow and not so easy to interpret in some cases, it provides very good resolution, down to 10-15 nm [4], and versatility for a reasonable price.

Magnetic vortices, mostly in soft magnetic permalloy discs, have been intensively studied at our Institute of Physical Engineering (IPE). The ultimate goal is the efficient switching between four possible states of the vortex at (sub) nanosecond-time-scale. The main experiments are carried out at synchrotrons, large facilities providing high-intensity and if required highly monochromatic radiation, mainly X-rays for probing the magnetic state of the sample and its switching. The beam-time at such a facility is limited and not so easily obtained.

It is possible to test various switching techniques *offline* by measurement of the state before and after the switching event without informations about the dynamics. If the switching process yields the desired states, in the other words the method is reliable, one can request the beam-time and use it more effectively - focusing on the dynamics. Magnetic force microscopy enables such offline observations.

There have been some attempts at the institute to image magnetic vortices and especially their cores, tiny objects, by MFM, but until now they have failed. In this work we present the MFM observations of the cores of the magnetic vortices both with commercial and our home-coated probes. Other interesting and even more challenging samples - magnetic nanowires - are covered as well.

The following text focusses on almost all aspects related to MFM: from preparation of magnetic probes and magnetic nanowires, through the measurement itself to micromagnetic simulations of the measured samples. The structure of the work is as follows:

We will start with introduction to the magnetism in low dimensions in chapter 2, which involves mainly micromagnetism (nanomagnetism) used for the description of the nanostructures and their modelling. We will briefly discuss possible magnetic states in samples of interest in this work - nanowires, magnetic vortices in discs and soft magnetic (rectangular) thin-film elements in general.

Chapter 3 involves the description of magnetic force microscopy itself, both theory and examples of measurement performed on soft magnetic nanostructures. As the magnetic probes are key elements for the imaging, the whole chapter 4 is devoted to the probe preparation and their parameters important for the imaging. Chapter 5 focusses on methods used in experiments: electrodeposition of magnetic nanowires, Ion Beam Sputter deposition (IBS), inspection of the probes and the samples by Scanning Electron Microscopy (SEM) and Energy-Dispersive X-ray spectroscopy (EDX). Few notes on instrumentation are given as well. The chapter ends with information on micromagnetic simulations with Object Oriented MicroMagnetic Framework (OOMMF) solver. Finally, results of fabrication, measurements and corresponding simulations are presented in chapter 6.

The work on nanowires, except the simulations, was done during author's Erasmus research internship at Institut Néel of CNRS in Grenoble (France), where the author improved and acquired many of his skills, MFM imaging in particular.

2   MAGNETISM IN LOW DIMENSIONS

Magnetism is of a pure quantum-mechanical origin and should be rigorously treated in this regard. On the other hand, real systems are too large for exact treatment of the many body problem, i.e. solving the many-body Schrödinger equation, due to limited computational resources. Therefore approximative approaches such as the Hartree–Fock method, wave function–based approximation, and the Density-Functional Theory are employed. In some cases, statistical theories and even classical electrodynamics can be used as well. [5, p. 1]

In this chapter, after recalling some basics of magnetism, we will restrict ourselves to micromagnetism. This continuous theory is especially suitable for a description of nanostructures which form usually too large systems to be addressed by (relativistic) quantum mechanics, however, still too small to be described by the phenomenological Maxwell's theory of electromagnetic fields. Micromagnetism bridges the gap between these two approaches - assuming continuum while taking results derived from quantum mechanics. Rest of the chapter is devoted to magnetism and magnetization in low dimensional structures, patterned thin films and one-dimensional structures in particular, being suitable for the characterization via magnetic force microscopy.

2.1   Magnetism - basics

Magnetism originates mostly in spin polarized currents, e.g. unpaired electrons in Fe, Ni and Co atoms. Unlike in electrostatics, the basic element of magnetism is still a current loop - magnetic dipole - characterised by magnetic moment $\vec{\mu}$. However, the concept of magnetic monopoles - magnetic charges - is used in theory, description of various phenomena as well as in magnetic force microscopy. It turns out that the concepts of magnetic dipoles, current loops and magnetic charges give the same results but in a particular case one of them might be more viable, for example from the computational point of view. We will cover only some aspects of magnetism, which are related to the following sections. Basics of magnetism can be found in many physics textbooks such as [6, 7].

Volume density of magnetic dipoles is called magnetization $\vec{M}$. In analogy with electrostatics, $\vec{J} \equiv \mu_0 \vec{M}$ is polarization with μ_0 being vacuum permeability. Magnetic dipole in vacuum creates a magnetic field $\vec{H}$, in a material magnetic induction defined by the material relation:

$$\vec{B} = \mu_0 \vec{H} + \mu_0 \vec{M}. \tag{2.1}$$

To shine some light on these magnetic vectors [1] and the material relation (2.1) let us assume simple case of a homogeneously magnetized body, e.g. a magnetic [2] disc with an out-of-plane magnetization (see Figure 2.1). $\vec{H}$-field in the material opposes magnetization, that is why it is called the demagnetizing field $\vec{H}_\mathrm{d}$. $\vec{H}$-field outside the body, referred to as the stray field $\vec{H}_\mathrm{s}$, forms closed loops in the same way as $\vec{B}$-field does. This is not a surprise when taking into account that in the free space $\vec{B} = \mu_0 \vec{H}_\mathrm{s}$ and both fields are divergenceless. Maxwell equation $\vec{\nabla} \cdot \vec{B} = 0$ is fulfilled, i.e. there are no sources of the $\vec{B}$-field. On the other hand, there is no reason why $\vec{H}$ or $\vec{M}$ should not have their sources. This idea leads to the concept of magnetic charges. In analogy with electrostatics [3], volume (ρ_m) and surface (σ_m) density of magnetic charges (shortly just charges) are defined as:

$$\rho_\mathrm{m} = -\mu_0 \vec{\nabla} \cdot \vec{M} = \mu_0 \vec{\nabla} \cdot \vec{H}, \qquad (2.2)$$

$$\sigma_\mathrm{m} = \mu_0 \vec{n} \cdot \vec{M}. \qquad (2.3)$$

Second part of (2.2) originates in inserting [4] material relation (2.1) into Maxwell equation $\vec{\nabla} \cdot \vec{B} = 0$. Vector $\vec{n}$ in (2.3) denotes outward-directed surface normal. Note that very often the volume magnetic charges are defined simply as $\rho_\mathrm{m} = \vec{\nabla} \cdot \vec{M}$ (and this definition will be used as well). Here, more rigorous definition from [9] was given. The difference is just in multiplication by a constant, magnetic charges are related to divergence of magnetization in both cases.

Typical way how to characterise a magnetic material is to observe its behaviour in an external magnetic field - i.e. to measure its hysteresis loop - as the one in Figure 2.2. Magnetic moments in the sample, grouped in so called domains (see section 2.2.3), points in random directions so almost no net magnetization exists. Upon increase of the external field, magnetic moments are being aligned with the external field until the saturation value is reached. Decreasing the field and applying the field in opposite direction results in hysteresis behaviour - dependence on previous states. Even though the moments are again being aligned with the field, the material exhibits remanent magnetization (remanence) M_r in zero applied field. A non-zero field of the opposite direction, so called coercive field or coercivity H_c, is necessary to reach zero net magnetization. Here, well-behaved bulk material was treated for the sake of simplicity. More complex curves can be obtained for real materials, samples composed of different magnetic bodies, multilayers, array of

---

[1] Axial vectors to be precise, there is a sign change with respect to time reversal, so their symmetry differ from their electric counterparts [8].

[2] When referring to magnetic we will mean ferromagnetic materials. Diamagnetic, paramagnetic, anti-ferromagnetic materials, helical magnets etc. are not of an interest in this work.

[3] $\vec{\nabla} \cdot \vec{E} = \frac{\rho_\mathrm{e}}{\epsilon_0}$ and therefore $\vec{\nabla} \cdot \vec{H} = \frac{\rho_\mathrm{m}}{\mu_0}$.

[4] $\left(\vec{\nabla} \cdot \vec{B} = 0 \right) \wedge \left(\vec{B} = \mu_0 \vec{H} + \mu_0 \vec{M} \right) \Rightarrow -\mu_0 \vec{\nabla} \cdot \vec{M} = \mu_0 \vec{\nabla} \cdot \vec{H} = \rho_\mathrm{m}$.
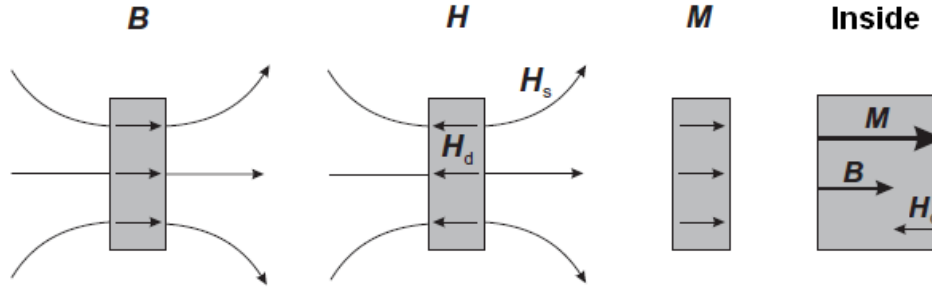
Fig. 2.1: Magnetic axial vectors characterizing an uniformly magnetized ferromagnetic disc with an out-of-plane magnetization - from the left: $\vec{B}$, $\vec{H}$, $\vec{M}$ and overall picture inside the material. $\vec{H}$-field inside the disc acts against the magnetization, hence called demagnetizing field $\vec{H}_\mathrm{d}$. $\vec{H}$-field emanating from the body, stray field $\vec{H}_\mathrm{s}$, closes in loops as $\vec{B}$-field does. Taken from [8], note that vectors are denoted in bold.

micro/nano structures. Note that only projection of magnetization into the direction of the external field is measured.

Remanent magnetization gives an information on *how much* magnetization is retained after removal of the external field. Coercivity shows how difficult it is to reverse or switch the magnetization. Both of these characteristics are important for magnetic probes for magnetic force microscopy. An area enclosed by the hysteresis loop is related to the energy losses during the magnetization process in the external field. Two types of magnetic materials are distinguished:

hard - high remanence and coercivity, e.g. permanent magnet producing strong magnetic field and not so easily influenced by external fields,

soft - low remanence and coercivity, e.g. core of a transformer requiring very low losses during the operation.

Both hard and soft magnetic materials are used for MFM probes as we will see later.

Magnetic recording media, one of the most important applications of magnetism, lies somewhere in between - a reasonable remanent magnetization is required for a good signal when reading the data from the medium. Coercivity should be high enough so that the medium keeps the stored information, but too high coercivity means that high fields have to be applied for writing, which leads to undesired higher power consumption.

2.2 Micromagnetism

Micromagnetism, sometimes merged with nanomagnetism, is suitable for description of magnetism at mesoscopic scale - i.e. micro and nanostructures. It forms basics of
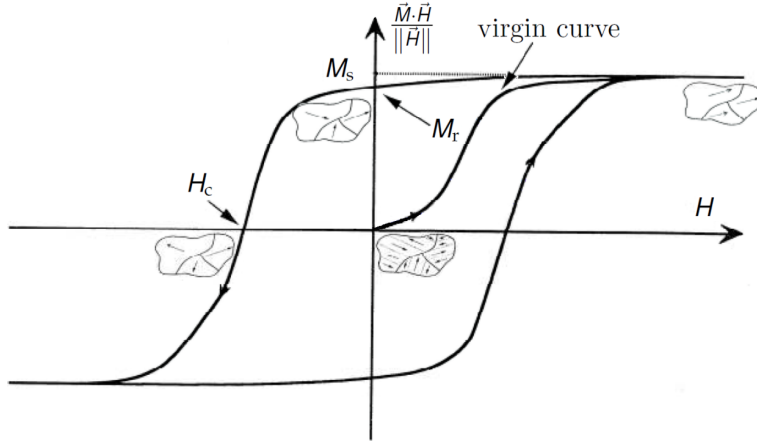
Fig. 2.2: Hysteresis curve of a ferromagnet - dependence of the magnetization M (projection into the direction of the external field) on the applied magnetic field with magnitude H. Virgin magnet not spoiled by the external magnetic field exhibits no net magnetization. Application of the increasing field gradually turns magnetic moments of the sample into the field's direction - magnetization rises, following so called first magnetization (virgin) curve. After reaching the saturation value of magnetization M_s, higher field doesn't lead to any significant increase. After removing the field, the sample keeps the so called remanent magnetization M_r. In order to reduce the net magnetization to zero, an external field of opposite direction, referred to as a coercive field, has to be applied.

micromagnetic simulations of nanostructures which will be used in this work. It is a continuum theory of magnetism, where magnetization is supposed to be a continuous function of a position in space. In addition, it is assumed that the magnetization vector has a constant norm for homogeneous materials, thus only the direction of magnetization is allowed to change:

$$\vec{M}_\mathrm{s} = \vec{M}_\mathrm{s}(\vec{r}), \left\|\vec{M}_\mathrm{s}\right\| = \mathrm{const.} \tag{2.4}$$

The topic will be covered only briefly without derivations and provision of deeper insight. Interested reader is encouraged to consult an excellent book *Magnetic Domains* [9] and other helpful resources [10, 11].

2.2.1 Magnetization dynamics

Magnetization dynamics, i.e. the evolution of magnetization, is described by the Landau-Lifschitz-Gilbert (LLG) equation:

$$\frac{\partial \vec{M}}{\partial t} = \gamma_\mathrm{G} \vec{M} \times \vec{H}_\mathrm{eff} + \frac{\alpha_\mathrm{G}}{M_\mathrm{s}} \vec{M} \times \frac{\partial \vec{M}}{\partial t}. \tag{2.5}$$

The first term stands for Larmor precession of the magnetization around an effective magnetic field $\vec{H}_{\text{eff}}$. $\gamma_{\text{G}} = -\mu_0 g \frac{e}{2m_e}$ is Gilbert gyromagnetic ratio, with e being elementary charge and m_e mass of the electron. The Landé g factor has value close to two for many ferromagnets [9]. Gyromagnetic ratio links magnetic moment $\vec{\mu}$ with angular momentum $\vec{L}$: $\vec{\mu} = \gamma \vec{L}$. As we know from mechanics, $\frac{d\vec{L}}{dt} = \vec{T}$, where $\vec{T}$ stands for torque. Thus all the terms on the right-hand-side of (2.5) can viewed as *torques* [5] multiplied by a constant.

Because real magnetic systems possess losses, the precessional motion is being damped and finally magnetization is oriented (anti)parallel with respect to $\vec{H}_{\text{eff}}$, as expected [6]. This is described by the second term in (2.5) with α_{G} being dimensionless empirical (phenomenological) Gilbert damping parameter with typical values for real material $10^{-3} - 10^{-1}$. It describes further unspecified dissipative phenomena such as magnon scattering on lattice defects. Vectors and terms acting in the LLG equation are depicted in Figure 2.3.
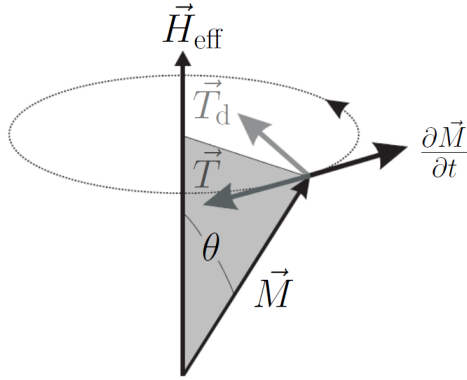
Fig. 2.3: Schematic picture of the dynamics of a magnetization vector (or magnetic moment) - graphical representation of the LLG equation. Torque $\vec{T} = \vec{M} \times \vec{H}_{\text{eff}}$ acts on the magnetization $\vec{M}$ in an effective field $\vec{H}_{\text{eff}}$. This leads to a precession of the magnetization around $\vec{H}_{\text{eff}}$ in a direction opposing $\vec{T}$, because γ_{G} is negative. In case of non-zero damping α, a damping torque $\vec{T}_{\text{d}}$ emerges. It is related to the second term in the LLG equation. For common case of positive α it aligns the magnetization with the effective field. Therefore the end point of $\vec{M}$ goes in a spiral before it reaches final state (angle $\theta = 0$). Typical time-scale for this process is in the order of nanoseconds. Adapted from [8].

---

[5]Recall that eg. torque acting on a magnetic dipole in external magnetic field is given by $\vec{T}_e = \vec{\mu} \times \mu_0 \vec{H}$.

[6]Magnetization precessional dynamics can be viewed as analogue with gyroscope in mechanics. Even though antiparallel alignment of $\vec{M}$ with respect to $\vec{H}_{\text{eff}}$ in case of negative α_{G} might be a surprise, it has its mechanical analogy as well: special spinning tops having a low lying centre of gravity - *tippe tops*. Some reader may recall the photo in which even Wolfgang Pauli and Niels Bohr were fascinated by upside-down flip of the *tippe top* [8, Fig. 3.18].

It follows from thermodynamics that the effective magnetic field is given by:

$$\vec{H}_{\text{eff}} = -\frac{1}{\mu_0}\frac{\partial E}{\partial \vec{M}}, \tag{2.6}$$

where E is the total energy of the system under consideration. Particular energy contributions will be described in the next section.

New phenomena in magnetization dynamics such as *spin transfer torques* [12] or *Dzyaloshinskii–Moriya interaction* [13] can be incorporated into the LLG equation (2.5) as additional *torques* or included in effective magnetic field $\vec{H}_{\text{eff}}$ as new energy contributions.

2.2.2   Energies at play

There are various contributions to the total energy of a (micro)magnetic system, among them the most important are: exchange, Zeeman, magnetostatic and magnetocrystalline anisotropy energy.

Exchange energy

This contribution results from purely quantum mechanical interaction between spins. In case of direct Heisenberg exchange, exchange energy of two spins $\vec{S}_1$, $\vec{S}_2$ reads [7]:

$$E_{\text{ex,spin}} = -J_{1,2}\vec{S}_1 \cdot \vec{S}_2. \tag{2.7}$$

Here, constant J represents the value of exchange integral and in the case of a ferromagnet $J > 0$. Thus alignment of neighbouring spins in the same direction is preferred. In micromagnetism we work with continuous magnetization rather than with spins. Very often magnetization is supposed to be constant in a very small volume. Then we can speak of a *macrospin.* If the magnetization in a ferromagnet deviates from uniform one, an energy penalty in the form of an isotropic volume [7] exchange stiffness energy appears:

$$E_{\text{ex}} = A \iiint_{\text{ferromagnet}} \left(\vec{\nabla}\cdot\frac{\vec{M}}{M_{\text{s}}}\right)^2 \mathrm{d}V, \tag{2.8}$$

where A is exchange stiffness with dimension J/m. At zero temperature, still used in many simulations, its value is related to the critical Curie temperature T_{c}: $A(T = 0\,\text{K}) \approx k_{\text{B}}T_{\text{c}}/a_{\text{L}}$, with k_{B} being Boltzmann's constant and a_{L} lattice parameter of the ferromagnetic crystal [9]. Typical value is of the order of $10\,\text{pJ/m}$: $31\,\text{pJ/m}$ for cobalt and $10\,\text{pJ/m}$ for permalloy ($Ni_{80}Fe_{20}$) [14].

---

[7]There exist also interface exchange coupling, when two different ferromagnets are in contact. This case is far beyond the scope of this work.

As $\vec{\nabla} \cdot \vec{M}$ is related to volume magnetic charges, we can see the tendency for their minimization. On the other hand surface charges are present at the ends of an uniformly magnetized region.

Generalized expression states:

$$E_{\text{ex}} = \iiint\limits_{\text{ferromagnet}} \sum_{i,k,l} A_{kl} \frac{\partial}{\partial x_k} \left(\frac{M_i}{M_{\text{s}}} \right) \frac{\partial}{\partial x_i} \left(\frac{M_i}{M_{\text{s}}} \right) \mathrm{d}V. \qquad (2.9)$$

Fortunately, symmetric tensor A_{kl} reduces to a simple scalar for cubic or isotropic materials, thus isotropic stiffness expression (2.8) can be used [9].

Zeeman energy

Zeeman energy stands for an external field energy, This contribution gives an energy penalty if the magnetization does not lie in the direction of an external applied field:

$$E_{\text{Z}} = -\mu_0 \iiint\limits_{\text{ferromagnet}} \vec{M} \cdot \vec{H}_{\text{ext}} \mathrm{d}V. \qquad (2.10)$$

Magnetostatic energy

Magnetostatic (dipolar) energy describes Zeeman-like mutual interactions of magnetic moments in a ferromagnet and reads:

$$E_{\text{d}} = -\frac{1}{2}\mu_0 \iiint\limits_{\text{ferromagnet}} \vec{M} \cdot \vec{H}_{\text{d}} \mathrm{d}V. \qquad (2.11)$$

Sometimes energy density called dipolar constant $K_{\text{d}} = \frac{1}{2}\mu_0 M_{\text{s}}^2$ is used. While demagnetizing field $\vec{H}_{\text{d}}$ has zero curl, it results from a potential: $\vec{H}_{\text{d}} = -\vec{\nabla}\phi_{\text{d}}$. Using this notation and the concept of magnetic charges, magnetostatic energy can be expressed in a slightly different form [9]:

$$E_{\text{d}} = \mu_0 M_{\text{s}} \left(\iiint\limits_V \rho_{\text{m}}\phi_{\text{d}}\mathrm{d}V + \oiint\limits_{\partial V} \sigma_{\text{m}}\phi_{\text{d}}\mathrm{d}S \right). \qquad (2.12)$$

To minimize E_{d}, we need to reduce both volume and surface charges, which leads to a so called charge avoidance principle. Surface charges can be avoided when the magnetization lies parallel to the sample edges, which can lead to a so called flux closure as will be shown later. Shape of the sample - integration region - has also significant influence on the magnetization configuration. Sometimes we speak about shape anisotropy in this case. However, the shape anisotropy is not related to other anisotropies like the magnetocrystalline one, which will be cover in the next section.

Magnetocrystalline anisotropy

In a crystal not all directions of the magnetization have the same energy. Due to crystal-field effects, coupling electron orbitals with the lattice, and coupling of electron orbitals with spins, some directions (planes) with respect to the crystal axes are preferred. These are so called easy axes [8]. On the other hand less favoured hard axes exist [11]. Rigorous treatment of magnetocrystalline anisotropy is quite complex as well as formulas used for its description, interested reader may consult references [5, 9, 14]. Very often volume density of magnetic anisotropy energy is given in terms of set of angular functions. Here we will restrict ourselves to simple example of uniaxial anisotropy found in hexagonal and orthorhombic crystals:

$$\epsilon_{\mathrm{mc,u}} = K_1 \sin^2 \theta + K_2 \sin^4 \theta + \cdots, \qquad (2.13)$$

where K_i are anisotropy constants with dimension $\mathrm{J/m^3}$ and θ is angle between magnetization and the anisotropy axis. Anisotropy constants for higher power terms are usually negligible and sometimes only the first term is taken into account. Cobalt is a typical represent with $K_1 = 520 \, \mathrm{kJ/m^3}$ and the c axis of the hexagonal crystal being the only easy axis [11].

Mercifully, we will be mostly concerned with soft magnetic samples made of permalloy which exhibits very low magnetocrystalline anisotropy. Therefore we will neglect this term in most of our computations. This brings us back to the distinction between soft and hard magnetic materials. As coercivity is related to the magnetocrystalline anisotropy, soft (hard) magnets posses low (high) anisotropy.

So far we have spoken of undeformed lattice. External stress results in magnetoelastic contribution which is sometimes taken as a part of magnetocrystalline anisotropy. Local deformation may result from stress generated by the ferromagnetic material itself - magnetostriction [14]. These contributions are very often negligible.

2.2.3 Magnetic domains and domain walls

Magnetic domains are regions with (almost) uniform magnetization within a magnetic body. Their creation results from competition of particular energy contributions, mainly exchange, magnetostatic and anisotropy energy. How this *combat* influences magnetization in a spheroidal particle is illustrated in Figure 2.4. Exchange energy favours uniform magnetization, thus only one domain is present - we speak of a single domain-state. If we add magnetostatic interaction, flux-closure pattern appears as a tendency to minimize surface charges by keeping magnetization parallel to the particle edges. Anisotropy favours only some directions of the magnetization, thus domains separated by boundary, domain wall (DW), emerge. Domain

---

[8]More generally not only easy axes, but easy planes and surfaces exist.

theory is very complex and there is no single and simple origin of domain creation for all materials. It rather differs from case to case, depending on anisotropies, shape and size of the sample. For sure, magnetostatic energy plays an important role in this case [9]. For rigorous treatment and nice pictures of various domains (bamboo, bubble, spike, labyrith, saw-tooth, . . .) consult the excellent book - *Magnetic domains* [9].
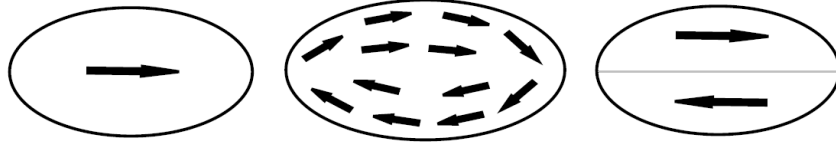
Fig. 2.4: Influence of energy contributions on a spheroidal particle. In first particle (from the left), only exchange is taken into account, thus uniform magnetization is present. In the middle flux-closure pattern results from competition of exchange and magnetostatic energy. On the right, particle with a considerable uniaxial anisotropy is split into two domains as intermediate directions of the magnetization are unfavourable. Gray line represents the the domain boundary - domain wall. Adapted from [14].

2.2.4   Characteristic lengths in (micro)magnetism

As a consequence of competition of different interaction, characteristic quantities such as lengths arise. We will mention here only two of them [11]:

- anisotropy exchange length (Bloch parameter): $\Delta_a = \sqrt{\frac{A}{K_a}}$,
- dipolar exchange length (exchange length): $\Delta_d = \sqrt{\frac{A}{K_d}}$.

Δ_a is more relevant for hard magnetic materials, where exchange and anisotropy (with anisotropy constant K_a) compete. This length corresponds to the width of a domain wall separating two domains. For soft magnets, it is Δ_d with exchange and dipolar energy in arena. Their main importance for us will be elucidated in the next section, briefly dealing with micromagnetic simulations. Δ_a is roughly $1\,\mathrm{nm}$ for hard magnets and up to several hundreds nanometers for soft magnets. Δ_d lies near $10\,\mathrm{nm}$ for both types [11]. Therefore we see, that nanoscale is really important in magnetism.

2.2.5   Micromagnetic simulations

Analytical solutions are available only to limited amount of rather simple micromagnetic problems. Thus, numerical simulations have to be employed for real three-dimensional problems, where equilibrium magnetic configuration of a magnetic body is sought or its dynamics under external field tracked.

Like in every numerical computation, discretization of part of the space with our magnetic body into small cells plays a key role. There are two main approaches:

- body composed of cubes (rectangular parallelepipeds) - finite difference (FD) method,
- body composed of tetrahedra - finite element (FE) method.

In both cases, magnetization in the cell is supposed to be constant. Therefore we can say that the cell possesses macrospin. The solution to our problem is obtained either by numerical integration of the LLG equation (2.5) or by seeking the minimum of the corresponding energy functional (sum of al energy contributions). The former can track the magnetization dynamics, the later provides ground state of the sample under the investigation. Both FD and FE have their virtues and drawbacks.

Finite difference usually consumes less computer memory, are suitable for rectangular shapes and an excellent choice for thin films with large surface, where FD override FE. Use of identical cubic cells enables faster computation of magnetostatic interactions which is commonly the slowest part of the simulation. As derivations are substituted by differences, new terms in the LLG equation are more easily incorporated into the FD than into FE. Typical example of FD solver is OOMMF [15], which is used in this work and is further described in section 5.3.

Finite elements are best for geometries with some curvature, angles different from $90°$. In these cases very often larger cell might be used compared to FD with almost no loss in precision. FE is also based on a more rigorous background. However, creation of the mesh requires some time. FE is represented for example by NMAG or Magpar [16]. We have mentioned above only freely available solvers, commercial and home-made codes exist as well.

Once we have chosen the method, the most important question is a size of the cell. The smaller, the more accurate results. On the other hand: the smaller, the more cells and thus computational time and resources are required. In derivation of micromagnetism, it is assumed that the magnetization varies only a little (only few first terms in Taylor expansion of exchange interaction are taken into account). To ensure this, cell size should be smaller than exchange length. In previous section we have mention two *exchange lengths*. As already mentioned Δ_a should be taken for hard and Δ_d for soft magnets. When in doubt, just choose the smallest of these two quantities [16].

To characterise variation of the magnetization in neighbouring cells, the quantity called *spin-angle* is used. Here $0°$ spin-angle means parallel magnetization in neighbouring cells. How big maximum value of spin-angle is still acceptable? M. J. Donahue, person behind OOMMF solver and other projects, says in email to H. Fangohr on 26 March 2002 referring to OOMMF:

- *If the spin angle is approaching 180 degrees, then the results are completely*

bogus.

- *Over 90 degrees the results are highly questionable.*
- *Under 30 degrees the results are <u>probably</u> reliable.*

To conclude, the right cell size is the one with low maximum spin-angle, especially for simulation of large objects. More information can be found for example in manuals of above mentioned solvers [15, 16], which were the main sources of information in this section.

It is necessary to note that atomistic treatment of nanomagnetism, usually based on multiscale models, exists as well. Open-source software for atomistic simulations taking some aspects from micromagnetism, VAMPIRE, is being developed. It enables atomistic treatment of magnetic nanostructures in a reasonable time [17].

2.3   Magnetization patterns in low dimensions

Bulk material comprises a high number of complex domains, whereas very small nanoparticles are in a single domain state. Between these two extrema, mesoscopic scale provides small number of simple domains, which are good objects for studies. Examples of the magnetic configuration at different scales are depicted in Figure 2.5.

In this section we will give some information on magnetic configurations that might be found (not only) at nanoscale. Some of these - vortices, domain walls in nanowires and various magnetization patterns in soft magnetic thin-film elements will be subject to MFM measurement and simulations as we will see in the following chapters. Other interesting structures exist - artificial spin-ices [18] and magnetic skyrmions [19].

2.3.1   Magnetic vortices

Magnetic vortices can be found in thin discs, prisms and even less regular shapes, depending on the geometry and the material. Smaller objects tend to be in single domain state and larger ones approach multi-domain state. In prisms, e.g. diesquares, 90° domain walls appear and so called Landau pattern is formed as shown in Figure 2.7.

Closed magnetic flux of the vortex minimizes the demagnetization energy. On the other hand, there is a penalty in higher exchange energy which causes the magnetization to point out-of-plane in the centre. Aside from flux closure, described by circulation (clockwise, anti-clockwise), vortex possesses a core with out-of-plane magnetization, denoted by polarity (up, down). These two degrees of freedom - circulation and polarity - are independent. As a consequence, four states with the same energy exist as illustrated in Figure 2.6. Nowadays, data are encoded in binary
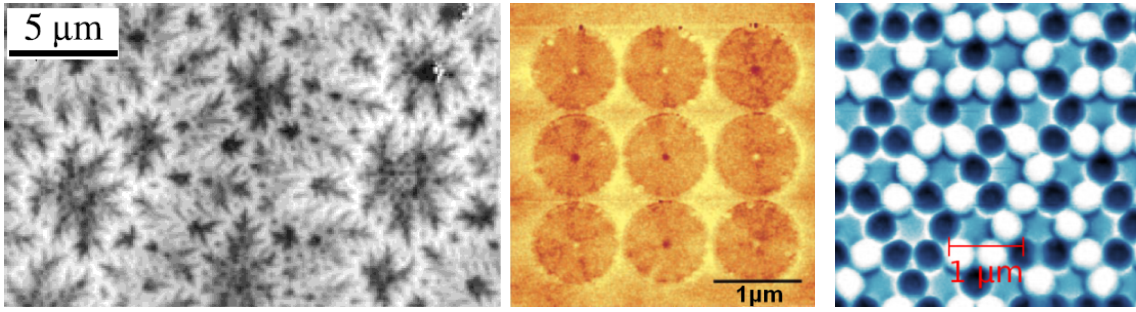
Fig. 2.5: Magnetic force microscopy images of magnetic structures at different length-scales. On the left: rather complex domain structure in a (1000) surface of a bulk cobalt sample [9]. In the middle: magnetic vortices in permalloy discs [20]. Finally on the right: array of uniformly magnetized dots (up or down magnetization), imaged by N. Rougemaille and I. Chioar at Institut Néel. Dark and bright regions corresponds to areas with opposite magnetization. Note, that bright areas around discs in the middle picture come from image processing and that bright dots, not including the central ones, are impurities or topography defects as will be discussed later on.

system (0, 1), here four states might be exploited. Random number generator based on magnetic vortices is under consideration as well [21].
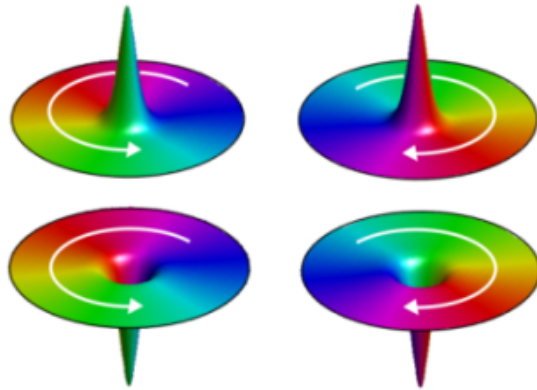
Fig. 2.6: Four remanent states of a magnetic vortex. The vortex is described by circulation, clock-wise or anticlockwise flux-closure of the magnetization, and up or down polarity of the core in the centre. Image courtesy of Michal Urbánek.

2.3.2 Domain walls in nanostrips

In nanostrips, usually prepared by lithography from thin films, magnetization tends to be in-plane. In this case two types of DWs can be observed - transverse and vortex. If high perpendicular magnetic anisotropy [22] is present, e.g. in very thin (multi)layers - less than few nanometers thick, out-of-plane magnetization can be
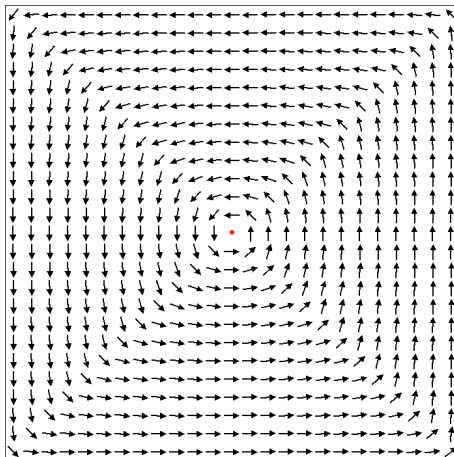
Fig. 2.7: Magnetic vortex in a diesquare with four domain walls (diagonals of the square). As in case of the disc, four states with different combination of circulation and polarity exist. Black arrows depict in-plane magnetization and red dot in the centre represents the core with out-of-plane magnetization. Edited simulation from micromagnetic solver OOMMF (will be described later in section 5.3).

present with Bloch and Néel walls. Domain walls in nanostrips are schematically shown in Figure 2.8.

2.3.3   Domain walls in nanowires

In nanowires (NWs) both with circular and square cross-section, magnetization tends to point out along nanowire axis, due to the shape anisotropy. Two types of domain walls have been predicted by simulations [24, 25] and recently identified by X-ray related techniques [23, 26] and by MFM at Institut Néel. Nanowires with diameters smaller than several dipolar exchange lengths contain transverse wall [TW, depicted in Figure 2.9(a)] similar to vortex and transverse walls in nanostrips [26], whereas large-diameter-nanowires bear so called Bloch point wall [BPW, demonstrated in the centre of Figure 2.9(b)] sometimes confusingly referred to as vortex wall - e.g. [27]. BPW name originates in Bloch point in its centre where magnetization vanishes. Although magnetization configuration of BPW may somewhat resemble vortices found in discs and diesquares, BPW possesses no core with out-of-plane magnetization, the magnetization vanishes in the centre instead. Both types of DW should have the same high DW propagation speed ($> 1\,\mathrm{km/s}$) under an external magnetic field necessary for spintronic devices like the race-track memory [28].

(a)   (b)

(c)   (d)
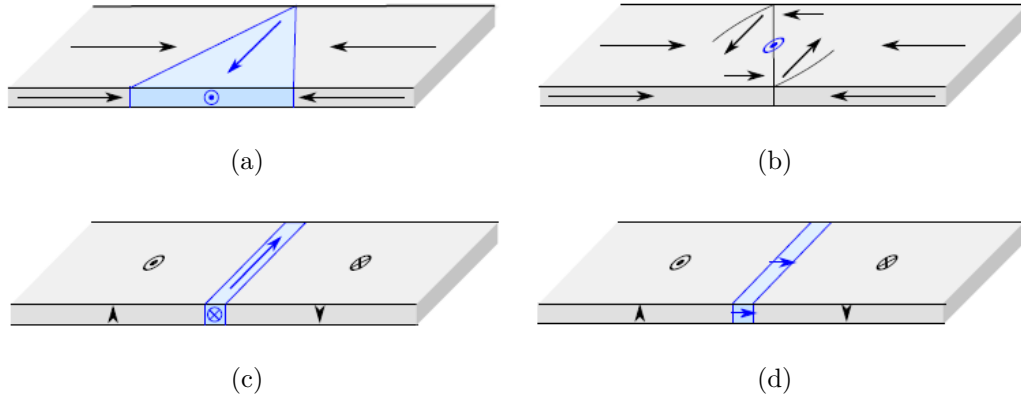
Fig. 2.8: Domain walls in nanostrips. (a)-(b) Strips with in-plane magnetization with domain walls of type (a) transverse and (b) vortex. (c)-(d) Strips with out-of-plane magnetization with DWs of type (c) Bloch and (d) Néel. Arrows depict local magnetization, domain wall region is highlighted with blue color. [23]

(a)   (b)
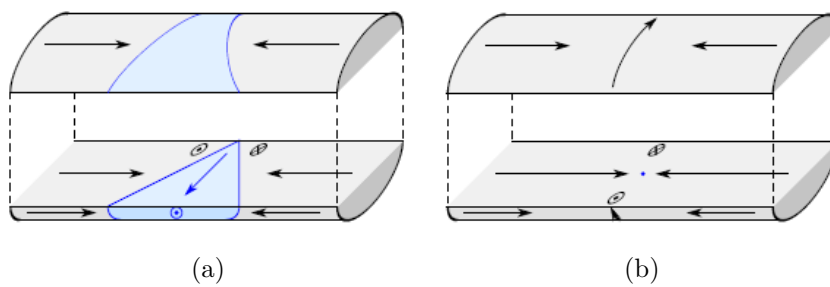
Fig. 2.9: Domain walls in nanowires: (a) transverse wall found in small-diameter nanowires and (b) Bloch point wall in thicker ones, sometimes called confusingly vortex wall. Magnetization vanishes in the centre of the BPW - here denoted with a small blue dot (the Bloch point is considered an 0D object). Taken from [26].

2.3.4 Domain walls in nanotubes

Similarly to nanowires the magnetization lies along the tube axis and two types of DWs have been predicted [29]: transverse and vortex wall (analogue of the BPW in nanowire, without the Bloch point due to the missing material in the centre). They have not been observed experimentally so far. Like in the nanowire case, DW in nanotubes should have high mobility, this implies potential use in spintronics.
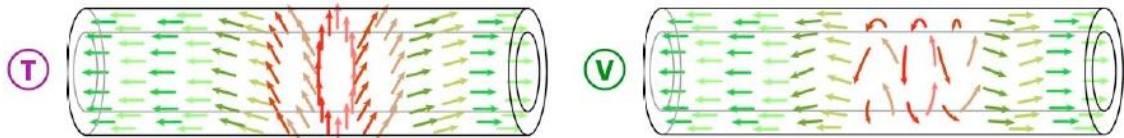
Fig. 2.10: Domain walls in ferromagnetic nanotubes: (T) transverse and (V) vortex wall, arrows depict the direction of magnetization [30].

2.3.5 Patterned permalloy thin films

Small dots and strips have already been covered above. Here we will focus on rectangular-shaped thin film elements, which are being prepared in most cases by Electron Beam Lithography (EBL) and thin film deposition. These structures were used for measurement in this work including test of prepared MFM probes.

Depending on the shape, size (thickness) and magnetic history of the sample, different magnetic configurations are favoured. Maps of magnetic charges for the common states are given in Figure 2.11, these images are close to the MFM measurement. Various states are demonstrated on an element with dimensions $2\,\mu m \times 1\,\mu m \times 20\,nm$. According to simulations by Rave and Hubert [31], the ground states is the diamond one. However energy of Landau pattern and single cross-tie is only a little bit higher than in case of the diamond. The situation might change for different dimensions. The diamond state and other ones resembling vortices are found usually in structures with a lower planar aspect ratio. On the other hand, C and S states seem to be preferred for elongated rectangles [32]. Note that previously applied external field may favour C and S states even for low aspect ratio structures.

For another images of thin-film elements see section 3.4.2 and Figure 3.9 in particular.
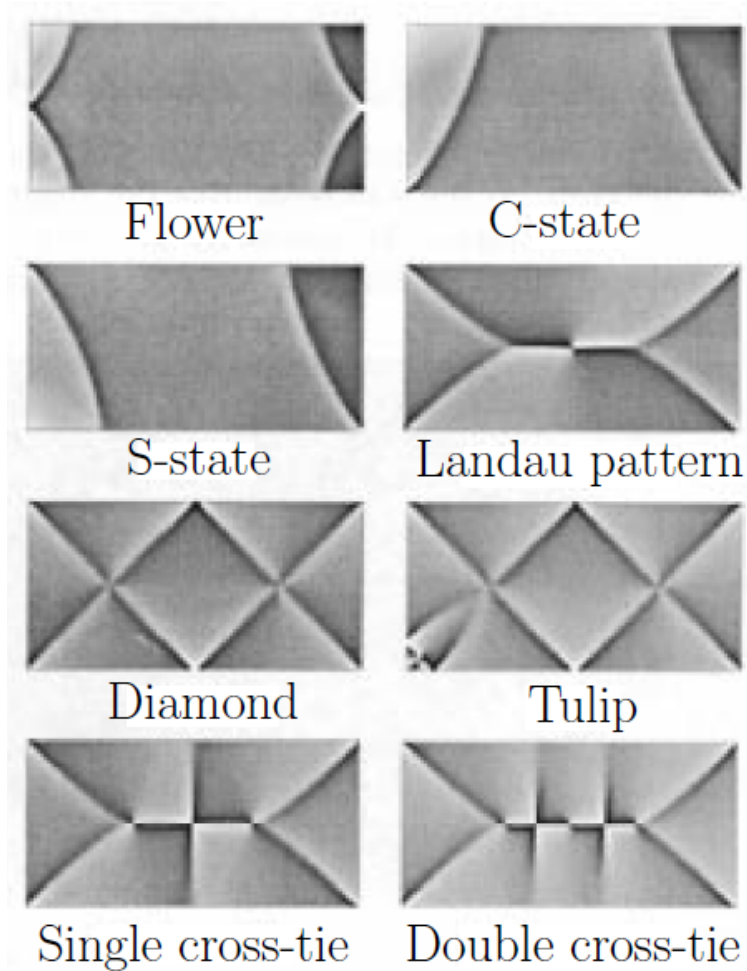
Fig. 2.11: Various magnetic configurations found in soft magnetic permalloy rectangles depicted as maps of magnetic charges, which resemble images acquired by MFM. Similar structures can be found for different aspect ratios. Here, element with dimensions 2 µm×1 µm×20 nm favours diamond state. But other states such as Landau pattern and cross-tie have only slightly higher energy. Taken from [31].

3 MAGNETIC FORCE MICROSCOPY

Soon after the invention of Atomic Force Microscope (AFM) [3], Martin and Wickramasinghe [2] introduced *magnetic imaging by 'force microscopy'*. Their invention was followed by further observation by Sáenz et al. [33]. Since these times, when etched ferromagnetic wires served as magnetic probes, the technique has evolved and nowadays it belongs to the standard imaging techniques of magnetic nanostructures. Two main milestones can be recognized: use of batch fabricated probes based on AFM cantilevers coated with thin magnetic film [34]; introduction of lift mode [35] for separation of topography and magnetic contributions. The lateral resolution has been improved from initial 100 nm to 10 nm [4] due to more sensitive detection and use of enhanced probes. Two main challenges remain: pushing the resolution below 10 nm and observation of soft magnets, which are very often influenced by the magnetic probe.

As MFM is based on AFM (in a simplified view: MFM=AFM+magnetic probe) we will start this chapter with a brief treatment of atomic force microscopy. We will follow with the theory of MFM imaging, where we will see that the interpretation of MFM images is not always straightforward and sometimes simulations are necessary to facilitate the analysis. Further, some examples of application of MFM to measurement of soft magnetic structures will be shown. Finally, main parameters influencing an MFM image will be covered. MFM probes will be discussed in the next chapter.

3.1 Atomic Force Microscopy

Atomic force microscopy relies on measurement of force acting between a sample and a very sharp tip - atomically sharp in ideal case. The tip is mounted on a mechanical lever built in a larger chip, thus referred to as a cantilever (illustrated in Figure 3.1; see also Figures 5.3 and 5.4). The radius of curvature of the tip apex (further on only tip radius) is usually below 10 nm. Both cantilever with the tip and the chip are very often from Si or Si_3N_4. For further applications, the tip may be coated with layers such as magnetic or conductive.

A simplified scheme of AFM is given in Figure 3.2. The sample is being scanned with the tip and the force is deduced from corresponding deflection of the cantilever. Very often a piezoelectric element, tube, is used for scanning, where voltage applied to the element leads to its deformation. If several electrode pairs are attached to the tube, setting appropriate voltages results in displacement of the element. For reliable operation of the AFM, calibrated scanner (non-linearity, hysteresis etc.) is required. Two designs exist - scanning by the sample or with the tip. The later one
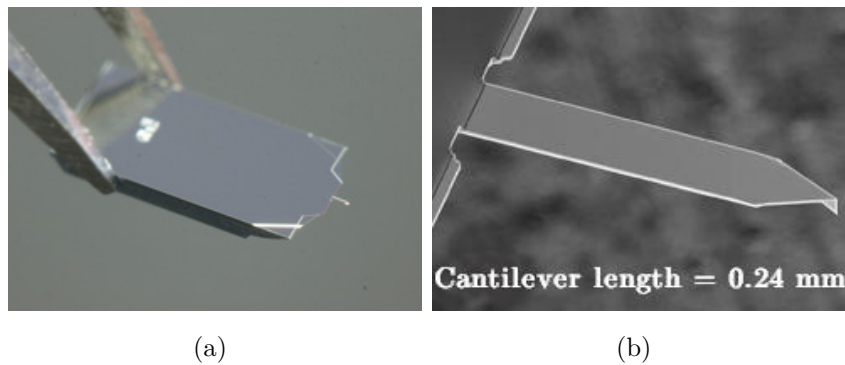
Fig. 3.1: AFM probe. (a) chip bearing a cantilever and (b) cantilever with a tip. Taken from [36].

enables scanning of larger samples, but depending on a particular construction can lead to easier damage of the piezoelement during mounting of the AFM probe.
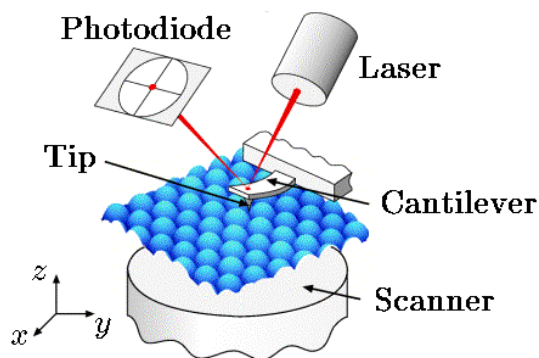
Fig. 3.2: Scheme of AFM imaging. Adapted from [37].

The deflection of the cantilever may be very small, for example several nanometers. In order to visualize such a small variation, optical detection is very often employed. A laser beam is aimed on the back side of the cantilever and is reflected towards segmented (four-quadrant) photodiode. The optical path is much longer than the deflection, thus enabling visualisation of small changes in the cantilever position. Segmented photodiode allows detection of both the vertical and the lateral displacement of the cantilever (torsion).

For stable operation and good resolution (especially for the atomic one), protection against temperature variation, acoustic vibrations, airflow and other possible interference should be ensured.

So far, we were describing the so called contact or static mode, when the tip almost touches the sample and feels repulsive forces. This regime is no longer used in MFM, dynamic modes are employed instead. In the dynamic mode, the cantilever is forced to oscillate near its resonance frequency. The excitation is done

by a piezo-drive-element placed under the chip with the cantilever. The dynamic imaging modes, non-contact and intermittent (tapping), and the contact mode are distinguished according to the tip-sample distance and forces which prevail at these distances as depicted in Figure 3.3. The interaction between atoms of the sample and of the tip is often approximated by the Lennard-Jones 12-6 potential (non-retarded model) [38], which involves the attractive van der Waals interaction (vdW, electrostatic interaction between induced dipoles) and shorter-range repulsive quantum mechanical interaction.
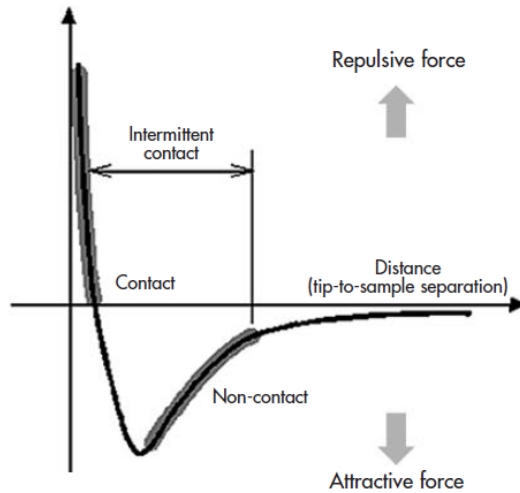
Fig. 3.3: AFM imaging regimes depending of the nature of forces a thus tip-to-sample distance.

The interaction with the sample leads to the change of cantilever oscillation - both amplitude and phase. Although in general the cantilever oscillation is anharmonic (especially in the tapping mode), here we will be concerned with small amplitudes of oscillation and harmonic approximation will be used through out this work.

The vdW forces, giving the topography signal, are not the only ones at play. In air, both the sample and the tip are covered with adsorbed water molecules leading to capillary attraction. Another interaction which comes to play is the electrostatic one which is exploited in Electric Force Microscopy and Kelvin Probe Force Microscopy (sensing potential of the sample surface with a conductive tip). Last but not least, magnetic forces act between magnetic sample and a tip covered with magnetic layer. This interaction is of a major interest in this work.

In general, the cantilever motion is damped, especially in the air. The influence of the damping is prominent in the dynamic mode. It can be significantly reduced when performing the measurement under vacuum, which also leads to an improved sensitivity of the probe. Aside from the damping in the air there might be additional contributions to damping from adsorbed layers on the sample and variable local

mechanic and magnetic dissipation [38]. The last two can provide some information on the sample. An example of a technique making use of the magnetic dissipation when scanning for example across domain walls is the Magnetic dissipation force microscopy. We may describe the damping in terms of the so called quality factor:

$$Q = \frac{\omega E_{\text{mech}}}{P_{\text{loss}}}. \tag{3.1}$$

This is just ratio of mechanical energy stored in the cantilever and the power dissipated during one period of oscillation $T = 2\pi/\omega$, with ω being angular frequency of oscillation. The higher Q, the less damping - enhanced sensitivity.

AFM electronics is controlled via computer and many task can be automated. The system also involves a feedback loop. When the feedback loop is turned on, it keeps constant deflection or oscillation amplitude of the cantilever by adjusting tip-sample distance.

Dominant interaction of the probe with the sample depends on the tip-sample separation as illustrated in Figure 3.4. Magnetic forces are long-range, thus in order to sense mainly the magnetic contribution, the tip-sample distance should be at least 10 nm. In practise, for the separation of topography and long-ranged magnetic contribution, so called lift mode is employed. The tapping/lift mode will be described in section 3.3.
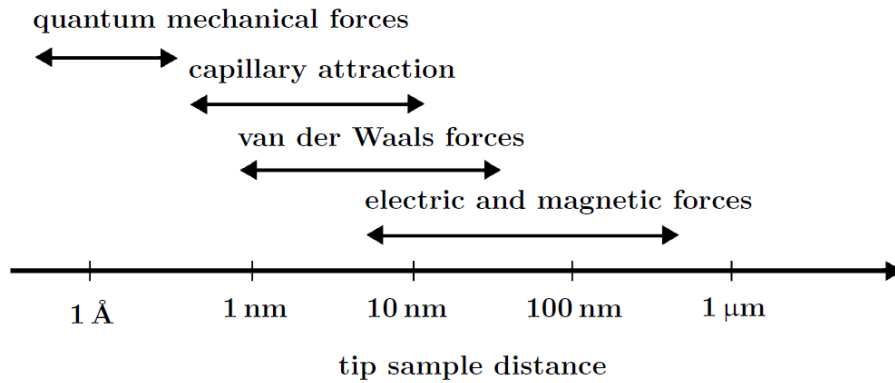
Fig. 3.4: Forces acting on a magnetic tip and tip-sample distances where they prevail. Adapted from [38].

To conclude, the most common scheme involves sensing the force or its gradients with flexural deflection in the contact mode or change in resonance of the cantilever in the dynamic mode. The probe can sense also lateral force acting on the lever. In addition to the flexural resonance, torsional resonance of the cantilever can be exploited for lateral forces imaging. The torsion is excited by two piezo-elements which are excited out-of-phase.

More about AFM can be found in a very nice book by Eaton and West [39].

3.2 Theory of MFM imaging

Magnetic Force Microscopy imaging is based on the interaction of a magnetic sample with a magnetic probe. The most common probes used in these days are the AFM cantilevers with a magnetic layer on the tip. The tip-sample interaction leads to cantilever deflection in the static mode or change in the cantilever oscillation in the dynamic mode. Even in dynamic mode, oscillation frequency of the cantilever (kHz-MHz, in our case usually $\approx 70\,\mathrm{kHz}$) is much lower than the Larmour frequency (GHz) corresponding to the spin or magnetization precession around external magnetic field. In other words, magnetization dynamics takes place at the nanosecond-time-scale so we can suppose that for every tip position (cantilever deflection) the system configuration is in equilibrium. Energy of the system, cantilever mechanical energy is not covered, reads:

$$E = E_{\mathrm{int}} + E_{\mathrm{sample}} + E_{\mathrm{tip}}. \tag{3.2}$$

E_{int} is the Zeeman energy - energy of the sample (with magnetization $\vec{M}_{\mathrm{sample}}$) in the stray field of the tip ($\vec{H}_{\mathrm{tip}}$) or vice versa:

$$E_{\mathrm{int}} = -\mu_0 \iiint\limits_{\mathrm{tip}} \vec{M}_{\mathrm{tip}} \cdot \vec{H}_{\mathrm{sample}} \mathrm{d}V = -\mu_0 \iiint\limits_{\mathrm{sample}} \vec{M}_{\mathrm{sample}} \cdot \vec{H}_{\mathrm{tip}} \mathrm{d}V. \tag{3.3}$$

For a constant tip magnetization, which is close to the measurement with hard magnetic tip magnetized along its axis, equation (3.3) can be replaced, using dipole approximation of the tip [40], by:

$$E_{\mathrm{Z}} = -\vec{\mu}_{\mathrm{tip}} \cdot \mu_0 \vec{H}_{\mathrm{sample}}, \tag{3.4}$$

i.e. by the energy of a magnetic dipole $\vec{\mu}_{\mathrm{tip}}$ in stray field of the sample. Because opposite magnetic charges of the tip dipole are located far away from each other, even the monopole approximation of the tip [40] is sometimes used.

Both sample (E_{sample}) and tip (E_{tip}) energy related to their magnetic states may be described in terms of magnetostatic, exchange and anisotropy energies. Other terms, such as the magnetoelastic energy and the magnetostriction, can be taken into account, but they often play only a minor role.

What we measure is not the energy but the force [1]:

$$\vec{F} = -\vec{\nabla}E. \tag{3.5}$$

In general, both the analytical and the numerical evaluation of the force (or its derivatives in the dynamic mode) is at least difficult if not impossible. Fully 3D

---

[1]To be accurate: we measure cantilever deflection or change of its oscillation amplitude, but force can be deduced if the cantilever stiffness is known.

micromagnetic simulations may shed some light on the problem. Very often hard magnetic (CoCr) tips are employed. If magnetized properly along the tip axis (z direction), their magnetization is well defined and constant [2]. Being interested in derivatives of the energy, we can drop the constant term E_{tip}.

Situation when both the sample and the tip magnetic configuration may change is in most cases so far strongly undesired. It can be avoided by adjusting imaging parameters, mainly by increasing the tip-sample distance but at the expense of a weaker signal and deteriorated resolution.

Commonly it is assumed that both the tip and the sample magnetization do not change during the measurement. In this rigid magnetization approximation we may drop both the tip and the sample energy which are constant and their spatial derivatives vanish. We are left with the sole interaction energy E_{int}. If the magnetization changes as a result of the mutual tip-sample interaction, we speak of a perturbation. This might be the case of a soft magnetic sample probed by a hard magnetic tip with a high magnetic moment.

3.2.1 Alternative description - magnetic charges

Hubert et al. [41] showed that E_{int} may have an alternative and for someone more intuitive form comprising the magnetic volume (ρ_{m}), the surface charges (σ_{m}) of the sample and a magnetic scalar potential (ϕ) of the tip. This form can be derived when inserting [3] $\vec{H}_{\text{tip}} = -\vec{\nabla}\phi_{\text{tip}}$ into the second version of equation (3.3) and integrating by parts over sample's volume/surface [41]:

$$E_{\text{int}} = \iiint\limits_{V} \rho_{\text{m,sample}}\phi_{\text{tip}}\mathrm{d}V + \oiint\limits_{S} \sigma_{\text{m,sample}}\phi_{\text{tip}}\mathrm{d}S. \tag{3.6}$$

Volume and surface charges have been already defined in section 2.1 by (2.2) and (2.3).

According to the nature and strength of tip-sample interactions we can divide contrast phenomena in MFM into these groups [41]:

- Charge contrast
- Susceptibility contrast
- Hysteresis contrast

---

[2]Excluding measurement in a high and/or variable external field.

[3]In case of no conduction currents in the region of interest, field can be described in analogy with the electrostatics as negative gradient of a scalar potential.

Charge contrast

The interaction is weak and neither the sample is modified by the probe nor the probe by the sample. In this case the image gives information about original magnetic charges of the sample. Experimentally this can be achieved with hard magnetic tip of low magnetic moment and large tip-sample distances. The interaction is considered negligible if images taken with the tip magnetized in opposite directions gives opposite contrast, but no other differences are present [9].

Susceptibility contrast

Magnetic charges can be induced by mutual tip-sample interaction. Often the hard magnet influences the softer one. This contrast is reversible and it is very often demonstrated by overall attraction between sample and the probe. Reversibility might be checked again from average of images with opposite polarity probes. Difference of these images very often gives original charge map of the sample [9].

Hysteresis contrast

Strong mutual interaction may lead to irreversible changes, then we speak about hysteresis contrast. Such a strong influence should be avoided as it leads to completely distorted images and artefacts. Thus this corresponds to strong perturbation.

To conclude, in case of no perturbation, MFM maps magnetic charges of the sample.

3.2.2 Static (DC) mode

In static mode we observe deflection of a cantilever carrying a magnetic tip. Here, only the deflection caused by the magnetic force is taken into account. In general case, vdW forces contribute to the deflection as well, however we usually try to minimize their influence by increasing the tip-sample separation. The magnetic force acting on the cantilever is under the assumption of rigid magnetization given by:

$$F_i = -\frac{\partial E_{\text{int}}}{\partial x_i} = \mu_0 \iiint\limits_{\text{tip}} \vec{M}_{\text{tip}} \cdot \frac{\partial \vec{H}_{\text{sample}}}{\partial x_i} dV. \tag{3.7}$$

The tip magnetization usually lies along the tip axis (z direction) and we detect cantilever deflection Δ (shown in Figure 3.5) in z direction as well:

$$\Delta = \frac{F_z}{k} = -\frac{1}{k}\frac{\partial E_{\text{int}}}{\partial z} = \frac{\mu_0}{k} \iiint\limits_{\text{tip}} \vec{M}_{\text{tip}} \cdot \frac{\partial \vec{H}_{\text{sample}}}{\partial z} dV, \tag{3.8}$$

where k is flexural stiffness (force constant) of the cantilever. In dipole approximation of the tip:

$$\Delta = \frac{F_z}{k} \propto \frac{1}{k}\vec{\mu}_{\text{tip}} \cdot \frac{\partial \vec{H}_{\text{sample}}}{\partial z}. \tag{3.9}$$

Thus the signal increases with lower force constant constant of the lever and higher magnetic moment of the tip (either bigger magnetic volume or M_{s}). Due to the reciprocity theorem, bigger magnetic moment of the sample enhances the signal strength. Last but not least, smaller tip-sample distance leads to better signal owing to larger stray field and its spatial derivatives. In general large signal means also considerable mutual interaction and thus potential perturbation, therefore compromise between signal strength and unwanted interaction has to be found.

Not well magnetized tip - ie. tip magnetization deviating from z direction leads to lower signal or sensing also different component of stray field (derivatives) which may aggravate the image interpretation. However, this is not always a drawback, because demagnetized tips reduce perturbations of the sample.

The cantilever senses lateral forces as well, but due to its geometry, the torsion sensitivity is lower, thus mainly F_z deflects the lever.

The minimum detectable force in DC regime for common stiffness of $1\,\text{N/m}$ an at room temperature is $\approx 10^{-11}\,\text{N}$.

Fig. 3.5: Schematic picture of a deflected cantilever.

3.2.3 Dynamic (AC) mode

In the dynamic mode, cantilever with stiffness k and quality factor Q is forced to oscillate near its resonance frequency - with driving frequency ω_{d} and amplitude A_{d}. Force gradients lead to change in effective stiffness and thus resonant frequency ω_{r} of the probe. Amplitude A and phase ϕ are affected as well. This is schematically shown for phase in Figure 3.6. In harmonic approximation, A and ϕ read:

$$A = A_{\text{d}} \frac{\omega_{\text{r}}^2}{\sqrt{\left(\omega_{\text{r}}^2 - \omega_{\text{d}}^2\right)^2 + \left(\omega_{\text{r}}\omega_{\text{d}}/Q\right)^2}}, \tag{3.10}$$

$$\phi = \arctan\left(\frac{\omega_{\text{r}}\omega_d}{Q\left(\omega_{\text{r}}^2 - \omega_{\text{d}}^2\right)}\right). \tag{3.11}$$

New resonant frequency ω_{r} is related to its free oscillation value ω_0 by:
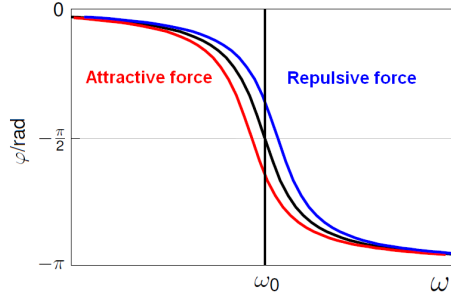
Fig. 3.6: Phase shift (in the harmonic approximation) as a result of force gradient acting on an oscillating cantilever.

$$\omega_{\mathrm{r}} = \omega_0 \sqrt{1 - \frac{1}{k}\frac{\partial F_z}{\partial z}} \approx \omega_0 \left(1 - \frac{1}{2k}\frac{\partial F_z}{\partial z}\right). \tag{3.12}$$

The expansion of the square root to the first order is justified by small relative frequency shifts ($\approx 10^{-4}$) and thus $\frac{1}{k}\frac{\partial F_z}{\partial z}$ is much smaller than 1. In experiment frequency shift is of the order of few Hz, whereas the resonant frequency around $100\,\mathrm{kHz}$.

The phase and frequency shifts are very often detected instead of changes in amplitude. They provide better better acquisition speed and sensitivity as we can detect very small frequency shifts. In some cases frequency detection is preferred to phase as it does not depend on Q - confer (3.11) and (3.12). The reason is that Q is not constant, but varies, with z in particular [42]. For frequency shift detection we need additional feed back loop keeping the phase constant - so called Phase Lock Loop (PLL) [43].

Minimal detectable force gradient is below $10^{-6}\,\mathrm{N/m}$. If we assume $\frac{\partial F}{\partial z} \approx F/z$ and $z = 10\,\mathrm{nm}$, just for the sake of simplicity and comparison with DC, we arrive at force detection limit of $10^{-14}\,\mathrm{N}$. This is much better than DC case with $10^{-11}\,\mathrm{N}$. That is why the dynamic MFM is preferred.

3.2.4   Perturbations

We can distinguish reversible and irreversible perturbations depending on whether or not the sample recovers its initial state once the tip stray field is removed. Examples of the reversible ones are domain wall distortion [44, 45] and stretching or shrinking of closure domains [46]. Irreversible perturbations are represented by probe-induced switching [47, 48] (under external field) or transformation of single domains into flux closure states [49]. Examples of perturbations found during the measurements in this work will be shown in Figures 6.17 and 6.21.

Although high tip-sample interaction is usually unwanted, it can be exploited for local magnetization switching as was demonstrated in [50, 51].

To unravel possible artefacts not only back and forward scan should be compared, but different scan directions should be used as well [51] (left-right, bottom-up, ...). Sometimes even different types of probes are needed.

3.3   Imaging modes

MFM imaging is mostly performed in the dynamic mode and many pass techniques are used - same line is scanned at least two times. More than one scan is motivated by the need for separation of signals coming from the topography, the electrostatic and magnetic interaction. Different parameters might be set for each pass and various signals might be acquired. Aside from classical two pass tapping/lift mode technique, other imaging modes exist:

- Switching magnetization MFM [52, 53],
- Bimodal MFM [54],
- Torsional resonance MFM [55, 56],
- Magnetic dissipation force microscopy [57, 58, 59],
- Magnetic exchange force microscopy [60, 61].

Both switching magnetization and torsional resonance MFM should be suitable for imaging of soft magnets, although no explicit mention of this use has been found. Both bimodal MFM and magnetic dissipation force microscopy have been employed for characterization of soft magnets. Magnetic exchange force microscopy is rather a curiosity than viable imaging technique. It is listed here to show that magnetic interactions can be probed even at atomic scale. In this case short-range quantum mechanical exchange is probed instead of long-range magnetic forces.

Common color coding of the MFM images is as follows:

- dark: attractive force, lower phase, lower frequency,
- bright: repulsive force, higher phase, higher frequency.

No matter what particular technique is used, there are (general) improvements which can enhance almost any of mentioned techniques:

- cantilevers with good mechanical properties= high Q ,
- imaging under vacuum - noise reduction, higher Q [62],
- low temperature (lower thermal noise) and tuning fork (improved sensitivity) [63],
- Phase Lock Loop - frequency modulation [43].

Two pass technique - tapping/lift mode

So called tapping/lift mode, introduced by Digital Instruments [35], is the most commonly employed technique for MFM imaging. It consist of two steps (passes) as is depicted in Figure 3.7. First 'topography' is acquired in the tapping mode - tip stays in the close proximity of the sample, therefore short-range vdW force responsible for topography prevails. Then the same line is scanned again and the tip copies the topography at same elevated distance - lift, thus keeping the tip-sample distance almost constant. Lift at least 10 nm are often required for predomination of magnetic interaction. Note that even negative lift heights are possible and used together with lower amplitude of cantilever oscillation during the second pass (often reduced to one half). Commonly change in amplitude of oscillation is used in the first pass for the topography acquisition, while phase or frequency shift is employed in the second one, which provides a map of magnetic charges.
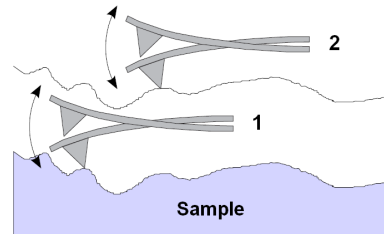
Fig. 3.7: Tapping/lift mode - two pass technique for separation of topography and magnetic interaction. First pass in tapping provides mainly topography, whereas the second one, performed at elevated height and copying the topography, gives signal of magnetic origin. Note that all possible contributions are present in measured signal during both passes. However, they are of different magnitude.

Three-pass technique

In fact, the tapping/lift mode provides not only the magnetic contribution, but the electrostatic as well, because both magnetic and electrostatic forces are dominating at larger distances. Whenever the tip and the sample work functions are different the electrostatic contribution arises. However, it can be suppressed by biasing the sample (tip). *Single bias* is adequate in case of homogeneous sample. Else Kelvin Probe Force Microscopy (KPFM) has to be used in order to determine corresponding electric potential. Thus, the three pass technique involves acquisition of:

1. Topography,
2. Surface electrical potential - corrected for topography,
3. Magnetic Force Microscopy - corrected both for topography and electrostatic interaction.

The description of the technique can be found in NT-MDT catalogue [64] and later in the article by Jaafar et al. [65].

3.4   MFM images of soft magnetic nanostructures

Numerous MFM observations of soft magnets have been reported, we will show just only several of them. Most of the samples are from permalloy - $Ni_{80}Fe_{20}$ (further on only NiFe, but note that the composition may vary slightly). Considerable progress in imaging was reached with observations of the cores of magnetic vortices by Shinjo et al. [20] in 2000. Other observations involve nanodots, patterned thin-film elements and artificial spin-ices. Some challenges remain, particularly imaging of domain walls in 1D nanostructures, nanowires and nanotubes, and magnetic skyrmions.

3.4.1   Magnetic vortices

First observations of the cores of magnetic vortices in permalloy discs were provided by Raabe et al. [66] and even better one by Shinjo et al. [20]. Since that year other MFM measurements have been reported such as behaviour in external field [67], vortices in triangular dots [68] (displayed in Figure 3.8) and asymetric discs [69]. Nice images of vortices both in discs and squares with good explanation supported by simulations were given by García-Martín et al. [49].
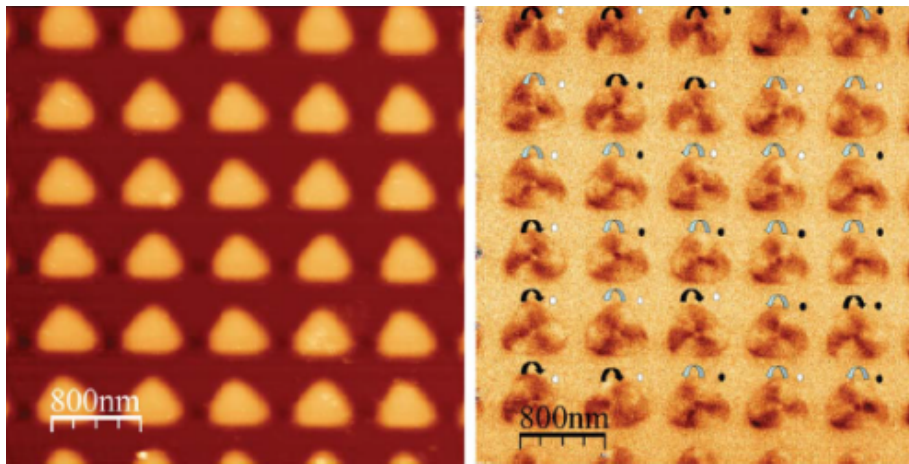
Fig. 3.8: Magnetic vortices in triangular elements. Left: AFM image of an array of triangular elements. Right: corresponding MFM image. Dots and arrows indicate core polarity and circulation of vortices in these elements. Taken from [68].

3.4.2 Permalloy thin-film elements

Special case of magnetic vortices in discs has already been shown above, here we will focus on different shapes, although ellipses are involved as well. Gomez et al. [47] imaged permalloy rectangles with different planar aspect ratio, this is demonstrated in Figure 3.9. Most elements on the diagonal show magnetic vortex and four domain closure pattern. The biggest square has complex multi-domain structure. Other states such as seven domain closure pattern and (near) single domain structure etc.
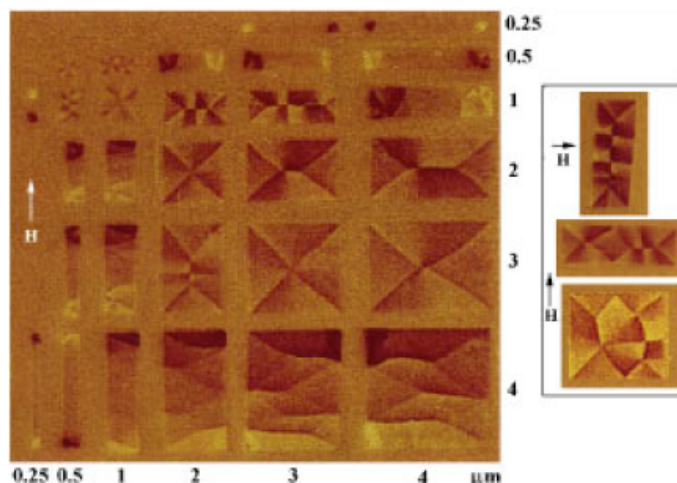
Fig. 3.9: MFM image of array of NiFe islands (height 26 nm) at remanence after applying external magnetic field corresponding to 15 mT (direction indicated by arrow). Dimensions are marked at the borders. Inset shows different states obtained for 3 µm×1 µm rectangles (from top) and 4 µm×4 µm square at the bottom. Taken from [47].

Liou et al. [70] and Felton and coworkers [71] focused on arrays of permalloy ellipses, this is illustrated in Figure 3.10. García et al. [48] studied magnetization switching of small permalloy rectangles under applied field (see Figure 3.11). Another MFM measurement of soft magnetic thin-film elements were reported in [49, 72, 73, 74].

3.4.3 Magnetic nanowires

MFM has been mostly employed for imaging of hard magnetic nanowires - especially from Co prepared by electrodeposition technique [75, 76]. The only found mention of MFM of soft magnetic nanowires is from Wang et al. [77] in 2009 who studied reversal of Fe nanowire with 60 nm in diameter. Tip coated with FePt layer exhibiting very high coercivity was used for imaging in external magnetic field. Results are shown in Figure 3.12. Only magnetic charges at the ends of the wire were imaged.
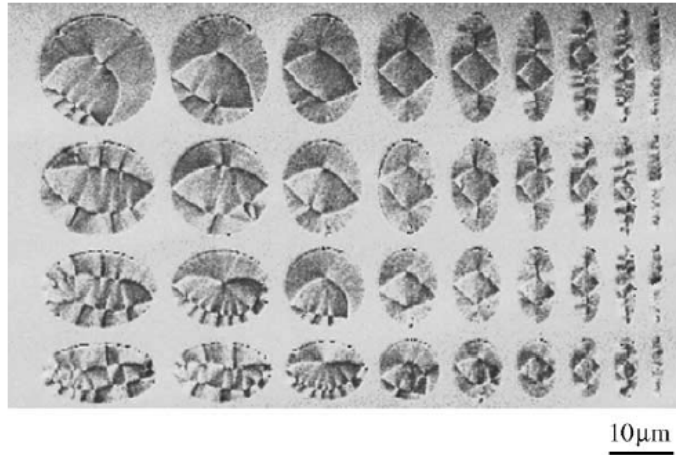
Fig. 3.10: An array of permalloy ellipses (thickness 30 nm) imaged by MFM. Taken from [70].
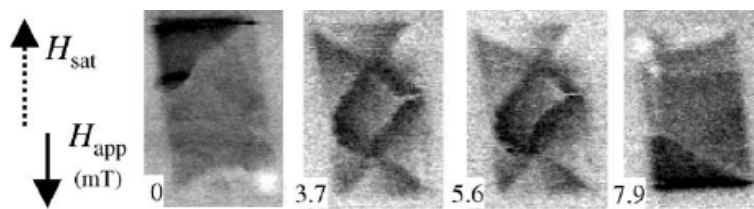
Fig. 3.11: Switching of a $2\,\mu m \times 1\,\mu m \times 16\,nm$ permalloy element observed by MFM. After saturation in one direction, increasing field of opposite direction is applied. Magnetic configuration of the element is transformed from initial S-state to deformed flux-closure diamond state and finally ends in C-state, another near single state configuration, now with magnetization mainly in the direction of the applied field. Adapted from [48].

Although some other contrast is seen along the wire, author attributes it to defects and roughness.
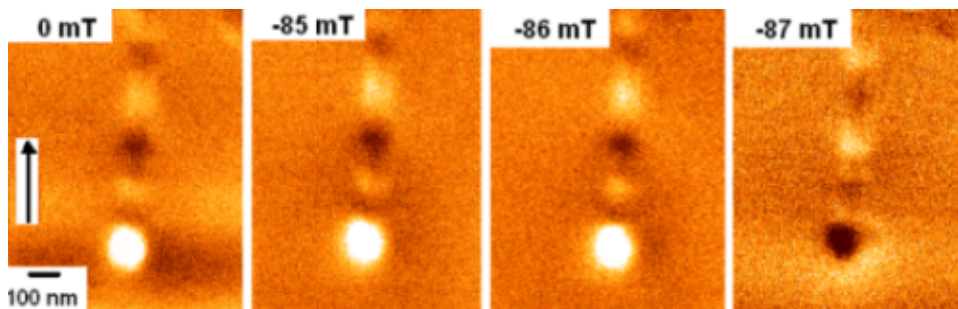
Fig. 3.12: Magnetization reversal in a Fe nanowire. MFM images show one end of the wire with surface charge of the magnetic dipole under different magnitudes of external field (converted to SI and shown as $\mu_0 H$). Other contrast along the nanowire is attributed to roughness and defects. Nothing happens till 86 mT; but slight increase in the field magnitude leads to magnetization reversal depicted by opposite contrast at the end of the wire. Adapted from [77].

Thus, to the best of our knowledge, the first images of domain walls in soft magnetic nanowires have been acquired at Institut Néel by the group of Olivier Fruchart, where the author spent his Erasmus research internship. Images acquired by the author will be demonstrated in section 6.3.

3.4.4 Miscellaneous

Sato and coworkers [74] explored cross and Y-shaped permalloy structures (illustrated in Figure 3.13). If the elements are close to each other, their mutual interaction leads to long-range arrangement of the magnetic dipoles. Nice example of single domain elements which form an array of the so called frustrated magnets (artificial spin-ices) is illustrated in Figure 3.14.

3.5 What influences MFM image?

There are lot of parameters in play which influence the resulting MFM image, mainly in terms of signal strength, resolution and possible perturbation of the magnetic structure with respect to its original state. The major ones are the magnetic probe, lift height in the tapping/lift mode and last but not least reliable microscope with good sensitivity. Here we will provide a list (summary) of parameters and short description of their impact on the imaging. Several of them were already mentioned and another ones will be further discussed in the following sections.
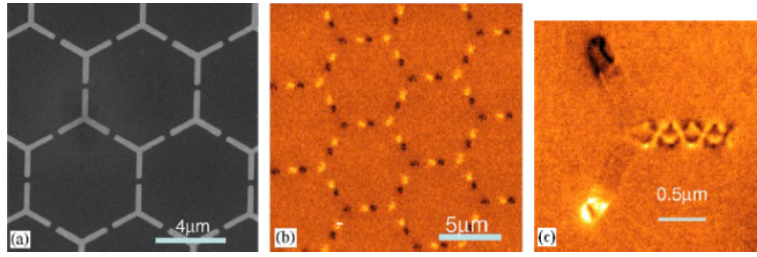
Fig. 3.13: Permalloy Y-shaped elements. (a) SEM micrograph of an array of Y-elements arranged in a honeycomb pattern. (b) Corresponding MFM image. (c) MFM image of a single element which is far away from the others and one of its arms displays flux-closure state. Adapted from [74].
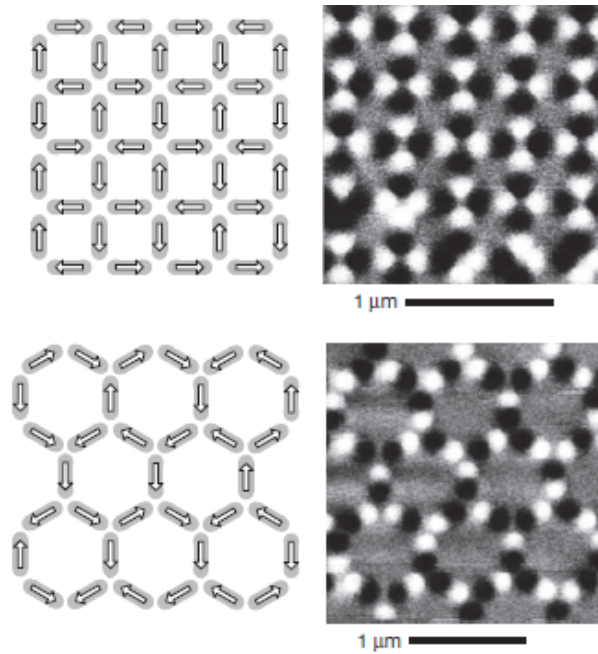
Fig. 3.14: Example of interacting frustrated nanomagnets. Left: scheme of array of elements with their magnetization depicted by arrows. Right: corresponding MFM image of the array. Adapted from [18].

Sample

The sample plays a significant role in the imaging. For sure, the signal from thick hard magnet layer is higher then from a domain wall in a soft magnetic nanowire with a diameter of 50 nm. An inappropriate tip-sample combination may lead to artefacts and/or distortion of the imaged magnetic configuration. Care should be taken when imaging a hard magnet with a soft tip and vice-versa. Even though the tapping/lift mode technique enables imaging of quite rough surfaces, the flat samples are easier to image and interpret.

Magnetic probe

Magnetic probe - cantilever bearing sharp magnetic tip - is the key for good imaging and will be covered in the next chapter and parameters particularly in section 4.1. For obtaining nice images, magnetic coating and its thickness should be tailored to a particular sample. Generally sharp tips with a low magnetic moment give better resolution, but a slightly lower signal.

Microscope and imaging parameters

It is not surprising that the microscope itself determines the quality of acquired images. The microscope should be well calibrated and in a good overall state. It should not contain magnetic parts in the vicinity of the sample, which may influence the measurement. When performing the measurement in an external magnetic field, no magnetic parts at all shall be present. High sensitivity and available imaging modes are of importance as well. Nowadays, almost all AFMs enable the tapping/lift mode with possibility of setting independent parameters for both scans - mainly the amplitude of the cantilever oscillation.

Hitting the sample surface during the tip approach (crash-landing) should be avoided, especially for super-sharp tips which are more susceptible to damage and complete destruction. Therefore slower, finer approach should be performed.

An appropriate choice of the driving (excitation) frequency is necessary for the imaging. The frequency is commonly selected close to the initial resonant frequency of the probe when it is far from the sample. In the air and for the flexural oscillation, finding the peak is easy and very often automated. Complication arises in liquids or in case of higher harmonics or torsional oscillations.

The most important imaging parameter is the tip-sample distance, which is given by the lift height and the oscillation amplitude. The lower the is the distance, the higher is the signal and the better is the resolution. The resolution depends mainly

on the probe, further on scan size, number of points in the image, scan speed, scanner non-linearity correction, etc.

3.6   Comparison with other magnetic imaging techniques

Main virtues and drawback of MFM are summarized below:

+ good (medium) resolution: 15 nm (some claims for 10 nm resolution exist [78]),
+ measurement in various environments (vacuum, magnetic field, low temperatures, liquids),
+ no special sample preparation required,
+ observation of large and rough samples,
+ moderate (lower) cost compared to other magnetic imaging techniques,
- not so easy data interpretation, especially data quantification requires simulations,
- possible influence of the sample during measurement (tip dependent),
- slow (acquisition typically several minutes+).

Table 3.1 shows how MFM stands in comparison with other imaging techniques. Their description can be found in [79], here only very short summary will be given. Spin-Polarized Scanning Tunnelling Microscopy (SP-STM) is based on spin-dependent tunnelling of current through small gap between conductive magnetic sample and very sharp (magnetic) tip (wire). Scanning Electron Microscopy with Polarization Analysis (SEMPA) probes sample with electron beam and detects polarization of electrons emitted by the ferromagnetic sample. Transmission Electron Microscopy (TEM) provides magnetic information especially in holographic or differential setup. The family of X-ray techniques is large and has many members. X-ray-Magnetic Circular Dichroism - PhotoEmission Electron Microscopy (XMCD-PEEM) is a combined synchrotron technique. XMCD probes difference in absorption of left and right circularly polarized X-rays by magnetic sample. Absorbed Y-rays lead to emission of photoelectrons which are detected by PEEM. Further Magnetic Transmission X-Ray Microscopy (MTXM) and Scanning Transmission X-Ray Microscopy (STXM) are employed for probing magnetic nanostructures with X-rays [80].

Although MFM is quite slow and indirect method of magnetization, it provides reasonable resolution and it is quite versatile.

Tab. 3.1: Comparison of MFM with several other imaging techniques [9, 81]. Measurement stands for determination of the magnetization. X-ray techniques involve XCMD-PEEM, MTXM, STXM etc. [80]. Note that rather no external magnetic field should be applied in XMCD-PEEM.

	MFM	SP-STM	SEMPA	TEM	X-ray
Resolution	10-15 nm	< 1 nm	10 nm	1-2 nm	25 nm ($\rightarrow$10 nm)
Measurement	indirect	direct	quantitative	quantitative	direct
Element sensitive	no	yes	no	limited	yes
Versatile	yes	no	limited	limited	yes
Necessary investment	moderate	high	high	very high	extremely high
Measurement in field	limited	yes	only local	limited	yes
Dynamics observation	no	no	no	limited	yes

4 PROBES FOR MFM

In pioneering works, etched ferromagnetic wires (Fe, Ni) served as probes for MFM [2]. Due to the high amount of the magnetic material, these tips provided only low resolution (100 nm). Their high magnetic moment significantly disturbed the sample magnetization especially in case of soft magnets. On the other hand, MFM was mostly concerned with hard magnetic recording media, so this potential influence played only minor role. Nowadays, MFM probes based on AFM Si/Si_3N_4 cantilevers are used instead. They offer better resolution, have lower influence on the sample magnetization and enable batch fabrication [34].

Resolution of the MFM is mostly determined by the probe used for imaging. Improvements in probe preparation, optimal magnetic layer thickness for a given material, use of a Focused Ion Beam (FIB) and nanotubes contributed to resolution enhancement in the past several years (schemed in Figure 4.1).
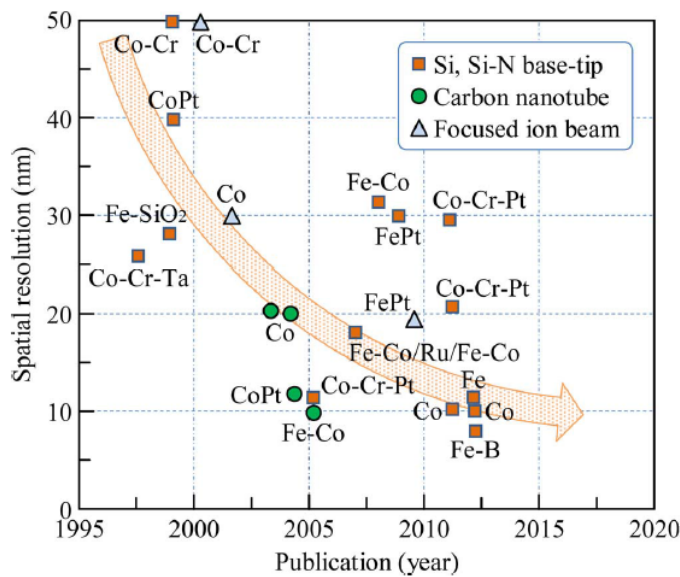
Fig. 4.1: Improvement of MFM spatial resolution. Taken from [82].

Magnetic material can be put on the tip by various methods:

- **evaporation/sputtering** [34, 82, 83, 84] (+FIB treatment),
- electrochemical deposition+FIB treatment [85], localized electrodeposition using AFM with fluid cell [86],
- carbon nanotubes with embedded magnetic nanowires [87] or coated nanotubes on the tip [88],
- magnetic nanowires [49, 89] / nanoparticles [90] on the tip,
- Electron Beam Induced Deposition - mainly Co [4].

Evaporation/sputtering of magnetic thin films (coatings) on the tip is the most frequently used method due to its relative ease, reasonable reproducibility and possibility of batch preparation. Sputtering of a magnetic coating (NiFe, Co, CoCr) will be used in this work for MFM probes preparation, thus, we will discuss this method and related issues further in section 4.2. Instrumentation will be covered in section 5.1.2 and experiments in 6.5.

FIB can be employed for several task: tip sharpening before and after the application of magnetic material on the tip, fabrication of nanoparticles at the tip apex, even for material deposition by FIB sputtering of small targets directly in FIB/SEM apparatus [84]. FIB can be also used for Ion Beam Induced Deposition.

We will start this chapter by addressing MFM probe parameters important for the imaging. As pointed out above, we will continue with discussion of MFM probes preparation by means of coating the tip with various (magnetic) layers. Finally, we will provide some information about commercial MFM probes, that were used for the MFM imaging in this work for comparison with prepared probes.

4.1 Probe parameters

Cantilever

Cantilevers with medium spring constant (several N/m, typical value $2\,\mathrm{N/m}$) corresponding to medium resonant frequency (50-100 kHz, typical value $70\,\mathrm{kHz}$) are very often employed for MFM imaging. Lower stiffness provides better sensitivity [91], but too soft cantilevers ($k << 1\,\mathrm{N/m}$) should be avoided as there is high probability of *jumping into contact* and consequent tip damage. Stiffer probes are sometimes used for permanent magnets. Back side of the lever bears reflective coating which enhances the detection of lower signals. Sensitivity is also improved by a good geometry and mechanical properties of the lever which are described usually in terms of the quality factor.

Magnetic coating

Various materials are used for the tip coating as we will see in next section. Material and layer thickness determine magnetic moment of the probe and its coercivity. Lower magnetic moment provides better resolution, but lower signal as well. Note that the effective magnetic moment is influenced by the tip magnetization process and is reduced by misalignment during the process and demagnetization. For some applications so called superparamagnetic particles are place on the tip [92].

Coercivity of the coating is often in tens of mT, lower (NiFe, NiCo coatings) is used for soft magnetic samples. High coercivity is needed for imaging of permanent

magnets or measurement under external field. CoPt is a common choice in this case, but also very high coercivity corresponding to 1.1 T was reported for multilayers such as CrRu/MgO/FePt [93].

Aside from the magnetic coating, protective coatings against mechanical wear and oxidation are used, although not very often. Probe life-time can also be prolonged by a storage in a low humidity environment (storage under low vacuum).

Tip

Tip shape and the radius of curvature of its apex determine the resolution both in topography and magnetic imaging. Generally low cone angle and high aspect ratio of the tip provide better resolution and enables reliable imaging of high aspect ratio structures [91]. Magnetic coating makes the tip more blunt and thus reduces resolution in the topography. Standard tips have tip radius and the resolution near 50 nm. For high resolution ($\leq$25 nm) super-sharp tips (often radius of 5 nm for bare and 15 nm for coated tip) can be employed. Unfortunately, super-sharp tips are very fragile, easy to destroy and sometimes difficult to use, not speaking of high price.

To summarize: high coercivity tips (CoCr, CoPt) and stiff cantilevers (high f_r) are used for permanent magnets, whereas medium stiffness cantilevers with low moment tips (and sometimes also low coercivity) for high resolution and soft samples.

4.2 Tip coating

Various magnetic materials, their alloys and even multilayers are used for the coating of MFM probes. The choice depends on application. The most common coating is CoCr as will be demonstrated below and most commercial MFM probes bear just this coating. Soft magnetic layers, NiFe and less often NiCo, are used for soft magnets [34]. FePt is an example of layer with very high coercivity, therefore very suitable for imaging in (higher) external magnetic field. Other used coatings: CoCrPt [51, 82], Co, CoPt [34, 82], FeCo, FePd [82], Fe [50], FeB [94]. Example of multilayers is CrRu/MgO/FePt system [93]. Other informations about magnetic coatings for MFM probes can be found in [95, 96, 97]. Hard magnetic tips like CoCr are better for observation of domains, whereas the soft tips (NiFe) for domain walls as they respond to the total stray field of the sample [34].

Babcock et al. [83] studied the dependence of the MFM signal strength, represented by the shift in resonant frequency of the probe, on the thickness of $Co_{85}Cr_{15}$ coating. This alloy posses coercivity of $\approx$39.8 kA/m (500 Oe, sufficient for most of applications) and magnetization of 400 kA/m (400 emu/cm^3). They probed thickness range of 15-150 nm and found an optimal value, i.e. for highest sensitivity and

lowest corresponding thickness, to lie around 50 nm (see Figure 4.2). Commercial probes are being coated just with CoCr alloy, standard probes bear layer of 40-50 nm. Most manufacturers do not provide precise composition, neither thickness of their magnetic probe coating. However, aiming for optimal thickness value near 50 nm is obvious. Babcock also demonstrated possibility of in-plane-magnetization of the tip for better lateral sensitivity of the tip.
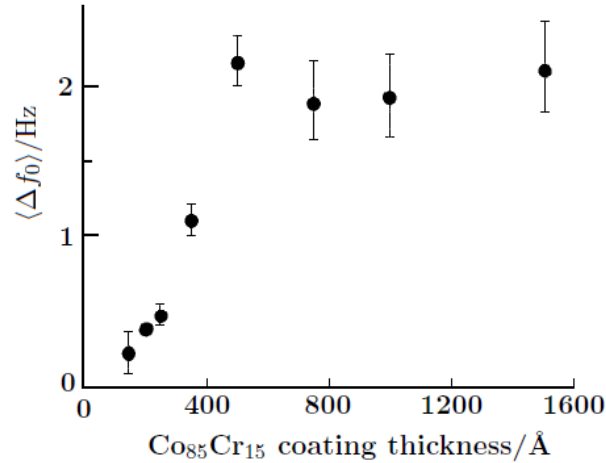
Fig. 4.2: Dependence of the MFM sensitivity (resonant frequency shift of the oscillating probe) on $Co_{85}Cr_{15}$ coating thickness. In probed range of 15-150 nm, roughly linear increase of the sensitivity with the thickness was observed up to the critical thickness of 50 nm. Thicker layers do not provide any further improvement. Batches of at least 5 tips were used for each thickness. Adapted from [83].

Futamoto et al. [82] studied the dependence of resolution on magnetic coating thickness for various materials. They found out the optimal coating thickness (optimal with respect to resolution as well, not only signal strength as in the case of Babcock's study) to be 20 nm for the following materials: Co, Fe-Co, Fe-Pd, Co-Pt. Example of this study for Co coating is illustrated in Figure 4.3. Thinner coatings suffered from weak signal, whereas thicker ones led to deteriorated resolution due to too large tip radius. Here it is necessary to note, that they coated super-sharp tips with tip radius of 4 nm. This implies that optimal thickness for coating common tips (radius of ≤ 10 nm) might be slightly different (lower). Their work (including coercivity of layers) is great from a material point of view, but their claims for sub 10 nm resolution are questionable because of improper definition of spatial resolution used in their article(s). It is not a surprise that the commercial MFM low moment probes bear 15-20nm coating (CoCr). In principle, thinner coatings should provide even better resolution, but corresponding weaker signal has to be compensated by lower lift heights and enhanced detection. Appropriate vibration and other interference insulation is a must in such a case.

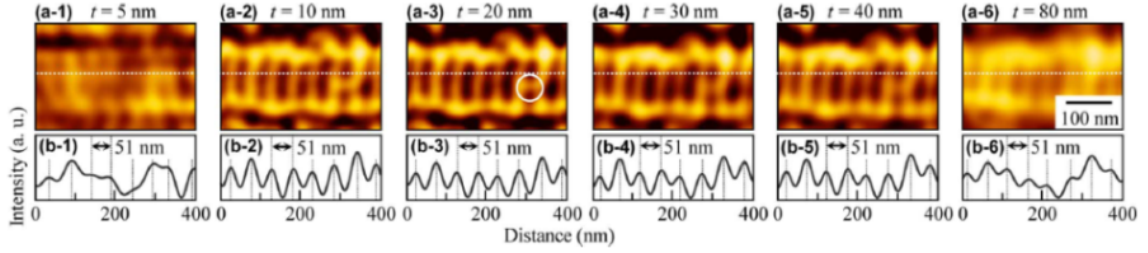*Fig. 4.3: Comparison of MFM images (under vacuum and at room temperature) of a perpendicular recording medium for various Co coating thickness. Base Si super-sharp tips (tip radius 4 nm) were coated with (a-1) 5, (a-2) 10, (a-3) 20, (a-4) 30, (a-5) 40, and (a-6) 80 nm of Co. (a) MFM images and (b) appropriate profiles measured along the dotted lines in (a). 20nm thickness was recognized as the optimal one. Taken from [82].*

4.2.1 Choice of tip side to be coated

We are very often interested in sensing the out-of-plane components of the magnetic stray field. In this case magnetization of the tip should lie in this direction, usually denoted as z. However, various shapes of tips exist and they are not symmetric (around z axis) in all cases. Coating the whole probe might not be the best idea - effective tip moment is increased and magnetization of the tip might not be well defined and do not necessary lie along the z axis. Most of the tips have a pyramidal shape with at least one side (plane, or tip side) tilted 10-15° with respect to the z direction. This tilt compensates mounting the chip with the probe at a similar angle in the microscope, which preventing the other parts of the cantilever from touching the sample. When coating this side of the tip with thin magnetic layer, its magnetization should lie in-plane of this side. This means in the z direction when the probe is mounted on the microscope. Comparison of images obtained with one and two side-coated tip is shown in Figure 4.4. It is obvious that coating (improperly) more sides can lead to sensing not only out-of-plane, but in-plane components of the stray field, thus making the image analysis even more difficult.

4.2.2 Tips for imaging of soft magnets

Most authors agree that probes with low magnetic moment (LM) are needed in order not to influence the soft magnetic samples. *Low* magnetic moment is not strictly defined, it is just lower than the moment of the standard CoCr coating (40-50 nm thick). LM coating is very often equivalent to <20-25 nm of CoCr. Some examples of LM coatings from the literature:

- 25 nm CoCr [68],
- 12 and 24 nm CoCrPt [62],
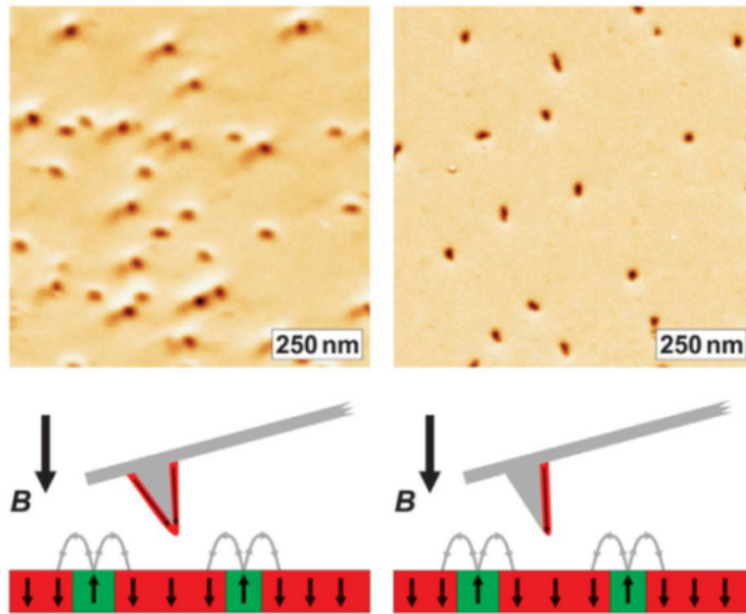
Fig. 4.4: Comparison of images obtained with two and one-side coated tips. Left: two side coated tip - ie. MFM tip with mixed out-of-plane and in-plane sensitivity. Right: one-side coated tip with pure out-of-plane sensitivity. Both MFM images of $La_{0.7}Ca_{0.3}MnO_3/LaAlO_3$ sample (with out of plane magnetization) were obtained at 5.1 K in external field of 0.295 T. Even though not the same area is imaged in both cases, one-side-coated tip gives clearly better image without further intriguing contrast. Taken from [78].

- $12 - 18\,\text{nm Co}_{80}\text{Cr}_{20}$ [49]
- CoPt $7\,\text{nm}$ [91],
- $20\,\text{nm}$ CoCr, $20\,\text{nm}$ NiFe, $20\,\text{nm}$ NiCo [72].

Getlawi and co-workes [72] showed that tips with low coercivity coating - NiFe and NiCo - do not influence so much soft magnetic samples as the CoCr coating does.

Memmert et al. [32] summarize strategies used to minimize the soft sample perturbations induced by the tip. Aside from reducing magnetic volume (thickness) of the coating at the tip apex, they mention two other approaches. Demagnetizing the probe before measurement and use of low-coercivity probes. Memmert notes that in case of low-coercivity probes, the tip moment aligns with the local stray field of the sample and therefore less information is detected. Of course, this might be severe disadvantage in some cases. Further, he reminds that most (irreversible) perturbations happen during the acquisition of the topography image performed in tapping mode. To suppress this perturbation he modifies the probe with deposition of 50nm carbon spacer on top of the tip with electron beam of the SEM. He shows that with such a spacer, increasing the tip-sample separation even during topography imaging, soft magnetic samples can be measured even with standard tip bearing 50 nm of CoCr. But there is a price - lower lateral resolution. On the other hand, it is not necessary for the spacer to be as large as $50\,\text{nm}\ldots$

4.3 Commercial MFM probes

Not only for comparison, commercial probes were acquired and used for imaging in this work. Manufacturers (suppliers) and probes follow:

- Nanosensors:
    - PPP-MFMR (standard, medium moment)
    - PPP-LM-MFMR (low moment)
    - SSS-MFMR (super-sharp, even lower moment)
- Asylum: ASYMFMLM (low moment)
- Bruker: MESP (medium moment)

Selected properties of the commercial probes are summarized in Table 4.1. The data are based on the information provided by suppliers. Parameters such as magnetic layer composition, thickness and the whole coating process are not given in all cases (proprietary). It is necessary to note that magnetic properties of the coating are estimated from measurement performed on the layer on a flat substrate. This means that properties of the coating on the tip might be different. For example, Carl and co-workers [98] inspected directly MESP tips and found out that the coercivity is in fact lower (27-36 mT instead of manufacturer's $40\,\text{mT}$). These parameters may

vary quite significantly for different batches. Carl further pointed out that magnetic properties of the MFM tip, or better to say its part involved in the imaging, should be measured using MFM technique itself. Inferring this data from magnetometry or even characterising layer on a flat substrate may lead to significant differences (such as factor of 2). Carl proposed MFM imaging of special current carrying gold rings as method for determining hysteresis loop of the MFM tips [98]. In general the thickness of the coating on the tip can be lower than the nominal one. Knowledge of probe properties is helpful for realization of a particular experiment and crucial for quantitative measurements.

Tab. 4.1: Parameters of selected commercial MFM probes: cantilever stiffness k, resonant frequency f_{r}, thickness of the CoCr magnetic coating t, coercivity H_{c}, effective magnetic moment μ and guaranteed tip radius r. Some manufactures do not provide magnetic layer thickness and precise composition. Except ASYMFMLM, magnetic coating thickness is estimated from guaranteed tip radius and radius of a bare tip (in general $< 10\,nm$, super-sharp $< 5\,nm$). Other data were taken from manufacturers websites [99, 100] and probe datasheet [101]. Magnetic properties were determined from measurement on a flat surface - ie not directly from the tip. Reflective coating thickness of the Bruker MESP probe is not provided as well, being probably the same as in the case of magnetic coating - estimated in the range of 40-50\,nm CoCr. Reflective coating is 30\,nm Al in case of Nanosensors probes and 15\,nm CoCr for ASYMFMLM probe.

Probe	$k/(\mathrm{Nm}^{-1})$	$f_{\mathrm{r}}/\mathrm{kHz}$	t/nm	$\mu_0 H_{\mathrm{c}}/\mathrm{mT}$	$\mu/(\mathrm{aA \cdot m}^2)$	r/nm
PPP-MFMR	2.8	75	$\approx 40\,\mathrm{nm}$	≈ 30	≈ 100	< 50
PPP-LM-MFMR	2.8	75	$\approx 20\,\mathrm{nm}$	≈ 25	≈ 50	< 30
SSS-MFMR	2.8	75	$\approx 10\,\mathrm{nm}$	≈ 12.5	≈ 25	< 15
ASYMFMLM	2	70	$15\,\mathrm{nm}$ CoCr	≈ 40	≈ 30	< 25
Bruker MESP	2.8	75	$\approx 40 - 50\,\mathrm{nm}$	≈ 40	≈ 100	< 50

5 METHODS & INSTRUMENTATION

In this chapter we will rather briefly cover the techniques used in experiments and the modelling of magnetization in measured structures. Experiments involve the fabrication of samples, especially NiFe nanowires, and the probes for MFM; further inspection of both samples and probes and MFM measurements. Finally, we will describe micromagnetic simulations in the finite difference solver OOMMF.

5.1 Fabrication techniques

In this section we will give a description of the fabrication of the magnetic nanowires by a electrochemical deposition into nanoporous alumina templates and ion beam sputtering used for the preparation of the magnetic probes and an antidot array.

Methods which were not used by the author, will not be discussed. This concerns EBL [102] patterning of NiFe thin films done by Marek Vaňatka and Atomic Layer Deposition (ALD) [103] of aluminium oxide performed by Ing. Miroslav Kolíbal, Ph. D.

5.1.1 Electrodeposition of NiFe nanowires

Electrodeposition of metallic layers/coatings is widely used in industry. An electro-chemical cell for the electroplating consist of at least two conductors, e.g. sheets of metal, immersed in a electrolyte - ionic conductor. Example of a such electrolyte is a solution or melt of a metallic salt plus some additives. By applying a voltage across these two electrodes it is possible to shift the Fermi level of electrons, i.e. the electrochemical potential $\overline{\mu}$, in electrodes and reduce metal cations from the electrolyte at the surface of negatively biased electrode - so called cathode. Commonly, three-electrode electrochemical cell is used for the electrodeposition.

The electrode where the desired reaction, reduction, takes place is named Working Electrode (WE), the other one Counter Electrode (CE, here anode). The CE is usually from a chemically inert material such as platinum, which prevents unwanted interference with the desired reaction. Complementary redox reaction, oxidation, takes place at the CE. Third electrode, Reference Electrode (RE), serves as a reference for measurement of the WE electrical potential. For the cell setup see Figure 5.1(a) and photos in Figure 5.2. Reader interested in further details and information about electrochemical deposition can consult author's bachelor thesis [104], where other references can be found.

In order to prepare nanowires instead of continuous layer, the nucleation and the growth of the metal has to be spatially restricted. One of proven possibilities is to use

electrically non-conductive nanoporous alumina template - depicted in Figure 5.1(b) - placed on WE. The rest of the immersed WE area is electrically insulated by a resin or an insulating tape in order to inhibit undesired deposition.
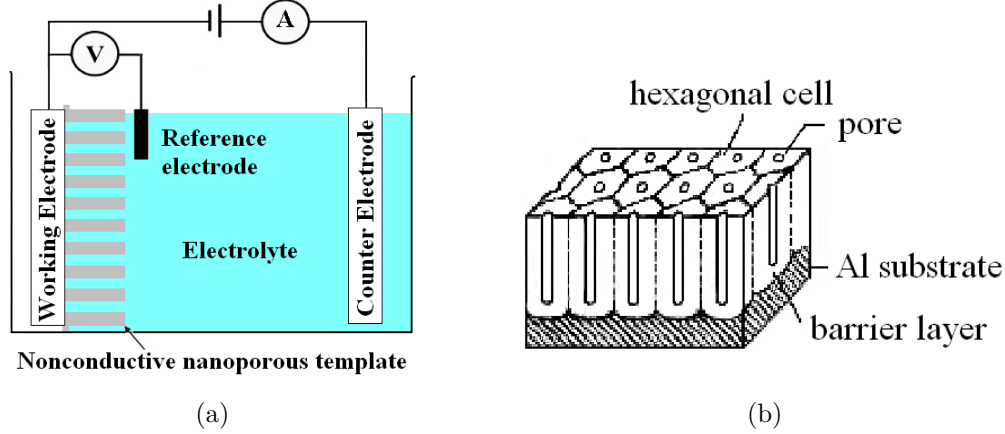

Fig. 5.1: (a) Electrochemical cell. (b) Nanoporous alumina template; Al substrate, barrier layer has to be removed and Au layer sputtered on the bottom side prior to the deposition.

Pulsed electrodeposition of NiFe nanowires [105] into the pores of the template was carried out with a potentiostat PAR 273A and NI PCI 6229 data acquisition card, experiment was controlled by a LabVIEW programme created by the author. Another programme was created for the template fabrication. The templates were provided by Laurent Cagnon (Institut Néel). The pulsed electrodeposition should give better composition homogeneity than the classical DC electrodeposition.

The aqueous solution (pH 3.0 ± 0.2) for the deposition of NiFe consists of $45.0\,g/l$ H_3BO_3, $300.0\,g/l$ $NiSO_4 \cdot 6H_2O$, $45.0\,g/l$ $NiCl_2 \cdot 6H_2O$ and $6.0\,g/l$ $FeSO_4 \cdot 7H_2O$ [105]. Iron content is kept low due to the so called anomalous codeposition for iron group elements, where the deposition of less noble element, here Fe, is favoured. To the best of author's knowledge, complete mechanism of this anomaly is not fully understood yet.

The deposition was conducted at ambient conditions, i.e. no inert atmosphere, so a higher iron content in the electrolyte and longer pulse delays might be necessary to get the same composition as in [105]. Fe yield slightly lower than 20 atomic percent (rest Ni) is expected in our case due to Fe^{2+} oxidation. Other parameters are summarized below:

- **working electrode**: golden layer on AAM 241 nanoporous alumina template,
- **counter electrode**: platinum mesh (higher surface area than WE),
- **reference electrode**: Saturated Calomel Electrode (SCE),
- **pulse**: -1245 mV for 10 ms followed by -745 mV for 100 ms (potential vs SCE),
- **duration**: 7200 s (pulses continuously repeated during the duration).

Fig. 5.2: Electrochemical deposition of nanowires. From the left: potentiostat (instrument for electrochemical experiments), deposition cell with electrodes and salts used for the electrolyte preparation.

In order to release the nanowires, the template was dissolved in 2M sodium hydroxide. Afterwards, nanowires were collected with a permanent magnet and rinsed thoroughly with demineralized water and isopropyl alcohol (IPA) and finally stored therein. A drop of IPA with dispersed nanowires was transferred on patterned Si substrate via micropipette. The magnet was placed underneath the substrate and IPA was removed by air-blowing. If done properly other effect comes together with getting rid of IPA - part of the isolated nanowires is bent. Bent parts are ideal for DW trapping and on the other hand, bundles of non-dispersed nanowires can be used for easier (composition) analysis.

5.1.2   Ion beam sputter deposition - Kaufman apparatus

Ion Beam Sputter (IBS) deposition uses accelerated ions for sputtering a target from various materials in high vacuum. The sputtered atoms and clusters are deposited on the sample as well as on a quartz crystal of a thicknessmeter. From a change in the resonant frequency of the crystal and knowledge of the sputtered material we can deduce the thickness of the deposited layer. In Kaufman apparatus at IPE ion source of the same name is used. More information about the apparatus can be found in [106]. The base pressure is of the order of 10^{-5} Pa, typical deposition rate is 1-2 Å/s and three targets can be mounted on the holder, but only one used at the same time. Most of the time, two out of three positions on the target holder are occupied by Au and Ti, thus only one position is available for other materials, which makes the fabrication of magnetic (multi)layers more difficult and slows down the systematic preparation. Exchange of targets, ie. use of other target than the ones in the apparatus, requires venting of the chamber. Sufficient vacuum needed for the deposition of magnetic layers can be recovered at best after one day. The exchange of targets sometimes leads to a tilt of the whole holder and the material is

not deposited directly in a direction perpendicular to the sample holder. Moreover, there was a long term and repeated shut-down of the apparatus, which forestalled more systematic preparation of magnetic probes for MFM.

Following targets are available at the institute and were used in the experiments: NiFe, Co, CoCr for the magnetic, Al and Ti for the protective cover layer. Target from Pt, which is often used for adjustment of magnetic coatings of the MFM probes, has not been acquired so far.

5.1.3   Choice of bare/base AFM probes

Driving forces for the preparation of own MFM probes are mainly necessity of custom tips optimized for a particular sample and last but not least possibility of saving some money when preparing a larger number of probes. For example price of a low moment probe is about $50 \, €$, super-sharp with better resolution over $100 \, €$. Note that prices differ depending on suppliers and there are discounts for bulk orders.

Among other commercial AFM probes from Micro-Masch, NT-MDT, Bruker etc., two were selected for further consideration - Asylum (Olympus) AC240TS and Nanosensors PPP-FMR. The tips from Asylum and Nanosensors belongs to the most favourite, frequently used and mentioned in the literature [49, 68, 107]. Both have similar characteristics as shown in Table 5.1, Figures 5.3 and 5.4. Finally, Asylum AC240TS tips were chosen based on these factors:

- good experience during the internship at Institut Néel,
- smaller dispersion of the characteristic values such as stiffness,
- slightly better reflective coating and thus signal to noise ratio,
- tip position just at the end of the microlever - easier aiming based on the optical microscope view.

Probes from both suppliers have good mechanical properties - high Q. They are fabricated from doped Si for a better charge dissipation and therefore reduce the contribution of electrostatic forces during the measurement. Both probes have good reflective Al coating, PPP-FMR $30 \, nm$ and AC240TS even $100 \, nm$ of Al.

Tab. 5.1: Commercial AFM force modulation probes - parameters [36, 108]: tip radius r, cantilever stiffness k, resonant frequency f_r, length L, width W and thickness t. Typical values are given in bold.

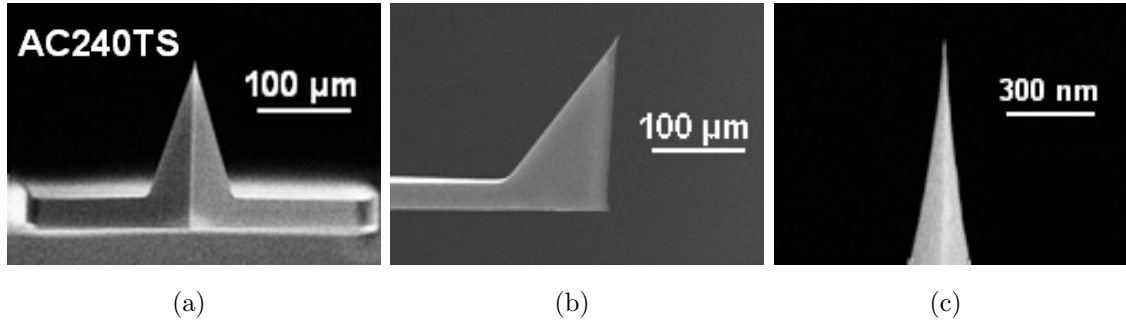| Probe	r/nm	k/(Nm^{-1})	f_r/kHz	L/µm	W/µm	t/µm
AC240TS	< 10	**2** (0.5-4.4)	**70** (50-90)	**240**	**40**	**2.3**
PPP-FMR	< 10	**2.8** (0.5-9.5)	**75** (45-115)	**225**	**28**	**3**

Fig. 5.3: Asylum AC240TS probe [36]. (a) front side of the tip, (b) side view, (c) tip apex.
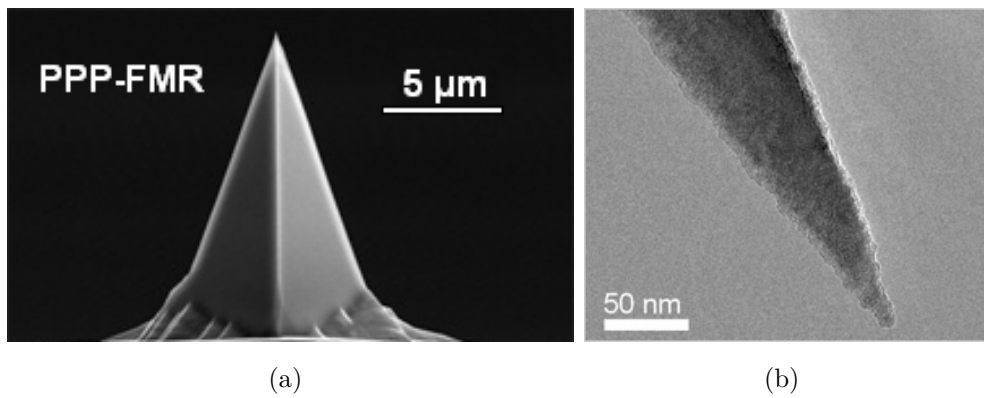

Fig. 5.4: Nanosensors PPP-FMR probe [108]. (a) front side of the tip, (b) tip apex.

5.1.4 Preparation of MFM probes

As stated above, three ferromagnetic coatings were available and used, namely hard Co, CoCr and soft magnetic NiFe. Aside from the magnetic film, a non-magnetic cover layer from AlO_x was used in some cases. Ti cover was tried as well. The role of AlO_x coating is following:

- protection against mechanical wear and oxidation of the magnetic layer,
- spacer that increases the distance between the sample and the magnetic part of the tip thus leading to lower tip influence on the sample, even during the topography scan,
- influence on the magnetic properties of the coating, but probably prominent only for ultra-thin magnetic coatings.

AC240TS probes were mounted on a sample holder with a Kapton tape, because not any tape/glue is compatible with high vacuum. A flat Si substrate, which serves as a reference and enables easier study of coating properties, was added as well. However, note that magnetic properties of the coated probe are generally different from properties of the coating on the flat substrate. The deposition angle was slightly varied, but it was mostly perpendicular to the sample holder surface. No significant differences were observed within used tilts. AFM probes mounted on the holder are captured in Figure 5.5.
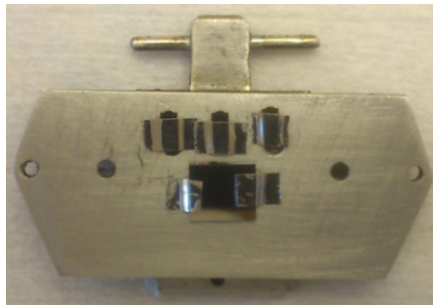
Fig. 5.5: Sample holder for Kaufman deposition apparatus with the AC240TS probes and a flat Si reference substrate.

After the preparation, the MFM tips were stored in a vacuum desiccator in order to avoid the undesired oxidation and other deterioration of the magnetic material.

5.2 Characterisation techniques

AFM/MFM was used for the measurement of soft magnetic - NiFe - nanostructures both with commercial and *home-coated* probes. The prepared probes and

samples were inspected by Scanning Electron Microscopy and Energy Dispersive X-ray spectroscopy. Last, Magneto-Optical Kerr Effect was exploited for a qualitative characterisation of the magnetic coatings deposited on flat substrates.

5.2.1 Atomic/magnetic force microscopy

Atomic and magnetic force microscopies have already been described, so we will make only small note on the instrumentation which was used in this work:

- NT-MDT Ntegra Aura (Institut Néel; microscope designed particularly for MFM),
- NT-MDT Ntegra Prima (IPE, microscope contains magnetic parts, which corrupt the measurement),
- Veeco Autoprobe CP-R (IPE/CEITEC),
- Veeco Autoprobe CP-II (Masaryk University),
- Bruker Dimension Icon (IPE/CEITEC, microscope capable of TR-MFM imaging).

Classical two pass tapping/lift mode technique was used for the imaging. During the first pass amplitude change was tracked, whereas the phase shift was employed in the second pass at elevated (lift) height. If not stated otherwise, images were acquired with NT-MDT Ntegra Prima. Veeco Autoprobe CP-II at Masaryk university was used for comparison with Veeco Autoprobe CP-R at IPE, no significant difference were found, so only measurements from Veeco Autoprobe CP-R are presented.

5.2.2 Scanning Electron Microscopy and Energy Dispersive X-ray Spectroscopy

Scanning Electron Microscopy (SEM) with Energy-Dispersive X-ray spectroscopy (EDX) were used mainly for the characterisation of samples and fabricated tips. SEM probes the sample with a focused beam of electrons and detects both scattered and secondary-emitted electrons from the sample. If the energy of the beam is sufficient, i.e. at least few keV, x-rays are emitted from the sample atoms upon irradiation with the electron beam. These x-rays are probed with EDX and from the characteristic radiation we can determine the element composition of the sample. Two systems were used:

- Zeiss Ultra+ with Bruker QuanTax (Institut Néel),
- Tescan Lyra 3 XMH with Bruker QuanTax (IPE, 'default' microscope).

The SEM images of the probes and the tips were acquired with samples tilted by 55°. Note that the measured tip radii may deviated 1-3 nm from the reality and the tip radius of the bare AC240TS probes could not be determined, as the

resolution of the SEM is not good enough. We can only say that the tip radius is really below 10 nm, the value guaranteed by the supplier. The EDX analysis was performed with the primary electron beam energy of 15 keV for efficient excitation of K_α lines of iron group elements. Too high energy is undesired as the interaction volume is enlarged, problem of possible charging is more profound and no additional advantage is expected.

5.2.3 Magneto-Optical Kerr Effect

Magneto-Optical Kerr Effect (MOKE) relies on a change of polarization plane of a polarized light upon a reflection from a magnetic sample. Miranda apparatus at IPE enables measurement in a varying external magnetic field and thus acquisition of hysteresis loops, even in the case of thin films and microstructures. Focusable He-Ne laser is used as a light source and difference of two orthogonal light polarizations is employed for the data acquisition. The scheme and more information about the technique and the apparatus are to be found in bachelor's thesis by Lukáš Flajšman [109], who designed the instrument. The field of magneto-optics is described in a book by Štefan Višňovský [110]. Regrettably, a Hall probe for measurement of the applied field is no longer available. Therefore rather qualitative data are currently obtained. Nevertheless, in the frame of our work, this is sufficient for determination whether the deposited layer is soft/hard or even non-magnetic.

5.3 Simulations in OOMMF

Object Oriented MicroMagnetic Framework (OOMMF) is a public micromagnetic solver from NIST [15]. This finite difference code can solve the problem either by a numerical integration of the LLG equation (2.5) or by minimizing the energy functional. All simulations are performed at 0 K, although extension called *thetaevolve* extension can mimic a finite temperature. Basic micromagnetic interactions and energies may be specified and other added in the form of other extensions. 3D problems are solved in OOMMF eXtensible Solver (Oxs) with application Oxsii. Input is defined in the form of MIF 2.1 file, a Tk/Tcl script. Both scalar and vector outputs are available. The former one includes mainly particular energies, whereas the later pointwise magnetization or magnetic field values. Further information can be sought in the manual [15].

In our simulations of the magnetization in permalloy structures we take into account the magnetostatic energy and a standard 6-neighbour exchange energy. The magnetocrystalline anisotropy is added only in a computation involving cobalt tips,

whereas anisotropy is negligible for permalloy. The Zeeman energy was considered only when an external magnetic field was present. The cell size was $4\,\mathrm{nm}$ for standard and $2\,\mathrm{nm}$ for finer computation, which is lower than the dipolar exchange length of permalloy - $5\,\mathrm{nm}$. In case of Co, 2nm cell was employed. The damping parameter α was set to 0.5 (0.1 for nanowires) for a faster convergence as is common in micromagnetic simulations. Often even higher values are used. Other parameters are summarized in Table 5.2. The convergence criterion used in this work is reached when the maximal change in orientation of macrospins with respect to previous step is lower than a predefined value. In our case it is $0.1°/\mathrm{ns}$, in special cases $0.01°/\mathrm{ns}$. If not stated otherwise, the magnetic configuration is given in mid-plane of the sample - for example if the thickness is $40\,\mathrm{nm}$, then magnetization in $z = 20\,\mathrm{nm}$ is provided.

Tab. 5.2: Material parameters used in the simulations.

Parameter	Permalloy	Cobalt
Exchange stiffness A	$13 \cdot 10^{-12}\,\mathrm{J/m}$	$30 \cdot 10^{-12}\,\mathrm{J/m}$
Saturation magnetization M_s	$860\,\mathrm{kJ/m^3}$	$1400\,\mathrm{kJ/m^3}$
Uniaxial anisotropy constant K_u	0	$520\,\mathrm{kJ/m^3}$

Computation server Konrad (IPE) was used for carrying out the simulations. Note that in the computations of the magnetization and its divergence for comparison with MFM images, the structure is simulated as *it is*. That means that no possible interaction with the probe is taken into account. If the measured data corresponds to the simulation, no significant perturbation of the sample is present and we do really measure the map of the magnetic charges.

It is possible to model the whole MFM imaging and resulting MFM image as has been shown for example in [49]. But the realization itself is problematic. Usually the magnetic tip is approximated by dipole or even monopole. Even if we disregard questionable validity of the approximation, we do not know how strong is the effective dipole and where it should be positioned. However, some works dealing with determination of these values from the experiment exist [40]. Other approach relies on modelling the sample with the magnetic tip or at least its part. This way is not so common, because it often requires a lot of computation resources. If we adopt strategy from [49], we need to carry out 3 simulations with slightly different tip-sample distance to get numerically the derivatives of the total magnetic energy. But this has to be done for each pixel of our image! And for larger sample 1 simulation can take even few days...

In our way towards the simulation of the MFM imaging, a magnetic wire with a square cross-section serves as the probe. The edge is $12\,\mathrm{nm}$ and the length $100\,\mathrm{nm}$.

For sure this tip is far away from the tips used in our experiments, but still not so far from reality, because magnetic nanowires are sometimes employed as MFM probes [49]. We were forced to use 2 nm cell, because 4 nm provided spin-to-spin angle slightly higher than 30° and the energy was about 30 % higher than for the 2 nm cell.

6 RESULTS AND DISCUSSION

In this chapter we present the results of the probe preparation and MFM measurements of various NiFe soft magnetic samples including nanowires, antidot array and thin-film elements such as discs. Both commercial and our probes were employed in the imaging. The acquired images were compared with micromagnetic simulations.

6.1 Instrumentation - improvements

Aside from maintaining the Veeco Autoprobe CP-R microscope and help with the maintenance of the deposition apparatus (cryo-pump, thickness meter), several improvements have been made. The most important of them are storage of magnetic probes and samples in low humidity environment and a magnetic-shielded holder for the NT-MDT Ntega Prima microscope which enables reasonable MFM measurement on this instrument.

6.1.1 Storage of samples and probes

Magnetic samples and the prepared MFM probes are being stored under low vacuum in a vacuum dessicator with silicagel dessicant to protect them from ageing - mainly the oxidation. This prolongs the lifetime of both the samples and the probes. Commercial MFM probes are stored in closed containers with desiccants for the same reason. In principle magnetic targets for ion beam sputtering may be stored under under vacuum in a larger dessicator as well. However, this is not used so far, because the oxide layer and impurities are removed by ion sputtering before the deposition.

6.1.2 Veeco Autoprobe CP-R

Slight improvement of the microscope performance was reached after the scanner calibration. The cantilever AC240TS, the base for our MFM probes, was added to the database of probes and rough calibration of oscillation amplitude was performed. However, precise calibration would have to be done for each cantilever. A new feature was added - phase tracking, possibility of phase shift when tuning the resonant frequency of the cantilever. Unfortunately it has not been confirmed if this feature is fully supported by the current hardware, because software for a newer version of the microscope is used. During experiments with this new feature, the cores of magnetic vortices in permalloy discs were measured with our probe bearing NiFe/AlO$_x$ coating. The results are displayed in Figures 6.1 and 6.2. Regrettably, such good results were measured only during one session and not repeated ever since,

despite considerable effort. Aside from the measured data, the figures involves corresponding micromagnetic simulation, which are in good agreement both with the measurement and theory.
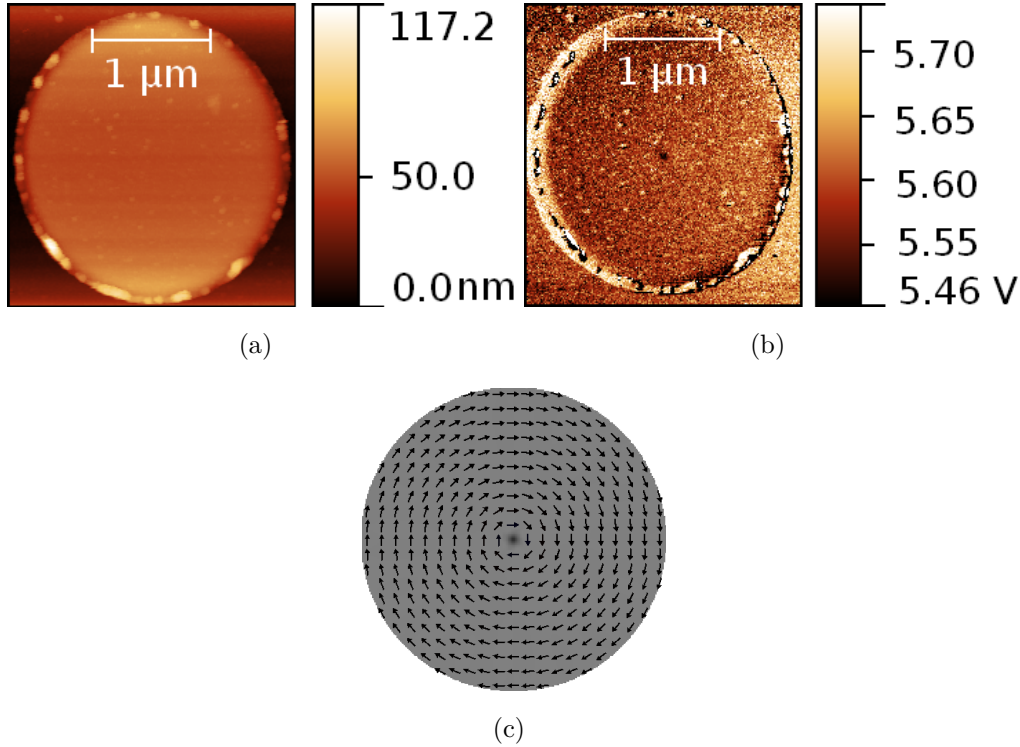

(a)

(b)

(c)

Fig. 6.1: Permalloy disc (thickness 45 nm, diameter 2 µm) imaged by our K7 NiFe/Al probe on the Veeco CP-R microscope and comparison with the micromagnetic simulation. (a) topography, (b) MFM image. Aside from the core in the centre (black dot), MFM image contains a lot of topographical impurities due to low lift height of 8 nm, which was necessary to get reasonable signal. (c) corresponding micromagnetic simulation (cell size 2 nm). Two images were superimposed (magnetization and its divergence) fort the sake of simplicity. Black arrow indicate in-plane circulation of the magnetization. Gray-scale background is a map of magnetic charges which is close to the signal provided by MFM. Black dot in the centre shows the core of the vortex with out-of-plane magnetization.

6.1.3   NT-MDT Ntegra Prima

For quite a long time it was believed (until recently), at the institute, that this microscope is not capable of MFM imaging. This assumption was supported by rather disappointing measurements. There were two main reasons. First, setting the appropriate parameters for the MFM imaging can be rather tricky. Secondly, the microscope contains magnetic parts that influence the measurement. In addition,
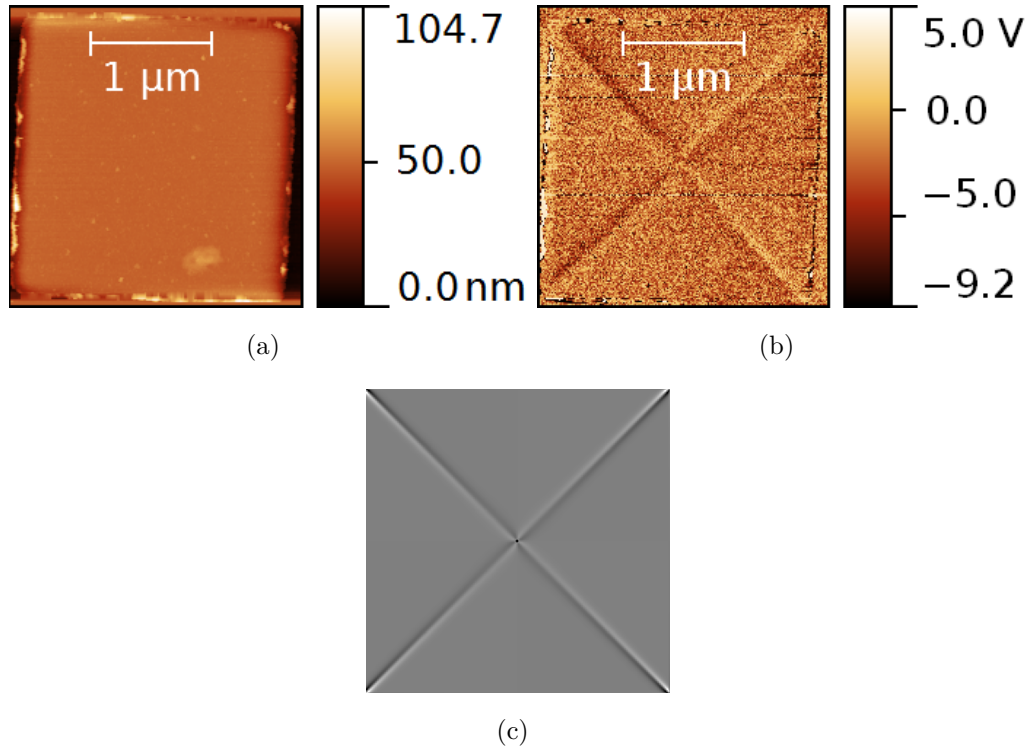
(a)

(b)

(c)

Fig. 6.2: Permalloy diesquare (thickness 45 nm, edge 2 µm) imaged by our K7 NiFe/Al probe on the Veeco CP-R microscope at lift height 10 nm and corresponding simulation of the magnetic state. (a) topography, (b) MFM image. Dark and bright contrast near the square diagonals correspond to the domain walls and an expert eye can see also the dark dot in the centre which shows the core polarity. (c) simulation of magnetic charges in the diesquare. Note that the core is really tiny. The simulation with 2 nm cell shows that its size is 12-16 nm for above mentioned geometry. In the article by Fisher et al. [111] the size was 18 nm, but for larger thickness - 50 nm and larger computation cell size of 4 nm. The core looks larger in MFM due to long-range interactions. The magnetization in such element has been already shown in Figure 2.7.

even the sample holders were magnetic! In a such case, both the tip and the sample magnetization can be distorted.

The magnetic field at the sample's position corresponded to up to few tens of mT at some points according to a measurement with Phywe Teslameter. Such field is sufficient for saturation of soft magnets as well as for switching of some MFM probes. Influence of the magnetic parts on the soft permalloy nanostructures is illustrated in Figure 6.3. All structures, no matter what shape and dimension looked like dipoles, almost homogeneously magnetized elements in the external field of the magnetic parts. Even though the sample holder can be replaced with a non-magnetic one, the most problematic magnet is incorporated into the scanner. For comparison, permalloy diesquare from Figure 6.3 was subject to simulation in external magnetic-field, which lies along the square diagonal and its magnitude corresponds to 50 mT. The result is illustrated in Figure 6.4. Although both the field magnitude and direction may slightly differ, the simulated map of magnetic charges agree with the measured MFM images.

When trying to deal with this issue, we put a piece of Fe plate as a weak shielding on the magnetic sample holder and tried to image a hard disc drive (HDD) and we succeed - see Figure 6.5. We moved on for permalloy nanostructures as demonstrated in Figure 6.6. There is great deal of improvement, nearly the Landau pattern is visible in the squares, with respect to the state depicted in Figure 6.3, but still some external influence is present. The teslameter showed something like few mT.

Finally, a special sample holder with 1mm thick Mu-metal plate, material which is used in industry for magnetic shielding, was assembled (captured in Figure 6.7). The design is rather crude, but sufficient. Geometry of the holder is limited by the head of the microscope as is illustrated in Figure 6.8. All MFM images from Ntegra Prima in the following part of this work were acquired with this shielded sample holder.

6.2 Measurement with commercial probes

Because of the long term shut down of the deposition apparatus, the preparation of our probes was significantly slowed down and for some time only commercial probes were available for the measurement. Below we present results obtained with the probes from 3 manufacturers: Asylum, Bruker and Nanosensors. The parameters of the commercial probes have already been described in section 4.3 and particularly in Table 4.1. According to the EDX inspection, the whole tip is covered with magnetic material in all cases of commercial probes.
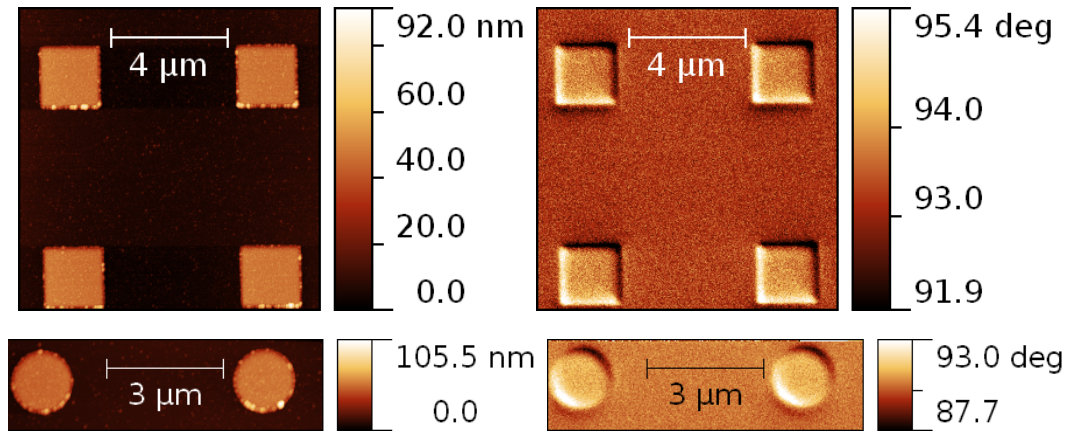
Fig. 6.3: Permalloy thin film elements (thickness 40 nm) imaged by the Ntegra Prima microscope and slightly damaged $AC240TS/CoCr[10\,nm]/Pt[1\,nm]/AlO_x[3\,nm]$ probe from Institut Néel. Left: topography. Right: MFM. Note that all elements seem to be saturated in one direction (diagonal of the squares) and dipolar contrast is seen - surface charges. This is caused by the magnetic parts of the microscope.
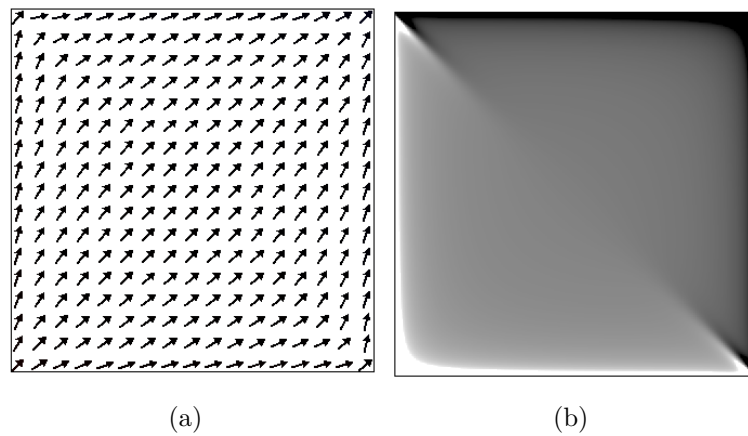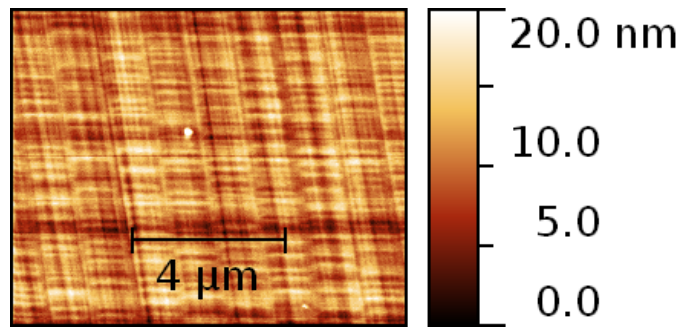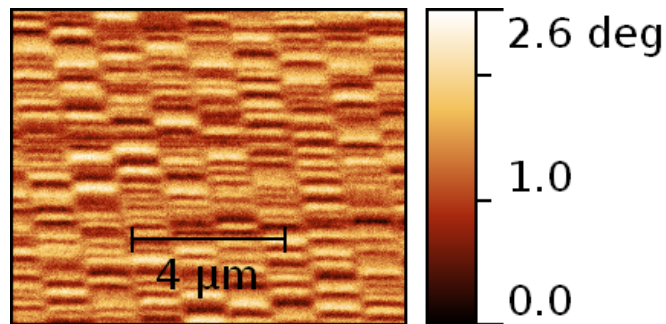

(a)   (b)

Fig. 6.4: Simulation of the permalloy diesquare from Figure 6.3 in external field applied along the square diagonal. The field magnitude corresponds to 50 mT. (a) magnetization, (b) magnetic charges. The simulated charges match the MFM observation from Figure 6.3.

(a)

(b)

Fig. 6.5: Hard disc drive with in-plane (longitudinal) magnetization imaged by the Nte-gra Prima microscope and slightly damaged $AC240TS/CoCr[10\,nm]/Pt[1\,nm]/AlO_x[3\,nm]$ probe from Institut Néel. (a) first pass - 'topography'. (b) second pass - MFM image. Note that even in the first pass the magnetic contributions is significant and bits separated by dark and bright lines can be distinguished. This is the reason why stiffer cantilevers are used for the imaging of permanent magnets and magnetic recording media to suppress the magnetic signal during the topography acquisition. The significant magnetic signal in the first pass leads to a slight deformation of the 'magnetic' image acquired in the second pass. The sample is rather flat and no topographical feature can be seen in the right image - neither nearly horizontal lines, nor an impurity near the centre of the image. This is ensured by the large lift height, 60 nm, in the second pass.
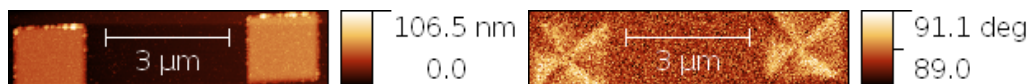

Fig. 6.6: Permalloy squares (thickness 40 nm) imaged by the Ntegra Prima microscope with slightly damaged $AC240TS/CoCr[10\,nm]/Pt[1\,nm]/AlO_x[3\,nm]$ probe from Institut Néel and rather simple shielded sample holder. Left: topography. Right: MFM. Although not ideal, some pattern which resembles the Landau one, magnetic vortex in a square, is present.

Fig. 6.7: Shielded sample holder for the Ntegra Prima microscope which consists of non-magnetic tubular ceramics with Al foil inside and 1mm thick Mu-metal plate and sticking tape for mounting the sample. The height of the holder is approximately 1 cm.
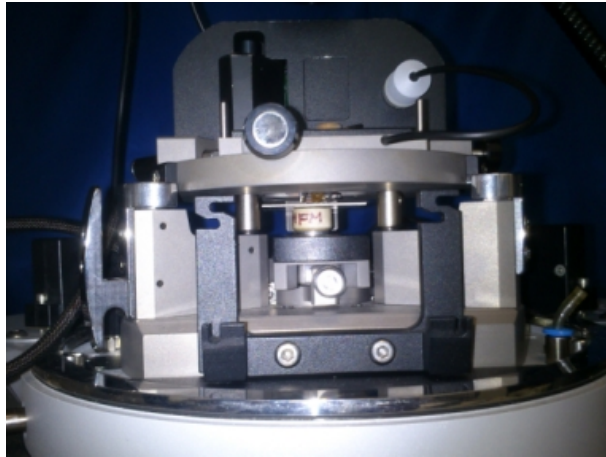

Fig. 6.8: Ntegra Prima microscope with shielded sample holder, it is obvious that there is not so much space left . . .

6.2.1 Asylum ASYMFMLM

The Asylum LM tips turned out to be a great disappointment - nothing was measured for 4 out of 5 delivered probes (the last one was left for further inspection). Observations were performed on two different microscopes - Veeco Autoprobe CP-R and NT-MDT Ntegra Prima. Various imaging parameters (oscillation amplitude, set point, lift hight) and samples (NiFe nanostructures, HDD) were tried without any magnetic contrast. The whole probe, including the reflective coating) is covered with 15 nm CoCr magnetic layer according to the suppliers specifications. The reflective coating provides a very low laser signal (sum intensity of laser beam reflected from the probe). For the Veeco microscope this signal is close to the minimum which is required for the correct microscope operation. On average, the laser signal from Nanosensors probes (reflective coating 30 nm of Al) is about 150 % of Asylum LM. Our home-coated probes based on AC240TS (reflective coating 100 nm Al) have laser signal 160-180 % with respect to Asylum LM.

SEM inspection revealed that the probes are completely oxidized and corrupted as demonstrated in Figure 6.9. EDX analysis found following elements on the tip: C (contamination), O (quite prominent peak, oxidized layers), Si (base cantilever material), Co and Cr ('magnetic' layer).
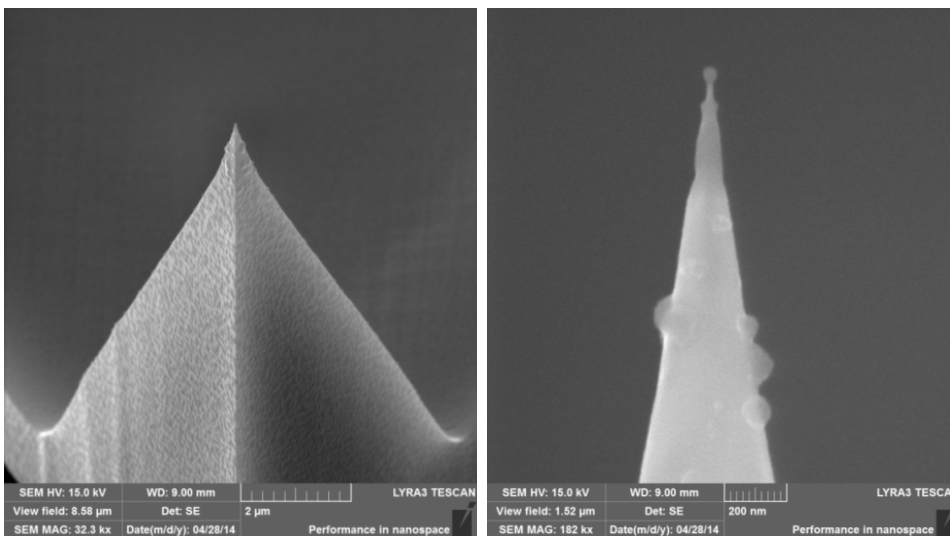

Fig. 6.9: SEM images of oxidized and corrupted ASYMFMLM tip. Left: whole tip, front view. Right: detail of the tip apex.

6.2.2 Bruker MESP

The MESP probes belong to the standard ones, both the composition (CoCr) and the coating thickness (respectively tip radius) corresponds to the parameters specified

by the manufacturer. A typical MESP tip is shown in Figure 6.10. Magnetic vortices and their cores, both in permalloy discs and diesquares (see Figure 6.11), have been measured, but only on the NT-MDT Ntegra Prima microscope. The tips are not well suited for the imaging of soft permalloy structures. Although this may not be so obvious for magnetic vortices, it is prominent in case of a permalloy rectangle as illustrated in Figure 6.12. C or S-state is expected in this case, but the result is biased by the tip. And the perturbation seems to be irreversible. Only distorted images of Landau patterns without vortex cores were measured on the Veeco microscopes (CP-R and CP-II) and on the Bruker Dimension Icon. The Bruker microscope should have even better sensitivity than Ntegra Prima, therefore it seems that the problem is in the selection of the appropriate imaging parameters.
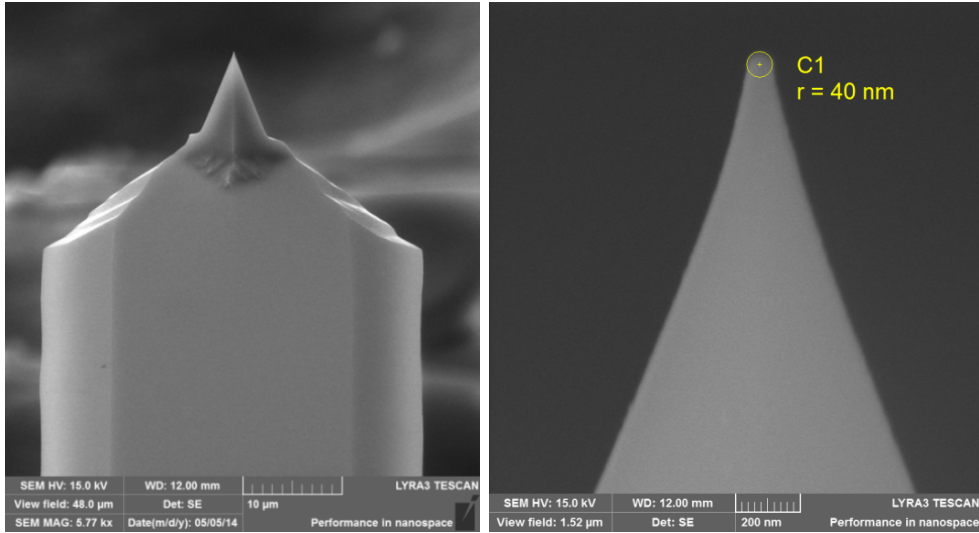

Fig. 6.10: SEM images of a Bruker MESP probe. Left: cantilever with a tip. Right: detail of the tip apex. The tip radius - 40 nm - lies in the guaranteed range $< 50\,nm$.

6.2.3 Nanosensors

Three types of probes from Nanosensors were employed for the measurement - standard, low moment (LM) and supersharp tips with even lower magnetic moment.

PPP-MFMR (standard moment)

Standard MFM probes from Nanosensors (Figure 6.13) very resemble Bruker MESP probes (depicted in Figure 6.10), the etching process for the tip fabrication seems to be similar and both probes have the same tip radius near 40 nm. Also the imaging performance seems to be close to the MESP probes which can be seen in Figure 6.16(b).
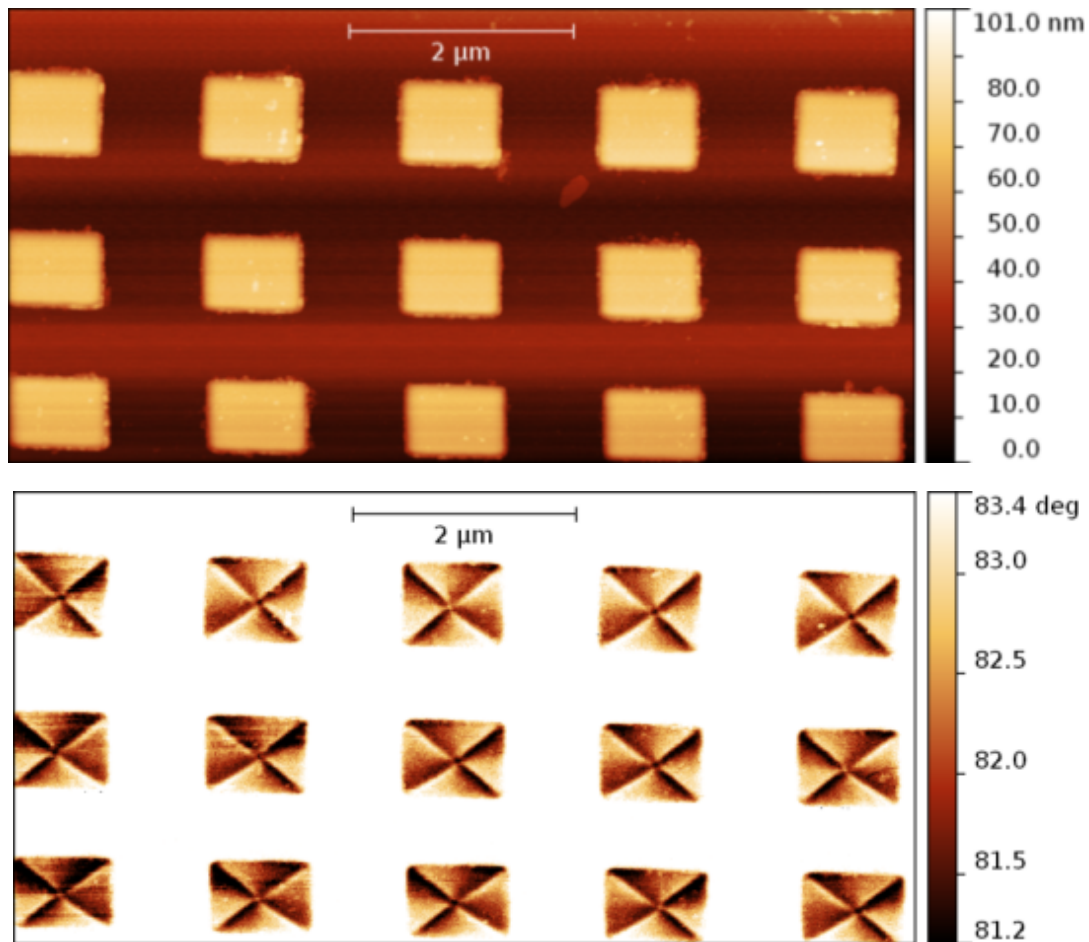
Fig. 6.11: An array of permalloy diesquares (thickness 50 nm). Top: topography. Bottom: MFM. Bruker MESP probe, lift height 20 nm. Few topographical features, impurities, can be seen in the MFM image due not so large separation (lift height). All four possible states of a magnetic vortex in a diesquare can be found in the image. The core polarities (up, down) are represented by bright and dark dots in the centre of the squares. The in-plane circulation (clockwise, counter-clockwise) can be deduced from the change of a contrast near the diagonals of the squares.
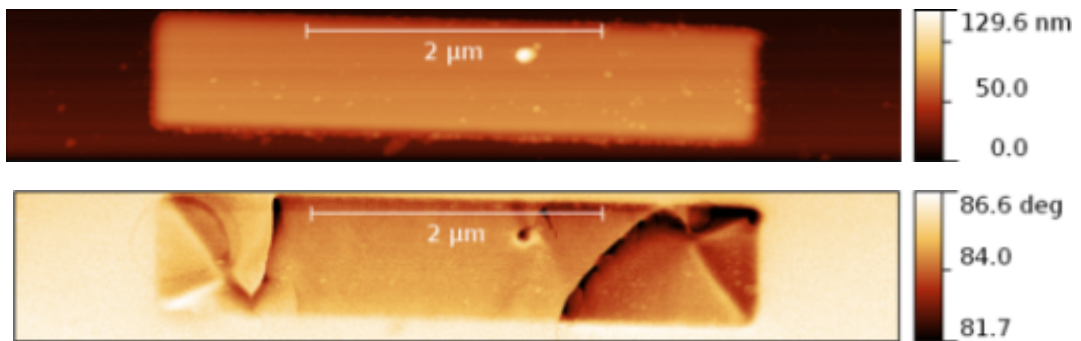
Fig. 6.12: Perturbation in a permalloy rectangle induced by the Bruker MESP probe and lift height 20 nm. Top: topography. Bottom: MFM. The pattern deviates from expected near single domain S or C-state.

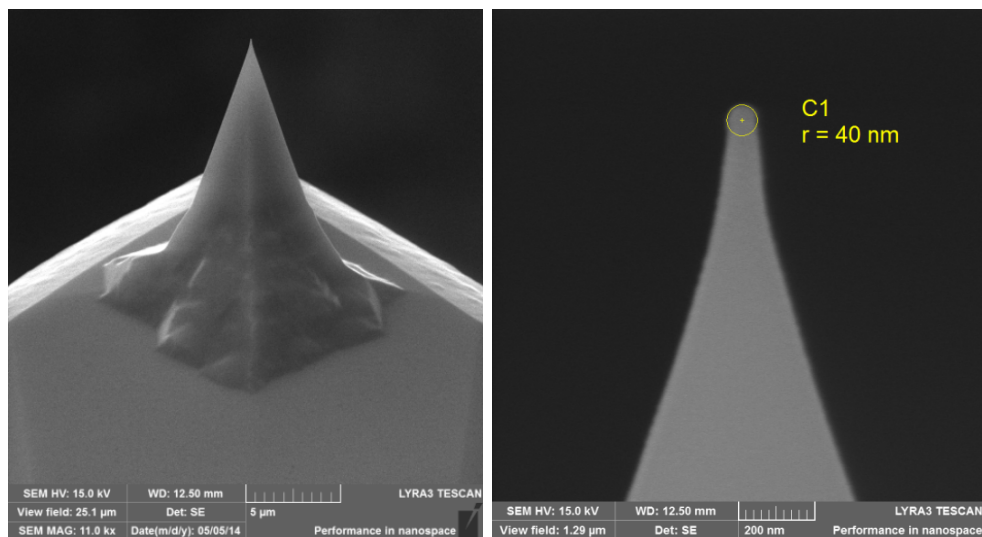Fig. 6.13: SEM images of a Nanosensors standard probe. Left: whole tip on protruding from the lever. Right: detail of the tip apex.

PPP-LM-MFMR (low moment)

The LM tip has the tip radius slightly higher than 20 nm as can be seen in Figure 6.14. According to the catalogue, this tip should be suitable for imaging of soft magnets. However, this is not completely true. It turned out that commercial low moment is not low enough. Several tip induced perturbations have been observed, example of rather nice one is magnetization switching during the measurement of a small permalloy rectangle, which is depicted in Figure 6.17. Unambiguously, the resolution of the LM probe is better than that of the standard tips. Further, no problem has been encountered during the observation of magnetic vortices. Example of two vortices with opposite core polarities is given in Figure 6.15. Note that the discs as well as other permalloy structures in our images are darker than the background. In our notation it means overall attractive force between the tip and the sample. This leads also to the fact that the 'bright' cores are less intensive as has been already discussed in [49]. A very nice observation of a disc array hosting magnetic vortices with different polarities is depicted in Figure 6.16(a).
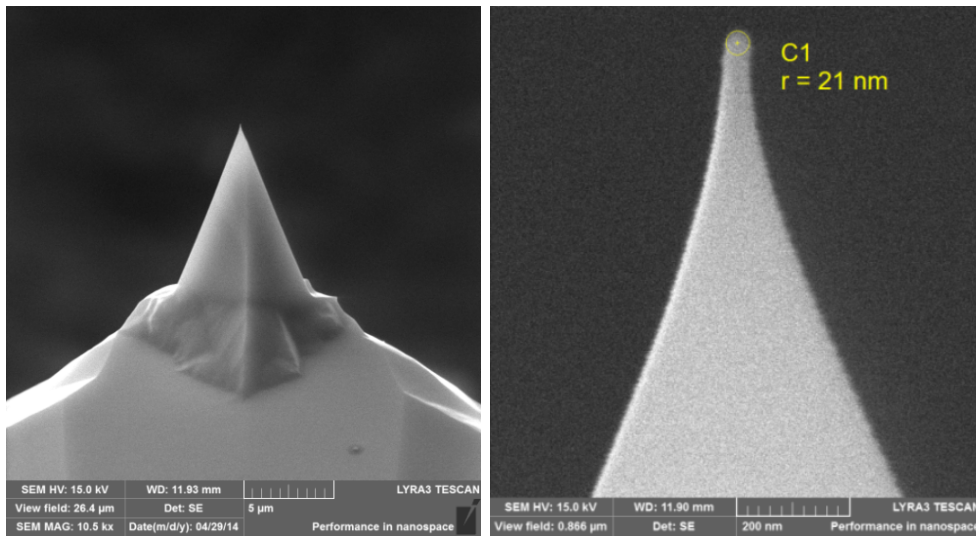
Fig. 6.14: SEM images of a Nanosensors LM probe. Left: whole tip on protruding from the lever. Right: detail of the tip apex.

SSS-MFMR (supersharp)

The supersharp tip provides the best resolution in topography and a good MFM resolution as well. Further no perturbations have been observed during the measurement with the probe. Figure 6.18 shows similar rectangular permalloy element which was switched by the LM probe. On the other hand, the MFM signal is
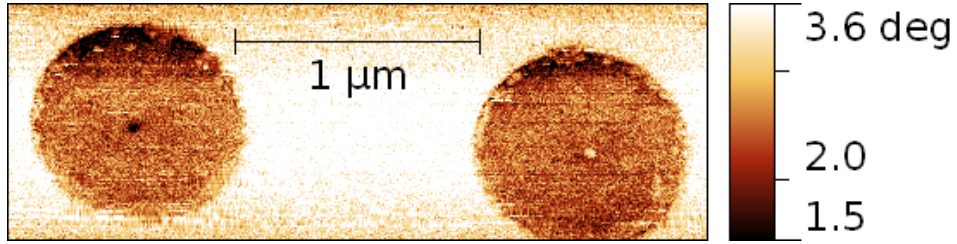
Fig. 6.15: Magnetic vortices in permalloy discs with the opposite polarities indicated by a dark and bright dot in the disc centre. LM probe, lift 15 nm.

quite low and handling of these probes is rather difficult. They are very easily destroyed, require a very careful approach to the sample and slow scans should be used ($< 1\,\mu$m/s recommended). Such a slow scan is very problematic if the sample is drifting and/or when we would like to scan larger areas (several micrometers). Like other Nanosensors tips (as well as in general), the probes are said to be very sensitive to static electricity and even small 'discharge' may deteriorate/destroy the tip. Last but not least, one probe cost even more than 100 €. That is why only two probes were obtained as free samples. These probes are not economically viable in our case.
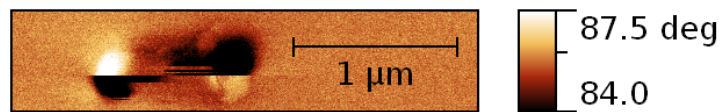
Fig. 6.17: Magnetization switching of a permalloy rectangle induced by the LM probe during the scanning. The switching is indicated by the abrupt change in contrast. After the event, the contrast at the ends is reversed. How the map of magnetic charges looks like without the perturbation is demonstrated in Figure 6.18 where the same type of element was imaged by the supersharp probe.
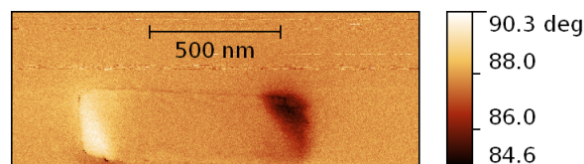
Fig. 6.18: Near single domain S-state in a permalloy rectangle imaged by the supersharp probe at lift height of 15 nm. Bright and dark parts indicate opposite magnetic charges. The same type of element was observed in Figure 6.17 with the LM probe, which caused magnetization reversal in the element.
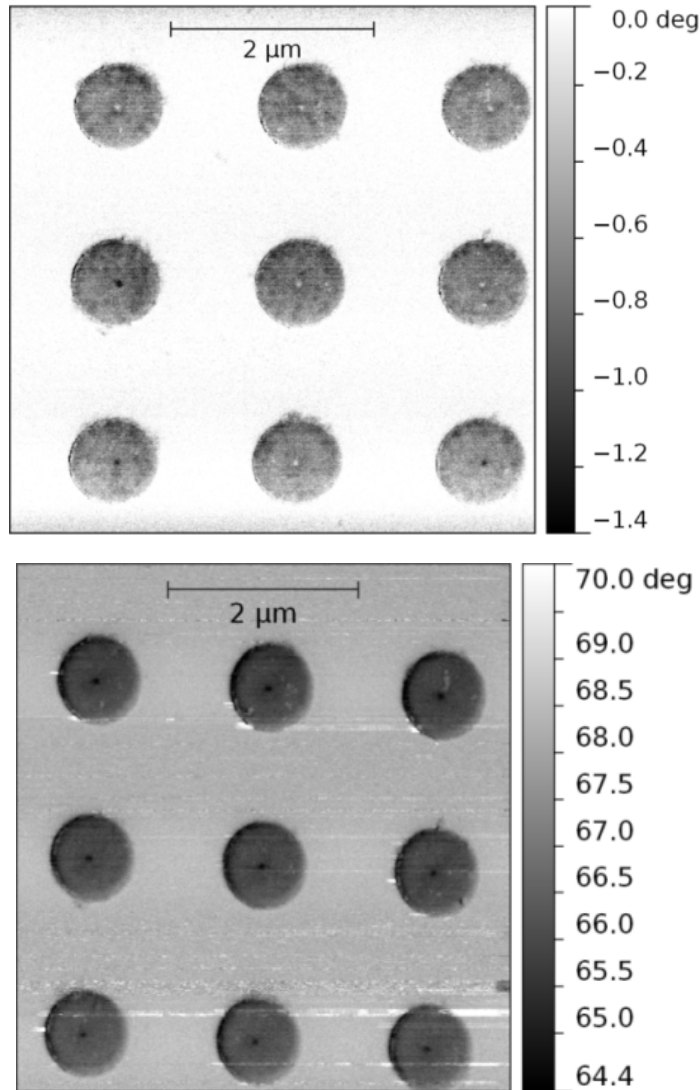
Fig. 6.16: Vortex core polarity switching in a NiFe disc array. (a) MFM image of the array after an out-of-plane demagnetization taken with Nanosensors LM probe. Both core polarities are randomly present in the array. (b) The same array (check the 'j' topographical impurity on the top-right disc) after saturation in out-of-plane external field. Only one core polarity imposed the previously applied external field can be observed. The same polarity was found for other 15 elements in a larger array. Imaged with Nanosensors standard probe.

6.3 Magnetic nanowires

Magnetic nanowires are potential candidates for novel spintronic applications such as the magnetic racetrack memory based on domain walls propagating in nanowires [28]. Here we provide results of the nanowire fabrication and observation of domain walls supported by micromagnetic simulations.

The template used for the NiFe nanowires (NWs) electrodeposition and prepared nanowires are captured in Figure 6.19 . The inspection by AFM and SEM shows that the nanowires are more than 10 μm long with diameter around 50 nm. According to the EDX measurements the chemical composition of prepared NiFe nanowires is homogeneous and despite some inhomogeneities at the scale of tens of nanometers, both elements (Ni, Fe) cover homogeneously the whole area of the nanowires. This is not the case of nanowires fabricated by the common electrodeposition; authors usually give only an overall composition of their samples but do not provide information about element distribution that is crucial for novel magnetic memories - unwanted DW pinning may slow down or completely corrupt such a device. Other effect like deviation from ideal shape and roughness will not be addressed here - they are related mainly to the quality of the template used for the nanowire preparation.

(a)   (b)
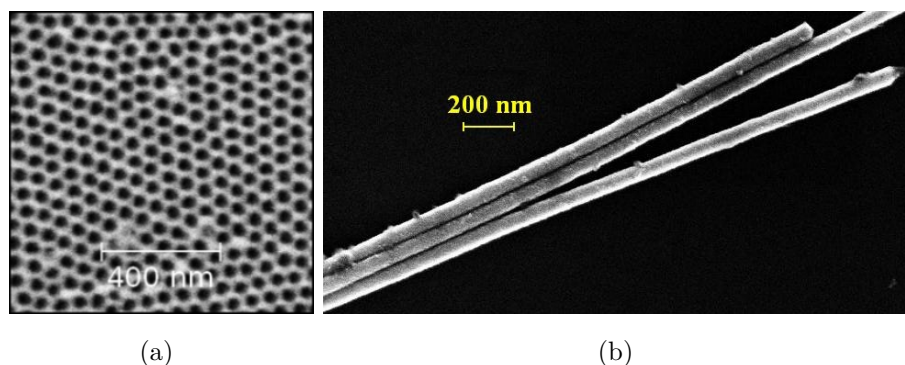
Fig. 6.19: (a) nanoporous alumina template used for NiFe nanowire electrodeposition and fabrication of an antidot array. (b) prepared NiFe nanowires dispersed on a Si substrate. SEM Zeiss Ultra+.

In the ground state of a straight NiFe nanowire the magnetization lies along the nanowire axis and opposite magnetic charges are present at both ends of the nanowire. This is illustrated in Figure 6.20.

Even though it is possible to nucleate the DWs in a straight nanowire by demagnetizing the sample in a direction transverse to the wire axis, we have adopted a more robust strategy. Part of the nanowires was bent by a directional air blowing of the IPA solution with NWs. The bent part acts as a geometrical trapping centre

Fig. 6.20: Simulation of a straight cylindrical permalloy nanowire with diameter 40 nm, length 4 μm, cell size 4 nm and damping parameter 0.1. Top: magnetization. Bottom: divergence of magnetization - map 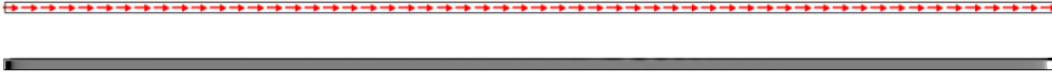of volume magnetic charges. Note the opposite charges at the ends. Cross-section along the nanowire is shown in the both cases.

for the DW when subject to an external field. Prior to the MFM observation, patterned Si substrate with dispersed nanowires was magnetized with an electromagnet by in-plane field $\mu_0 H_{ext} \approx 1\,T$ perpendicular (transverse) to the nanowire curvature [illustrated in Figure 6.22(a)].

MFM observations of soft magnetic nanowires, especially homogeneous ones, are challenging. The use of commercial probes even these with low magnetic moment leads to an unwanted domain wall distortion or displacement - depicted in Figure 6.21. Extremely low moment AC240TS probes with CoCr[3 nm]/Pt[1 nm]/-AlOx[5 nm] multilayer (at Institut Néel) were used in order to overcome the undesired DW displacement.
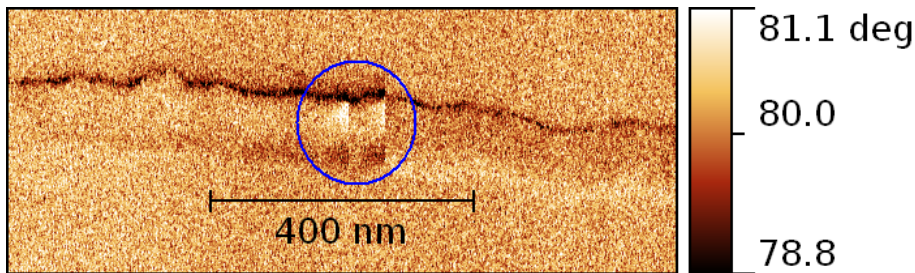
Fig. 6.21: MFM image of the DW displaced by the magnetic probe. Fast scan was performed in vertical direction. Apart from nanowire contour (signal from topography due to low lift height) phase contrast with abrupt change can be seen - DW was moved in two steps, first only few tens of nanometres, than completely away from scanned area. Ntegra Aura microcope.

Magnetic domain wall in the bent NiFe nanowire was nucleated after withdrawal of the sample from the external field perpendicular to the nanowire curvature as confirmed by MFM observation in Figure 6.22(c) and rather crude simulation (Figure 6.23).

In order to mimic the experiment, the bent nanowire was simulated. Length of the simulated wire is smaller than in experiment to save computational time. This is not a problem provided that the length is much larger than diameter. For the sake of simplicity (easier modelling) a wire with square cross-section (edge about 50nm)

(a)

(b)

(c)
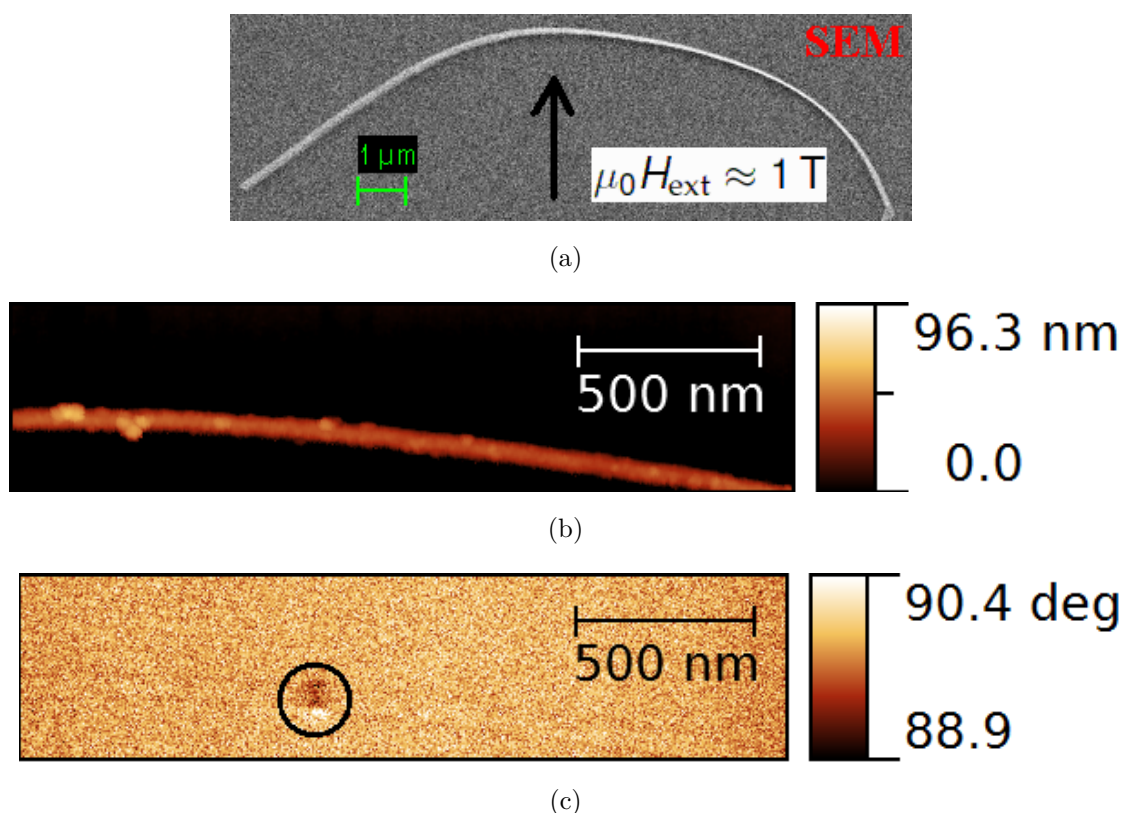
Fig. 6.22: *Electron and force microscopies observation of a bent NiFe nanowire with diameter $\approx 50\,nm$. (a) Scanning electron micrograph (crop from bigger image) with black arrow indicating direction of external field applied before imaging (DW nucleation after relaxation). (b) AFM topography of a part of the curved nanowire. Lateral distance (diameter) is overestimated in AFM, especially with rather blunt MFM tip, the tip radius is slightly less than $20\,nm$ (c) Corresponding MFM phase image (lift mode), black-circled phase contrast corresponds to the domain wall, nanowire contour may be seen as well (topography contribution). Zeiss Ultra+ and Ntegra Aura microscopes were used for the imaging.*

Fig. 6.23: *Domain wall in the bent permalloy nanowire, simulation of $div\vec{M}$ (magnetic charges) is shown in gray-scale for better comparison with MFM measurement, cell size $4\,nm$, damping 0.1. 'Black' part near the centre corresponds to the DW, other weaker contrast might be seen when diameter slightly changes and at the right end of the wire. Only crop of the nanowire with the DW is displayed.*

was simulated. Processed AFM image [from Figure 6.22(b)] served as an input geometry. Processing involved contrast enhancement, crop and rescaling - lateral distance is overestimated (underestimated in case of holes) in AFM, especially with rather blunt MFM tip. Nanowire was put in the strong field as in the experiment [Figure 6.22(a)] and then let to relax without any field. As depicted in Figure 6.23, finally only one DW remained in the curved part of the wire. Detailed view on magnetization vector orientation in the vicinity of the DW is given in Figure 6.24. According to this simulation two parts with opposite magnetization are separated by BPW with Bloch point with zero magnetization in the centre [Figure 6.24(b)]. TW should become energetically-viable for nanowire edge (square cross-section) smaller than 35-40 nm [25]. However, it is necessary to mention, that in the case of a nanowire with square cross-section, energy of TW and BPW differs only slightly for the edge of 50 nm and even TW can be present in nanowire with diameter/edge of 50 nm depending on the magnetic history of the sample. Example of simulated TWs in a straight cylindrical nanowire 40 nm in diameter is illustrated in Figure 6.25.
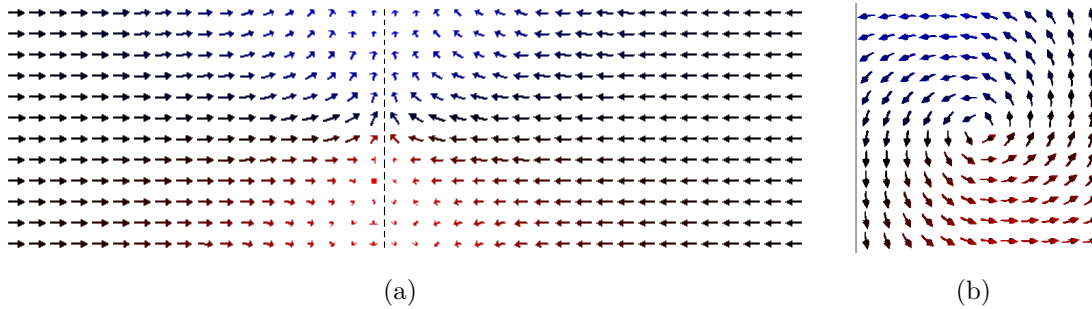

(a) (b)

Fig. 6.24: Bloch point domain wall in bent 50 nm thick nanowire for 4 nm cell size. (a) Magnetization lies along nanowire axis, but two parts with antiparallel orientation might be distinguished, separated by BPW. Blue and red arrows denote out-of-plane magnetization in parts of DW. Where these two meet (in the centre of the wire), Bloch point with zero magnetization sits. (b) cross-section of the BPW with Bloch point in the centre. Note that the image is not symmetric along the nanowire axis. This might be attributed to the fact, that the cross-section is not taken exactly in the centre of the DW (cell size restriction) and the nanowire diameter varies slightly in this region. Although this magnetization configuration may somewhat resemble vortices found in discs and diesquares, BPW posses no core with out of plane magnetization, magnetization vanishes in the centre instead.

It has been shown that even such a small structure like the DW in a nanowire [see Figure 6.22(c)] can be observed by MFM, unfortunately even the ultimate resolution of this technique cannot depict internal structure of DW in a nanowire - i.e. transverse and Bloch point walls cannot be distinguished by this technique so far. DW was found in the bent part of the nanowire as expected and confirmed by micro-
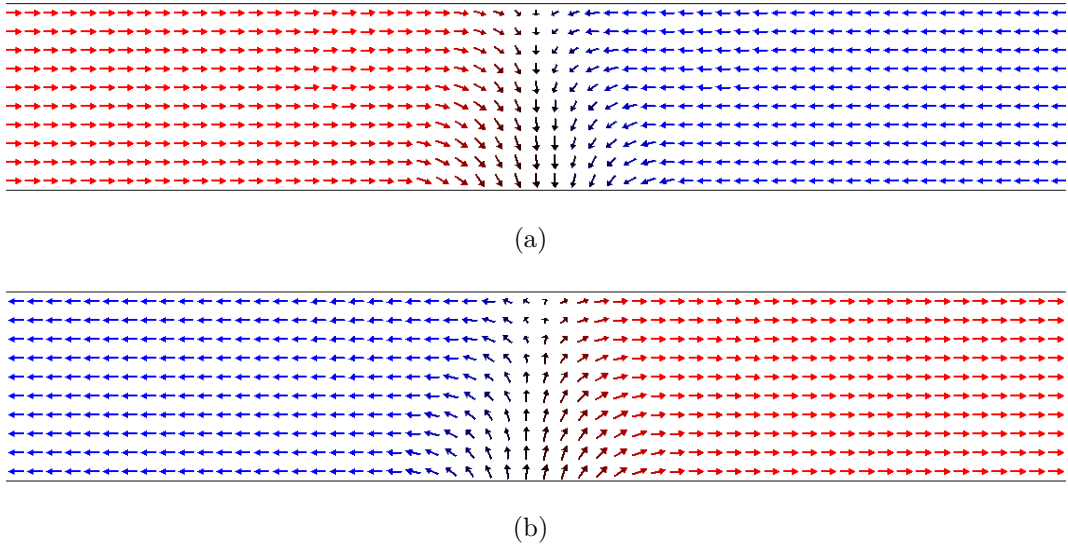
(a)

(b)

Fig. 6.25: Simulation of transverse walls in a straight cylindrical permalloy nanowire with diameter 40 nm, length 4 μm, cell size 4 nm and damping parameter 0.1. (a) head-to-head and (b) tail-to-tail transverse wall. Note, that here blue and red indicate opposite magnetization along the nanowire axis and black arrows show transverse magnetization.

magnetic simulation (Figure 6.23). The position is not exactly the same due to the model used for simulation - roughness and other defects were not taken into account. From micromagnetic simulation (Figure 6.24) we conclude that DW type might be BPW which is for this thickness (edge, 50 nm) in agreement with [25]. In further and finer simulations a finite element solver could provide better performance and better approximation of curved and bent geometries.

6.4 NiFe antidot array

An array of NiFe antidots was fabricated by the deposition of 20 nm NiFe on the nanoporous alumina template with pore diameter around 60 nm. Optimal thickness of the layer is crucial for the antidot array. Too thick layer will result in a continuous layer and too thin layer will not provide enough signal for the MFM observation. Measurement performed on the array is summarized in Figure 6.26. From the topography image, it is obvious that the array have many defects which are inherited from the template. However some contrast in the MFM image can be seen at lift height of 40 nm, when the topography contribution should be low. Many dark areas correspond to the holes and defects in topography, but there is still some contrast that should be of a magnetic origin - especially the bright parts in places, where holes are present in the topography. Still the results are quite disappointing

as we expect a map of magnetic charges that resembles the simulation shown in Figure 6.27(a).

For the modelling, a processed SEM image served as a template. Magnetization lies in-plane and closes around the holes as shown in Figure 6.27(b).

(a) (b)
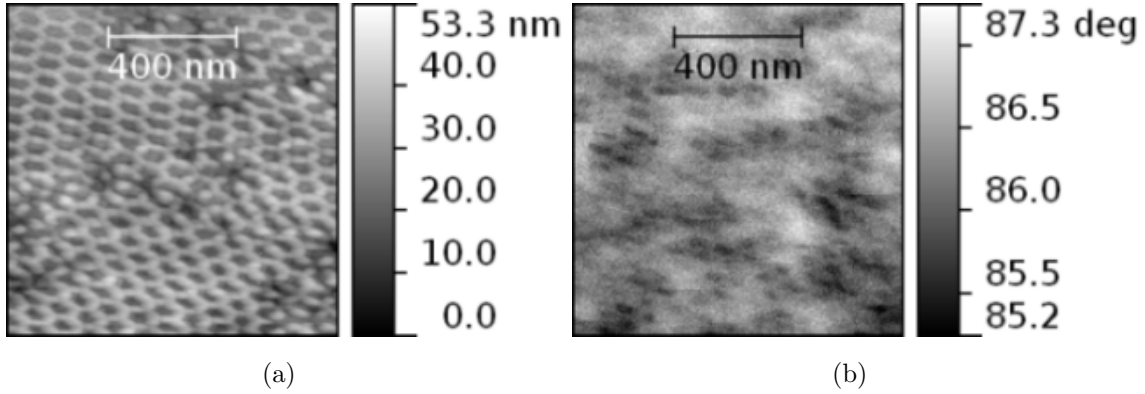
Fig. 6.26: Array on NiFe antidots on the nanoporous alumina template. (a) topography, (b) MFM, Nanosensors LM tip and 40 nm lift height.

(a) (b)
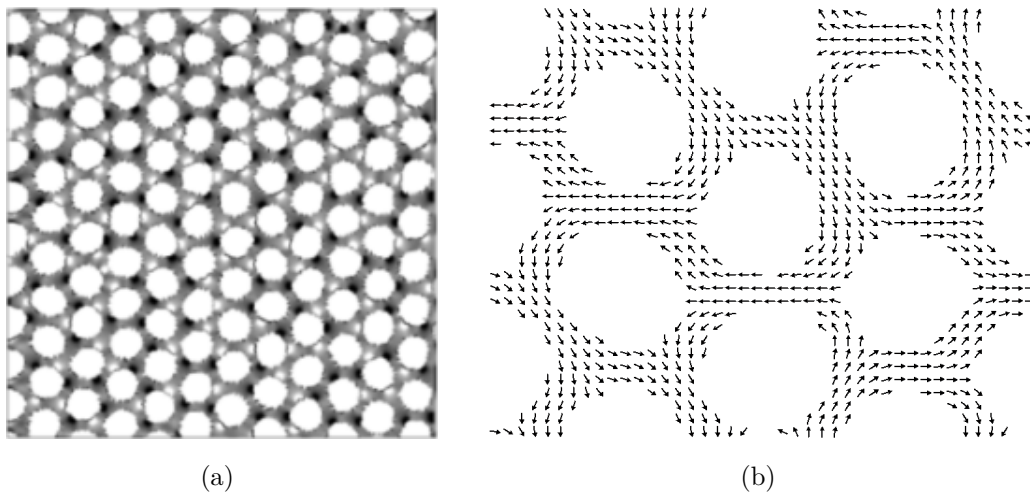
Fig. 6.27: (a) map of magnetic charges in the 20 nm thick antidot array, field of view is 1 μm. (b) magnetization in the NiFe antidot array closes around the holes. Magnetization near the part where two neighbouring hexagonal cell meet, follows rule two-in and one-out or vice versa. Situation when all three neighbouring magnetization vectors point in, or out is unfavourable. Crop of a larger simulated image.

Next, we tried to deposit thicker layer - 40 nm of NiFe, but in this case the pores were almost covered. Further experiments were not possible due to the lack of suitable templates.

More promising results should be obtainable with the template with less defects, smaller pore diameter, higher interpore distance and thicker NiFe layer, when the

magnetic volume is higher, but almost the same geometry is kept. For the current sample the achievable resolution might not be good enough. The pores themselves can be problematic as the abrupt changes in topography lead to the higher topography contribution in the lift mode. This might be overcome by sealing the pores with a resin. Eventually the template can be dissolved and the array transferred to another substrate. Last but not least, if the NiFe deposition is not perpendicular to the sample surface, magnetic material covers the walls of the pores near the surface and may have some influence on the resulting magnetic configuration.

6.5 Preparation of MFM probes

Similarly to commercial probes, all tip sides are covered with the magnetic layer (probed with EDX). However there is preferential deposition on the back side of the tip due to the tip geometry. It turned out that the thickness of the coating on the tip is much lower than on a flat substrate. Thus sometimes 60 nm layer on a flat substrate corresponds to 15-20 nm layer on the tip. The results of covering the AC240TS tips with NiFe, Co and CoCr coatings are presented below. Note that long term shut-down of the deposition apparatus forestalled the more systematic preparation of the probes and optimization of the process.

6.5.1 Tips with NiFe coating

First several probes deposited with Marek Vaňatka suffered from the low MFM signal. The NiFe thickness was 10-30 nm on a flat substrate and further 4 nm of Al was added as a cover layer. The probes were continuously rotated in-plane of the sample holder during the deposition. The probe K7 with 30 nm NiFe, veteran of many observations, gave very good results - the vortex cores were measured with this probe on the Veeco CP-R microscope. The resulting images are displayed in Figures 6.1 and 6.2.

Next several probes with a similar thickness of the NiFe coating exhibited no or very weak MFM signal. The deposition without rotation at slightly different deposition angles provided no improvement.

Recently, probes with a higher thickness have been deposited - 35 and 40 nm (on a flat substrate). Especially 40 nm of NiFe provided satisfactory results. The apex radius near 22 nm (12-15 nm of NiFe on the tip) is shown in Figure 6.28 and examples of observations with these tips in Figure 6.29. No perturbations induced by these probes have been observed so far, even it the case of previously problematic permalloy rectangles. On the other hand, these tips provide lower signal than Co and commercial tips (except the supersharp).

6.5.2 Tips with Co coating

All probes from Co series, sputtered with 60 nm Co (on a flat substrate), showed layer thickness on the tip near 15 nm (see Figure 6.30) and had good performance in imaging, which is illustrated in Figures 6.31 and 6.40. Few tip-induced perturbations of the samples, permalloy rectangles in particular, were observed. The problem is similar to the commercial LM probes. Figure 6.32 demonstrates example of EDX spectra from point analysis. Similar observation were made for other probes at different points. In some case element maps were acquired - i.e. the spectrum is

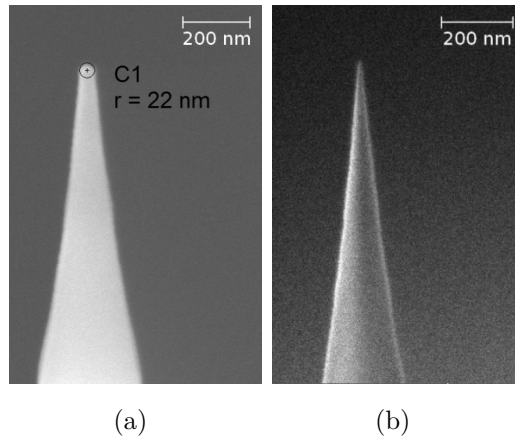(a)   (b)

Fig. 6.28: SEM image of (a) a NiFe probe, (b) a bare AC240TS tip.
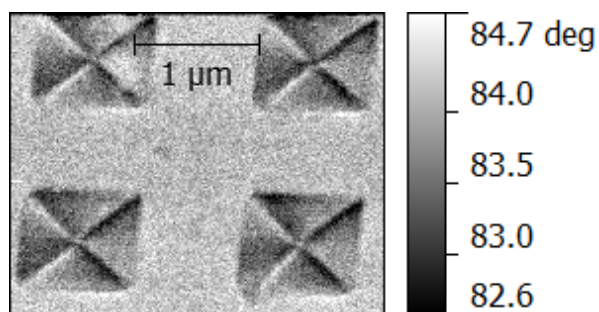
Fig. 6.29: MFM image of magnetic vortices in permalloy diesquares, NiFe probe (layer thickness 12-15 nm), lift 15 nm.

measured at each point of the SEM image. Note that even point spectrum contains informations from larger volume, because of the interacting volume of the primary electrons which forms so called pear.
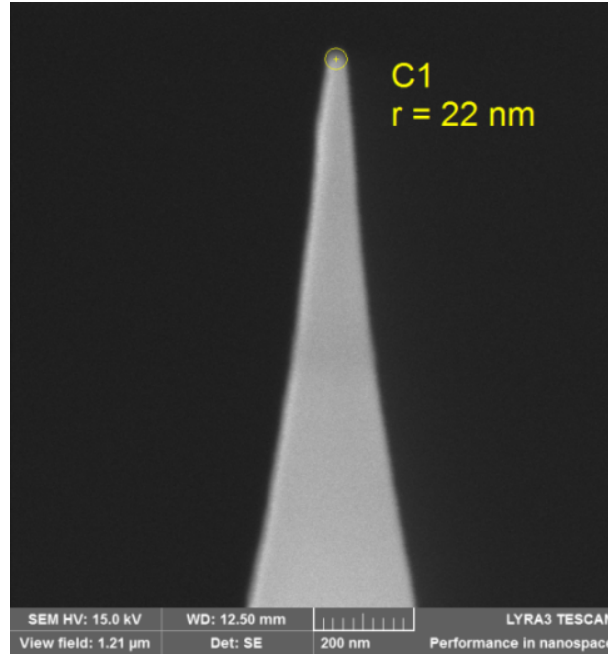
Fig. 6.30: SEM image of a tip after the deposition of 60 nm of Co, resulting layer thickness on the tip is around 15 nm.
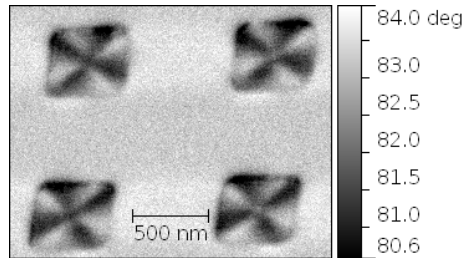
Fig. 6.31: All four possible states of the magnetic vortex in a permalloy diesquare ($500 \times 500 \times 50\,nm^3$) captured by MFM with our Co probe, lift 20 nm.

6.5.3   Tips with CoCr coating

As there were some doubts whether the CoCr target for the deposition is not completely corrupted, the CoCr layer deposited on the flat Si substrate was measured with MOKE. The resulting hysteresis curve is shown in Figure 6.33; in fact it is average of 1000 of acquired loops. As already mentioned, probe for field measurement was unavailable. But in our case the most important information is, that the coating
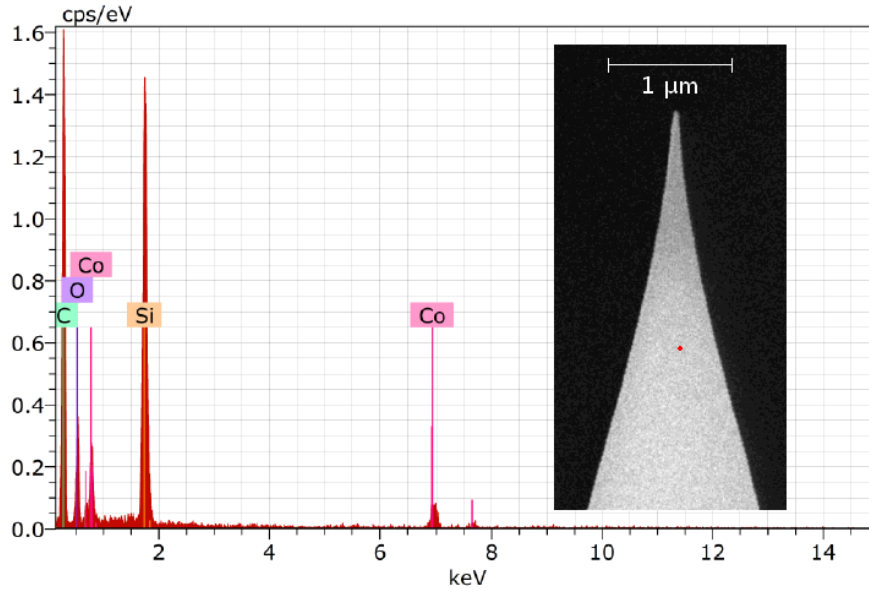
Fig. 6.32: Point EDX spectrum of the Co coated tip. The inset shows the tip and a red dot marks the point of data acquisition. Primary electron beam had energy of 15 keV and both K_α and L_α were tracked. The Co peaks are quite prominent. The tip is made from Si, and the presence of other, contamination elements (C, O), are not a surprise as well.

seems to be in a good state, it is magnetic, and exhibits coercivity 5 times larger than NiFe layers of the same thickness. According to the EDX measurement performed on three CoCr layers at different points and quantification with interactive PB/ZAF method, it seems that the composition is (88 ± 2) at% Co and (12 ∓ 2) at% of Cr.

Although the CoCr coating seems to be all right from the magnetic point of view, problems with the deposition on the AC240TS tips occurred. All three sets of depositions with different thickness (25, 30 and 60 nm on a flat substrate) and slight change in the deposition angle resulted ended with almost no material deposited on the tip apex and bigger cluster can be found just slightly below the apex as demonstrated in Figure 6.34. No similar problems have been observed for the Co coating, thus might be the problem is in Cr content. An adhesion layer may solve the issue. The same problem was once observed also for the NiFe coating.

It is not a surprise that very weak and distorted signal was obtained for all seven prepared probes. In case of two probes another CoCr layer was deposited, so the total CoCr coating would be 25+30=55 nm on a flat substrate, but the real tip coverage is much lower. Still it was possible to image vortex cores with a such, redeposited, probe. However, low lift high of 15 nm had to be used to get sufficient MFM signal. A nice curiosity was imaged with this CoCr tip - so called Pacman-like nanomagnet, which is illustrated in Figure 6.35. The disc on the right in the Fig-
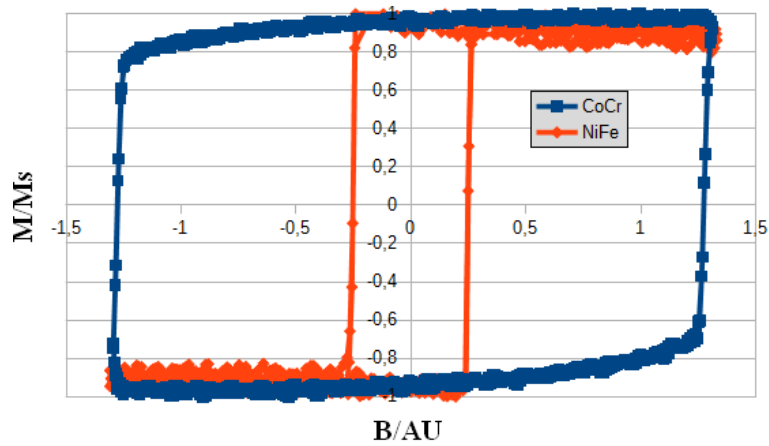
Fig. 6.33: Normalized hysteresis loops of a typical CoCr (blue) and NiFe (red) coating deposited on a flat substrate. The coercivity of CoCr is at least 5 times larger than for NiFe layers, which usually exhibit coercivity of few mT. Babcock [83] measured coercivity of 50 mT for a CoCr coating of similar composition. This fact together with the shape of the CoCr loop suggest that our obtained loop is only a minor (recoil) loop and further measurement in higher fields should be performed.
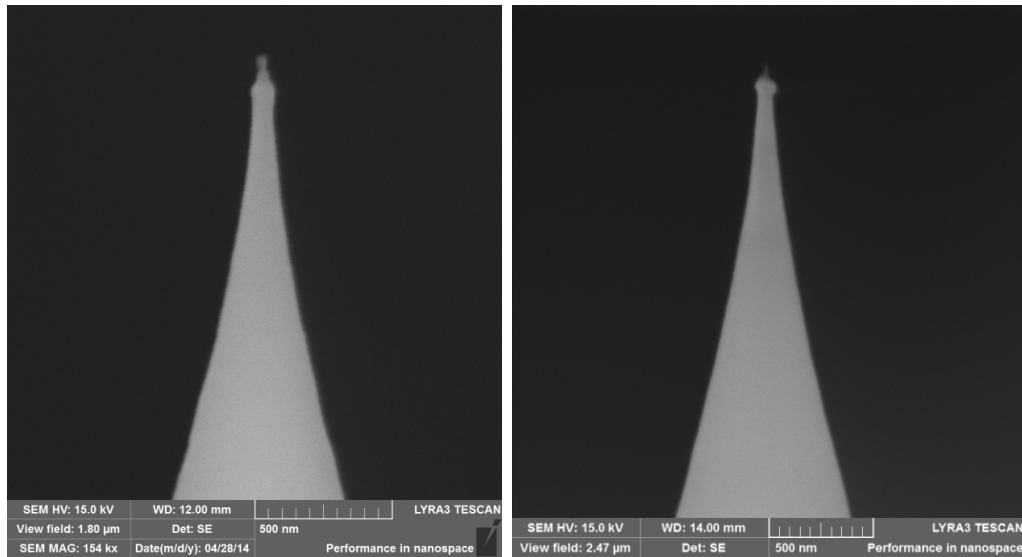
Fig. 6.34: SEM images of the tips with CoCr coating. There is almost no layer on the apex, but slightly below a cluster of deposited material is formed.

ure contains notch, here unmeant defect. This asymmetry influences the magnetic state of the element, which is shown by simulation in Figure 6.36. Processed AFM image served as the input geometry for the simulation. A domain with uniform magnetization in the vicinity of the notch spans towards the disc centre. Dark and bright lines on the *Pacman* in Figure 6.35(b) show edges of the domain area. In our case this is just a curiosity. However, dynamics and switching of state of these Pacmans, asymmetric discs with artificial notches, are widely studied for applications in non-volatile magnetic memories [69, 21].

(a)

(b)
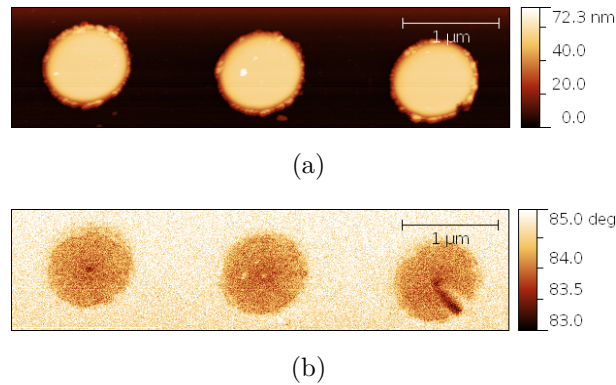
Fig. 6.35: Permalloy discs (thickness 50 nm) hosting magnetic vortices with opposite polarities and Pacman-like nanomagnet imaged with home-coated CoCr tip at 15 nm lift. The right disc contains a notch, this asymmetry influences the magnetic state of the element. (a) topography, (b) MFM.

6.6   Comparison of MFM probes

As we have neither special sample for the determination of the resolution, nor a sufficient number of both commercial and home-coated probes for good statistics, we cannot carry out the proper comparison of the probes. However we can distinguish the probes according to measurement of the same sample under the same or at least very similar conditions. For this testing, the core of the magnetic vortex in permalloy disc with diameter 1 µm and thickness 40 nm was selected as the imaging of the cores is of considerable interest in this work. Images were acquired with different probes at the same lift height of 20 nm for comparison of different commercial probes and 15 nm in case of comparison of our probes with the best commercial ones. We tried to keep at least similar (if not the same) scan size, rate and other parameters. We even intended to image the same disc, but this was not possible for all probes, because the disc was damaged during the experiments. Images are presented as crops from larger images.

(a)   (b)

Fig. 6.36: Simulation of magnetization in a Pacman-like nanomagnet. A domain with uniform magnetization in the vicinity of the notch spans towards the disc centre. Although this is not so obvious in our simulation in (a), it is quite clear in (b) where idealized Pacman was simulated by Šoltýs et al. [69]. Blue and red region corresponds to opposite x components of the magnetization.

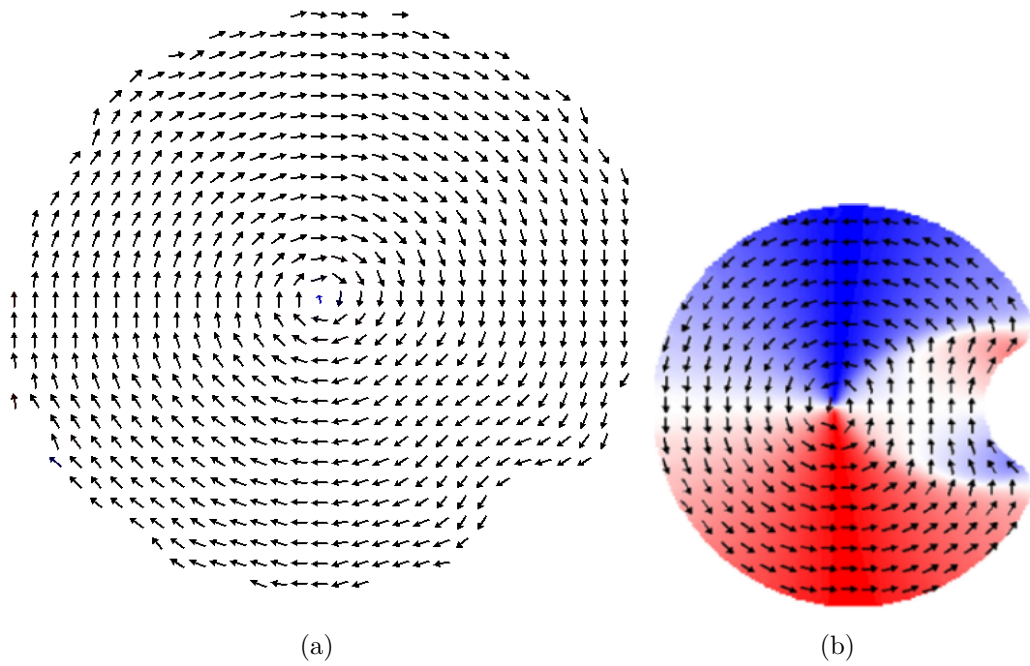From the MFM image (phase shift) we extracted line profile which involves the core. Two main information can be obtained from these profiles - signal strength (phase difference between the disc and the core) and seeming size (full width - half maximum) of the core which tells something about the resolution of the probe. Obviously the smaller 'is' the core, the higher is the resolution. The rather crude comparison is given in Figure 6.37. Note, that the core was not always in the centre of measured area, but it was still near the centre of the disc (slightly to the right of $x = 0.5$ in case of the supersharp). In all cases the phase is lower over the whole disc which corresponds to the overall attraction. The higher is the magnetic coating thickness and magnetic moment, the higher the signal - phase shift between the disc area and the background. When scanning over the core, here with the same magnetization as the tip, the signal is even lower. It is obvious that the highest signal is obtained for the standard tip ($2.1 \pm 0.2°$), then our ($1.2 \pm 0.1°$) and the LM follows ($1.0 \pm 0.1°$). The signal from the supersharp at this lift ($20\,\mathrm{nm}$) is so weak, that the core is almost lost in noise. This tip has to be operated at lower lift heights. The 'width' of the core is similar (approximately $50\,\mathrm{nm}$) in all cases, maybe it is smaller for the supersharp (if one believes that it is really there), which means that the resolution is mainly limited by the lift height.

The signal from our Co probe is is slightly higher than in the case of the LM tip. Although the thickness of our Co coating is even lower than in case of the LM probe, Co has higher saturation and also remanent magnetization than CoCr does. Depending on the particular composition of the CoCr layer, its remanent magnetization and thus magnetic moment can be 2-3 times lower with respect to the Co layer of the same thickness. This limits achievable resolution as well - our Co probes is comparable with the standard one, although there is potential for grading up with the LM probe or even beating it, when using CoCr coating as well. Regrettably, as mentioned above, we have problems with the deposition of CoCr. We have only one redeposited CoCr probe, its performance on the core, now at lift height $15\,\mathrm{nm}$, is given in Figure 6.38 where it is compared with the LM probe at the same lift. Because our CoCr tip is not well covered, the signal is quite low and the LM probe is for sure better. Further optimization is necessary in our case. A buffer layer (Ta, Ti?), which is commonly used both in research and industry, should solve the problem with adhesion of our CoCr coating.

Our NiFe probes provide very low signal even at $15\,\mathrm{nm}$ lift, so thicker coating than $15\,\mathrm{nm}$ (on the tip) should be used for reasonable signal with our instrumentation. On the other hand, no perturbations of soft magnetic samples have been observed with these probes. Figure 6.39 demonstrates MFM observations of two discs with opposite core polarities at lift height of $12\,\mathrm{nm}$. Still the signal is rather weak and almost hidden in the noise.
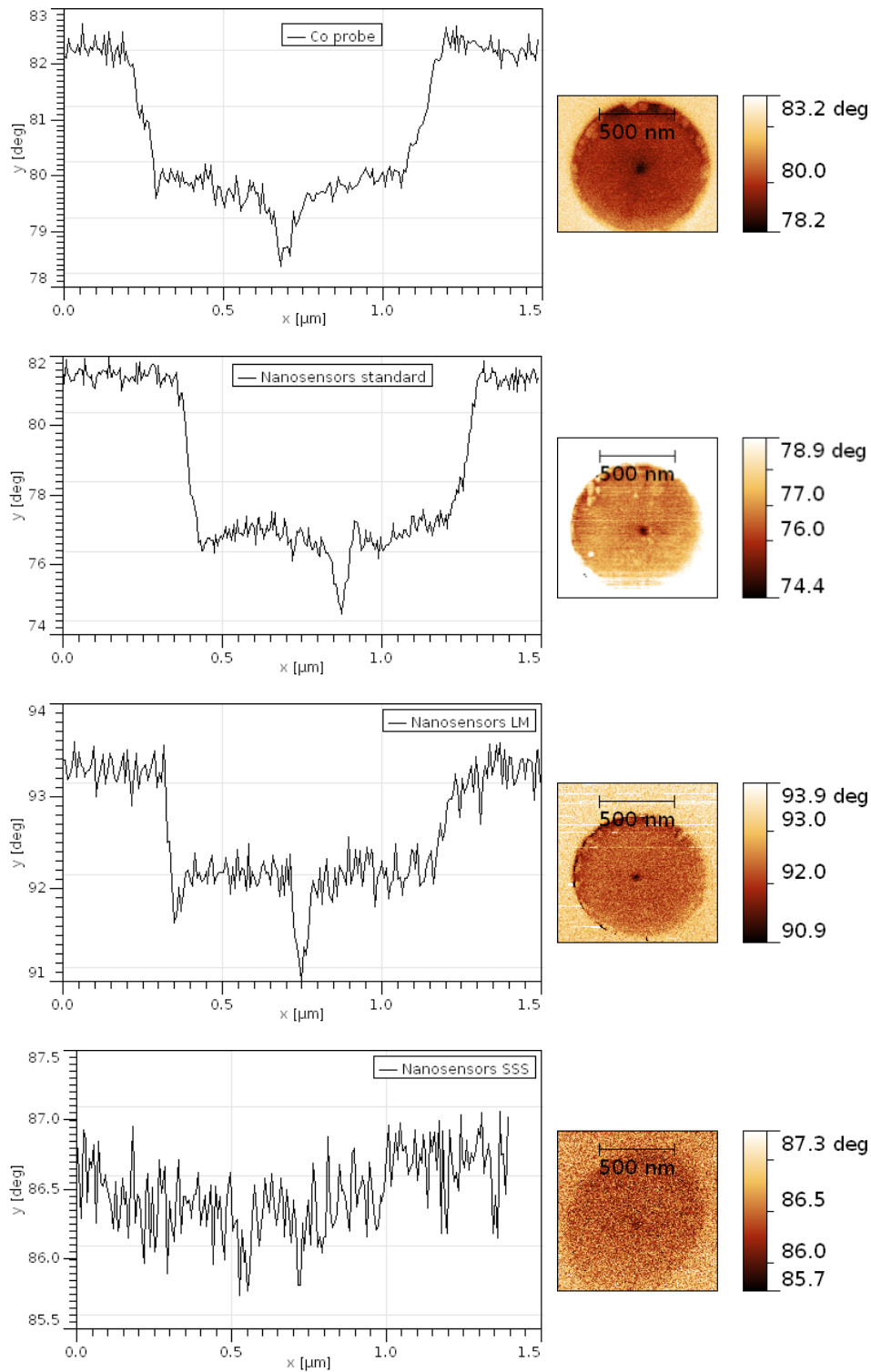
Fig. 6.37: Comparison of Nanosensors probes: standard, low moment (LM) and super-sharp (SSS) with our Co probe. Core of a magnetic vortex in permalloy disc with diameter 1 µm and thickness 40 nm was measured at lift height 20 nm. Left column shows line profiles across the core involving the disc and part of its surrounding. Right column illustrates corresponding MFM image acquired with the probes.
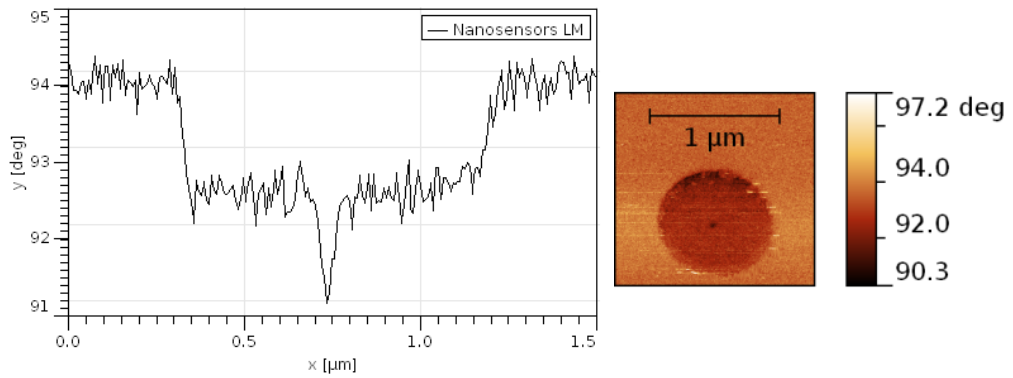
(a)

(b)
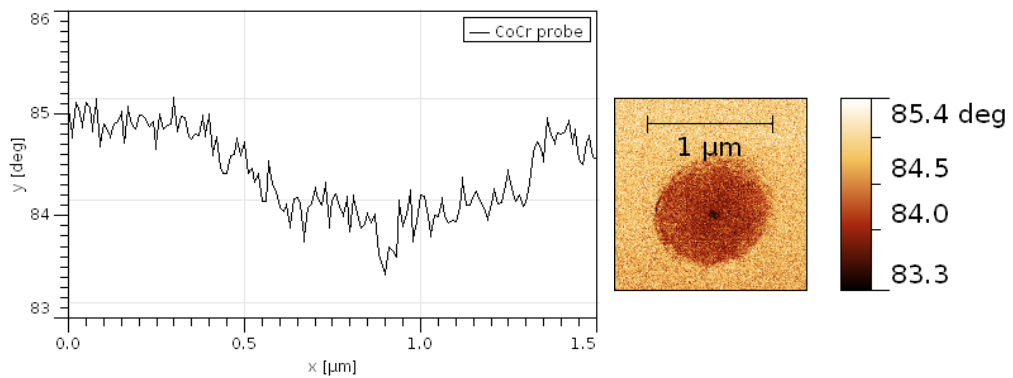
(c)

(d)

Fig. 6.38: Comparison of the commercial LM probe with our not so well covered CoCr probe at lift height of 15 nm. Profile across the core is on the left, whereas the right column illustrates the MFM image of the magnetic disc.

(a)

(b)

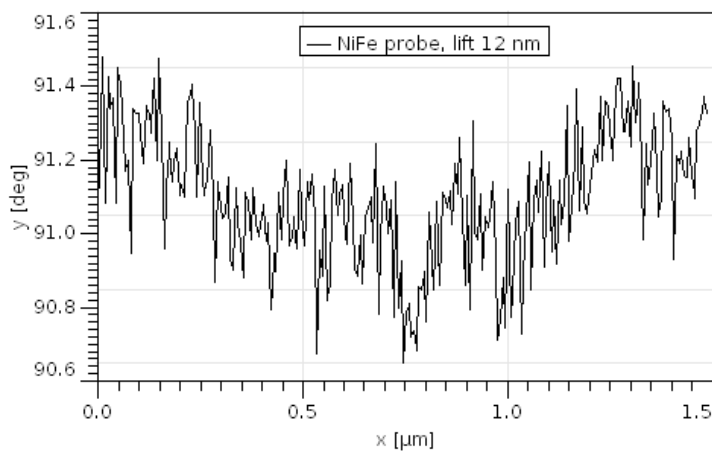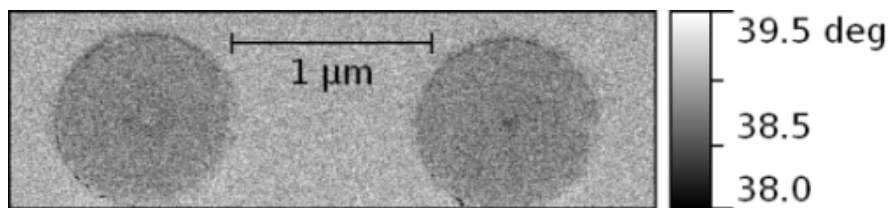*Fig. 6.39: (a) MFM observation of two discs with opposite core polarities with our NiFe probe. The signal is weak and almost hidden in the noise. (b) line profile across the dark core - the disc on the right.*

Comparison of the imaging performance of the commercial Nanosensors supersharp tip and our Co-coated tip on a small permalloy rectangles is given in Figure 6.40. In both cases the diamond state is found in the rectangle. Simply it can be viewed as two magnetic vortices next to each other. The simulated magnetization and its divergence is presented in Figure 6.41.

(a)

(b)
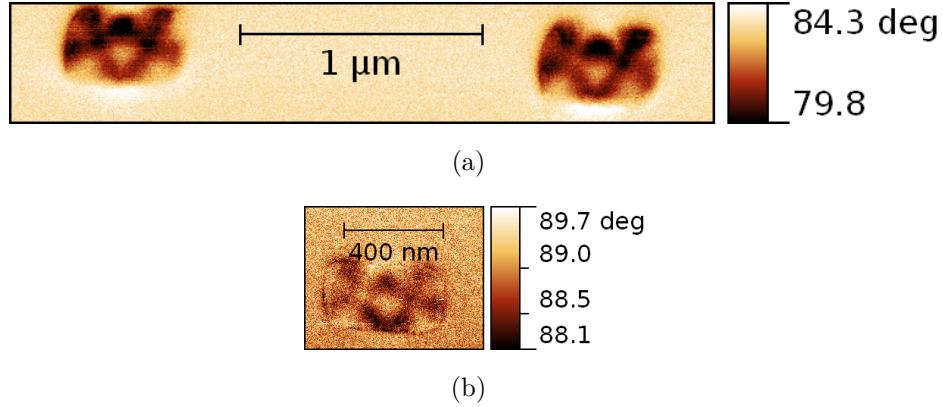
Fig. 6.40: MFM image of small permalloy rectangles ($400 \times 200 \times 40\,nm^3$) obtained with (a) our Co probe (b) commercial Nanosensors supersharp probe. Lift height was $15\,nm$ in both cases. Both images are comparable, even though not all parameters were equal. The supersharp tip could be slightly damaged and the effective lift for our probe was in fact higher - near $20\,nm$ due to the non-magnetic AlO_x spacer on the tip. Still it is obvious that our probe provides stronger signal. The magnetic pattern in rectangles is the diamond state, corresponding simulated image is displayed in Figure 6.41. Note that elements seem to be larger, which is caused by slightly blunt tips (magnetic coating) and long-range interaction. Last, but not least there are really slight deviations of the structures from the ideal case.

6.7 Simulations with the MFM tip

For at least qualitative simulation of the tip-sample interaction we modelled both the tip and the sample. Magnetic wire with a square cross-section serves as the probe. The edge is $12\,nm$ and the length $100\,nm$, initial magnetization of the tip is in $-z$ direction. The sample is magnetic vortex in permalloy diesquare with dimensions $500 \times 500 \times 40\,nm^3$. Commonly, smaller sample are simulated in order to save the computational resources. The magnetization of both the tip and the sample is allowed to change. The tip is positioned over left bottom corner of the sample and the tip-sample separation is $30\,nm$.

The results of the modelling are displayed in Figure 6.42. The magnetization in the sample below the tip is influenced by the tip and it is partially aligned with the magnetization of the tip, which result in the attractive interaction. This change in
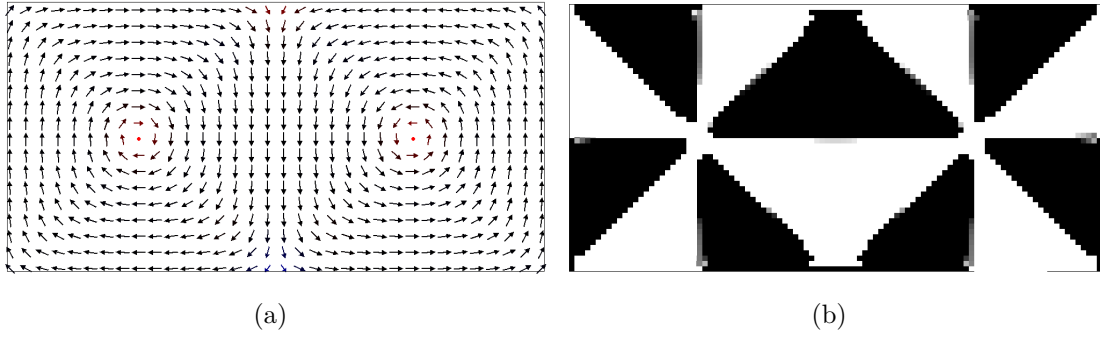
Fig. 6.41: Simulation of the diamond state in the permalloy rectangle from Figure 6.40. (a) magnetization in plane of the rectangle depicted by black arrows and out-of-plane magnetization of the core indicated by red dots. (b) map of magnetic charges. The cell size was 4 nm.

magnetization is reversible and corresponds to the susceptibility contrast and dark background of the samples displayed in the measurements. Similar results were obtained for the Co tip and tip-sample separation of 10 nm.
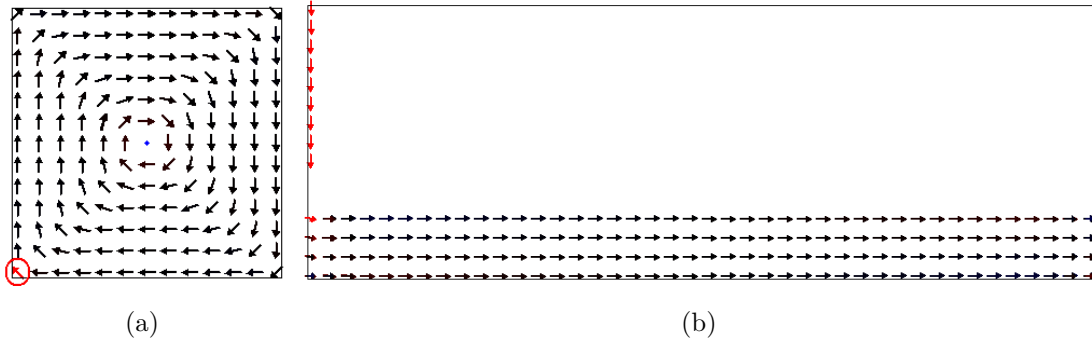
Fig. 6.42: Simulation of the tip-sample interaction with 2 nm cell size. Black arrows show magnetization in-plane of the sample, red and blue ones out-of-plane magnetization ($\pm z$). (a) top-view at mid-plane of the sample ($z = 20$ nm) with the tip position marked by the red circle. (b) side view involving the tip. The magnetization in the sample below the tip is influenced by the tip and it is partially aligned with the magnetization of the tip, which result in the attractive interaction. Note that the contrast is enhanced for the z direction.

7   CONCLUSION AND PERSPECTIVE

In this work we have been concerned with magnetic force microscopy of soft magnetic nanostructures. We have succeeded in fulfilment of the assigned tasks, although only partially in the case of the probe preparation. Systematic preparation and testing of our own magnetic probes was forestalled by the long-term shut down of the main instrument (Kaufman ion beam sputter - deposition apparatus). We even measured the cores of the magnetic vortices in thin permalloy discs with both the commercial and our own home-coated probes, the major goal, even though it was not mentioned explicitly in the official assignment due to an uncertain outcome.

As far as the probe preparation is concerned, we covered Olympus AC240TS AFM probes with both hard (Co, CoCr) and soft (NiFe) magnetic layer. Protective cover layer from AlO_x was deposited in some cases as well. The tips were tested on soft magnetic patterned thin-film elements (discs, 'rectangles').

The Co tips give the highest MFM signal for a given thickness, because Co has the highest saturation and remanent magnetization. Higher signal usually comes together with a deteriorated resolution and higher possibility of perturbations of the sample by the probe. However, Co tips can have similar imaging properties to commercial standard probes with CoCr coating, but with lower thickness of the Co coating compared to the corresponding thickness of the CoCr layer. This results in a sharper tip and therefore better resolution of the probe in topography. All of our Co probes (approximately 15 nm of Co on the tip) were capable of imaging of the cores of the vortices. However, their moment was too high for some other soft magnetic structures - few perturbations were observed in permalloy rectangles. These rectangles seemed to be more sensitive to the tip moment, than the magnetic vortices both in discs and diesquares. The vortices turned out to be quite stable and no tip-induced switching was observed for any of the used probes. The reason might be defects in fabricated structures, rims around the edges in particular.

CoCr coating is the best choice for general applications and commercial probes bear just this coating, even though the particular composition and thickness is a business secret. The commercial LM probes provided the best images of the cores in terms of the sufficient signal and a good resolution. Therefore we wanted to prepare similar probes. Regrettably, all except for one of our depositions resulted in almost no CoCr coating at the tip apex and in most cases the deposited material formed big clusters just below the apex. The CoCr target for deposition seems to be in a good state from the magnetic point of view, but it seems that the problems are caused by wetting of the tip. This might be solved by deposition of a suitable adhesion layer. With our CoCr probe we measured the cores as well and in addition a curiosity was observed, Pacman-like nanomagnet - a disc with a notch. Here it was just a defect,

but similar structures are studied for non-volatile magnetic memories. Despite this success, the signal was low and optimization of the CoCr deposition (with adhesion layer) is required.

Our NiFe probes (10-15 nm NiFe) provided very low signal, but no sample perturbations were observed even for the problematic rectangles. Improvement of the signal might be achieved by increasing the layer thickness. These probes seem to be the best for the observations of really soft nanostructures. On the other hand, a thin CoCr coating with non-magnetic spacer may perform even better.

As for the fabrication of soft magnetic nanostructures, two types of samples were prepared, both from NiFe: Antidot array by deposition of 20 nm NiFe on a nanoporous alumina template and cylindrical nanowires 50 nm in diameter by electrochemical deposition into the nanoporous template. Results of imaging performed on the former turned out to be quite disappointing. The fabricated array had many defects inherited from the template and walls of the array were too thin. Although some signal of magnetic origin was acquired as well, it was full of the topographical contribution and far away from very nice simulation of the array.

The second type of sample, which was prepared and measured during author's research internship at Institut Néel, was much better. Individual bent nanowires more than 10 µm long and 50 nm in diameter with homogeneous chemical composition were prepared by pulsed electrochemical deposition into nanopores of the alumina template. One domain wall was nucleated in the bent part as excepted from our simulation and confirmed by the MFM observations. Soft nanowires are even more susceptible to the tip-induced perturbations, therefore special probes with multilayered $CoCr/Pt/AlO_x$ coating developed at Institut Néel were employed for the imaging. These probes have a very low magnetic moment and better resolution than the commercial probes (maybe except the Nanosensors supersharp probes). To the best of author's knowledge, the only images of DWs in soft NiFe nanowires have been acquired at Institut Néel in the group of Olivier Fruchart, where the author spent his Erasmus internship. Although we were able to image such a DW in a NiFe nanowire, the resolution is not good enough to say which type of DW is in the nanowire. Both types of DWs in nanowires - the transverse and the Bloch point wall - were simulated. From micromagnetic modelling it seems that it might be the BPW, which is preferred for the diameters higher than approximately seven times the dipolar exchange length which is near 35 nm in our case. On the other hand, the nucleation process by transverse magnetic field favours the transverse wall. Last, but not least the energy of both types of DW is not so different for our diameter. Thus, the question of the DW type in our nanowire remains open. It can be determined at synchrotron by the combined XMCD-PEEM technique. Maybe, even

the MFM observation with an extremely low moment probe under vacuum and the ultimate resolution of 10 nm can give the answer.

Last part of the thesis was also devoted to micromagnetic simulations involving modelling of the magnetization and its divergence in measured structures (nanowires, discs, diesquares, rectangles, antidot array). Even though the map of magnetic charges corresponded to the measured MFM image in most cases, we also tried to simulated the tip-sample interaction. Due to the high demand for the computation resources, only preliminary results are presented. Their extension will lead to the simulation of the MFM imaging itself, i.e. involving also mutual tip-sample influence and possible perturbations.

A lot of work has been done, but still much remains to be carried out in the field of MFM at IPE. As for the probe preparation, it is the CoCr adhesion problem and optimization of the tip coating in general. Next step after the imaging of magnetic nanostructures is MFM observation in an external field. A new microscope has been acquired at IPE/CEITEC which should, in principle, enable such measurements. Moreover, the microscope is capable of the torsional resonance imaging, which can be also exploited in its MFM variation for the sensing of the in-plane components of the sample's stray field. In case of the magnetic vortices in discs, this should provide information both on the core polarity (in tapping/lift-mode) and the in-plane circulation (TR-MFM again in lift mode) by acquisition of two subsequent images with the same probe. Only the cantilever excitation would be different for each image.

To conclude, we have prepared MFM tips capable of vortex core imaging and in some cases the perturbation-less observation of soft nanomagnets. Aside from the cores of magnetic vortices, we measured DWs in nanowires and configuration of thin-film elements, mainly rectangles. All measured samples were from the soft NiFe (permalloy in our case). The micromagnetic simulations of magnetic charges, the divergence of the magnetization, are in a good agreement both with the experiments and the theory.

BIBLIOGRAPHY

[1] Everspin technologies, 2014. Available from http://www.everspin.com/, [Accessed 2014-05-29].

[2] Y. Martin and H. K. Wickramasinghe. Magnetic imaging by "force microscopy" with 1000 Å resolution. *Applied Physics Letters*, 50(20):1455–1457, 1987.

[3] G. Binnig, C. F. Quate, and C. Gerber. Atomic force microscope. *Physical Review Letters*, 56(9):930–933, 1986.

[4] L. M. Belova, O. Hellwig, E. Dobisz, and E. D. Dahlberg. Rapid preparation of electron beam induced deposition Co magnetic force microscopy tips with 10 nm spatial resolution. *Review of Scientific Instruments*, 83(9), 2012.

[5] H. Kronmüller and S. Parkin, editors. *Fundamentals and Theory*, volume 1 of *Handbook of Magnetism and Advanced Magnetic Materials*. Wiley, 2007.

[6] É. du Trémolet de LaCheisserie, D. Gignoux, and M. Schlenker, editors. *Magnetism Fundamentals*. Springer, 2005.

[7] S. Blundell. *Magnetism in condensed matter*. Oxford master series in condensed matter physics. Oxford, 2001.

[8] J. Stöhr and H. C. Siegmann, editors. *Magnetism: From Fundamentals to Nanoscale Dynamics*, volume 152 of *Solid-State Sciences*. Springer, 2006.

[9] A. Hubert and R. Schäfer. *Magnetic domains: The Analysis of Magnetic Microstructures*. Springer, 3rd edition, 2009.

[10] A. P. Guimarães. *Principles of Nanomagnetism*. NanoScience and Technology. Springer, 2009.

[11] Lecture notes on nanomagnetism. pdf, 2014. Available from http://perso.neel.cnrs.fr/olivier.fruchart/lectures/nanomagnetism-2014-02-26.pdf, [Accessed 2014-04-10].

[12] D. C. Ralph and M. D. Stiles. Spin transfer torques. *Journal of Magnetism and Magnetic Materials*, 320(7):1190–1216, Nov 2008.

[13] C. D. Hu. The Dzyaloshinskii-Moriya interaction in metals. *Journal of Physics: Condensed Matter*, 24(8):086001, 2012.

[14] J. M. D. Coey. *Magnetism and Magnetic Materials*. Cambridge, 2010.

[15] M. J. Donahue and D. G. Porter. *OOMMF Users's Guide, Version 1.0.* National Institute of Standards and Technology, Gaithersburg, MD, September 1999. Intragency Report NISTIR 6376.

[16] Mini tutorial micromagnetic modelling. Available from http://nmag.soton.ac.uk/nmag/0.2/manual/html/tutorial/doc.html, [Accessed 2013-12-13].

[17] R. F. L. Evans, W. J. Fan, P. Chureemart, T. A. Ostler, M. O. A. Ellis, and R. W. Chantrell. Atomistic spin model simulations of magnetic nanomaterials. *Journal of Physics: Condensed Matter*, 26(10):103202, 2014.

[18] S. Zhang, I. Gilbert, C. Nisoli, G.-W. Chern, M. J. Erickson, L. O'Brien, C. Leighton, P. E. Lammert, V. H. Crespi, and P. Schiffer. Crystallites of magnetic charges in artificial spin ice. *Nature*, 500:553–557, 2013.

[19] A. Fert, V. Cros, and J. Sampaio. Skyrmions on the track. *Nature Nanotechnology*, 8:152–156, 2013.

[20] T. Shinjo, T. Okuno, R. Hassdorf, K. Shigeto, and T. Ono. Magnetic vortex core observation in circular dots of permalloy. *Science*, 289(5481):930–932, 2000.

[21] T. Sato, K. Yamada, and Y. Nakatani. Switching of magnetic vortex core in a pac-man disk using a single field pulse. *Applied Physics Express*, 7(3):033003, 2014.

[22] M. T. Johnson, P. J. H. Bloemen, F. J. A. Den Broeder, and J. J. De Vries. Magnetic anisotropy in metallic multilayers. *Reports on Progress in Physics*, 59(11):1409, 1996.

[23] S. Da Col, S. Jamet, N. Rougemaille, A. Locatelli, T. O. Mentes, B. Santos Burgos, R. Afid, M. Darques, L. Cagnon, J. C. Toussaint, and O. Fruchart. Identification and motion of domain walls in cylindrical nanowires, June 2013. Manuscript.

[24] A. Thiaville, J.M. García, and J. Miltat. Domain wall dynamics in nanowires. *Journal of Magnetism and Magnetic Materials*, 242-245, Part 2(0):1061–1063, 2002. Proceedings of the Joint European Magnetic Symposia (JEMS'01).

[25] A. Thiaville and Y. Nakatani. Domain-wall dynamics in nanowires and nanostrips. In B. Hillebrands and A. Thiaville, editors, *Spin Dynamics in Confined Magnetic Structures III*, volume 101 of *Topics in Applied Physics*, pages 161–205. Springer, 2006.

[26] S. Da-Col, S. Jamet, N. Rougemaille, A. Locatelli, T. O. Mentes, B. Santos Burgos, R. Afid, M. Darques, L. Cagnon, J. C. Toussaint, and O. Fruchart. Observation of Bloch-point domain walls in cylindrical magnetic nanowires. *Physical Review B*, 89:180405, 2014.

[27] R. Hertel. Computational micromagnetism of magnetization processes in nickel nanowires. *Journal of Magnetism and Magnetic Materials*, 249(1-2):251 – 256, 2002. International Workshop on Magnetic Wires.

[28] S. S. P. Parkin, M. Hayashi, and L. Thomas. Magnetic domain-wall racetrack memory. *Science*, 320(5873):190–194, 2008.

[29] P. Landeros, S. Allende, J. Escrig, E. Salcedo, D. Altbir, and E. E. Vogel. Reversal modes in magnetic nanotubes. *Applied Physics Letters*, 90(10):102501, 2007.

[30] J. Bachmann, J. Escrig, K. Pitzschel, J. M. M. Moreno, J. Jing, D. Gorlitz, D. Altbir, and K. Nielsch. Size effects in ordered arrays of magnetic nanotubes: Pick your reversal mode. *Journal of Applied Physics*, 105(7):07B521, 2009.

[31] W. Rave and A. Hubert. Magnetic ground state of a thin-film element. *IEEE Transactions on Magnetics*, 36(6):3886–3899, Nov 2000.

[32] U. Memmert, A. N. Müller, and U. Hartmann. Probes for magnetic force microscopy imaging of soft magnetic samples. *Measurement Science and Technology*, 11(9):1342, 2000.

[33] J. J. Sáenz, N. García, P. Grütter, E. Meyer, H. Heinzelmann, R. Wiesendanger, L. Rosenthaler, H. R. Hidber, and H.-J. Güntherodt. Observation of magnetic forces by the atomic force microscope. *Journal of Applied Physics*, 62(10):4293–4295, 1987.

[34] P. Grutter, D. Rugar, H. J. Mamin, G. Castillo, S. E. Lambert, C.-J. Lin, R. M. Valletta, O. Wolter, T. Bayer, and J. Greschner. Batch fabricated sensors for magnetic force microscopy. *Applied Physics Letters*, 57(17):1820–1822, 1990.

[35] Digital Instruments. *Magnetic Force Microscopy*, 1996. Support Note No. 229, Rev. B.

[36] Olympus micro cantilevers: Medium-soft silicon cantilever, 2014. Available from http://probe.olympus-global.com/en/product/omcl_ac240ts_r3/, [Accessed 2014-04-10].

[37] Atomic force microscopy (afm), 2014. Available from http://www.farmfak.uu.se/farm/farmfyskem/instrumentation/afm.html, [Accessed 2014-05-18].

[38] S. Porthun, L. Abelmann, and C. Lodder. Magnetic force microscopy of thin film media for high density magnetic recording. *Journal of Magnetism and Magnetic Materials*, 182(1-2):238 – 273, 1998.

[39] P. Eaton and P. West. *Atomic Force Microscopy*. Oxford, 2010.

[40] J. Lohau, S. Kirsch, A. Carl, G. Dumpich, and E. F. Wassermann. Quantitative determination of effective dipole and monopole moments of magnetic force microscopy tips. *Journal of Applied Physics*, 86(6):3410–3417, 1999.

[41] A. Hubert, W. Rave, and S. L. Tomlinson. Imaging magnetic charges with magnetic force microscopy. *Physica Status Solidi (B)*, 204(2):817–828, 1997.

[42] A. Thiaville, J. Miltat, and J. M. García. Magnetic force microscopy: Images of nanostructures and contrast modeling. In H. Hopster and H. P. Oepen, editors, *Magnetic Microscopy of Nanostructures*, NanoScience and Technology, pages 225–251. Springer, 2005.

[43] Z. Khan, C. Leung, B. A. Tahir, and B. W. Hoogenboom. Digitally tunable, wide-band amplitude, phase, and frequency detection for atomic-resolution scanning force microscopy. *Review of Scientific Instruments*, 81:073704, 2010.

[44] H. J. Mamin, D. Rugar, J. E. Stern, R. E. Fontana Jr., and P. Kasiraj. Magnetic force microscopy of thin permalloy films. *Applied physics letters*, 55(3):318–320, 1989.

[45] S. Foss, R. Proksch, E. D. Dahlberg, B. Moskowitz, and B. Walsh. Localized micromagnetic perturbation of domain walls in magnetite using a magnetic force microscope. *Applied Physics Letters*, 69(22):3426–3428, 1996.

[46] J. M. García, A. Thiaville, and J. Miltat. MFM imaging of nanowires and elongated patterned elements. *Journal of Magnetism and Magnetic Materials*, 249(1-2):163 – 169, 2002. International Workshop on Magnetic Wires.

[47] R. D. Gomez, T. V. Luu, A. O. Pak, K. J. Kirk, and J. N. Chapman. Domain configurations of nanostructured permalloy elements. *Journal of Applied Physics*, 85(8):6163–6165, 1999.

[48] J. M. García, A. Thiaville, J. Miltat, K. J. Kirk, and J. N. Chapman. MFM imaging of patterned permalloy elements under an external applied field. *Journal of Magnetism and Magnetic Materials*, 242-245, Part 2:1267 – 1269, 2002. Proceedings of the Joint European Magnetic Symposia (JEMS'01).

[49] J. M. García-Martín, A. Thiaville, J. Miltat, T. Okuno, L. Vila, and L. Piraux. Imaging magnetic vortices by magnetic force microscopy: experiments and modelling. *Journal of Physics D: Applied Physics*, 37(7):965, 2004.

[50] M. Kleiber, F. Kümmerlen, M. Löhndorf, A. Wadas, D. Weiss, and R. Wiesendanger. Magnetization switching of submicrometer Co dots induced by a magnetic force microscope tip. *Physical Review B*, 58(9):5563–5567, 1998.

[51] X. Zhu, P. Grütter, V. Metlushko, and B. Ilic. Systematic study of magnetic tip induced magnetization reversal of e-beam patterned permalloy particles. *Journal of Applied Physics*, 91(10):7340–7342, 2002.

[52] V. Cambel, P. Eliáš, D. Gregušová, J. Martaus, J.Fedor, G. Karapetrov, and V. Novosad. Magnetic elements for switching magnetization magnetic force microscopy tips. *Journal of Magnetism and Magnetic Materials*, 322:2715–2721, 2010.

[53] V. Cambel, M. Precner, J. Fedor, J. Šoltýs, J. Tóbik, T. Šepka, and G. Karapetrov. High resolution switching magnetization magnetic force microscopy. *Applied Physics Letters*, 102:062405, 2013.

[54] J. W. Li, J. P. Cleveland, and R. Proksch. Bimodal magnetic force microscopy: Separation of short and long range forces. *Applied Physics Letters*, 94(16), 2009.

[55] T. Kasai, B. Bhushan, L. Huang, and C. Su. Topography and phase imaging using the torsional resonance mode. *Nanotechnology*, 15(7):731–742, 2004.

[56] A. Kaidatzis and J. M. García-Martín. Torsional resonance mode magnetic force microscopy: enabling higher lateral resolution magnetic imaging without topography-related effects. *Nanotechnology*, 24(16):165704, 2013.

[57] P. Grütter, Y. Liu, P. LeBlanc, and U. Dürig. Magnetic dissipation force microscopy. *Applied Physics Letters*, 71(2):279–281, 1997.

[58] R. Proksch, K. Babcock, and J. Cleveland. Magnetic dissipation microscopy in ambient conditions. *Applied Physics Letters*, 74(3):419–421, 1999.

[59] B. Torre, G. Bertoni, D. Fragouli, A. Falqui, M. Salerno, A. Diaspro, R. Cingolani, and A. Athanassiou. Magnetic force microscopy and energy loss imaging of superparamagnetic iron oxide nanoparticles. *Scientific Reports*, 1:202, 2011.

[60] R. Wiesendanger, D. Bürgler, G. Tarrach, A. Wadas, D. Brodbeck, H. J. Güntherodt, G. Güntherodt, R. J. Gambino, and R. Ruf. Vacuum tunneling of spin-polarized electrons detected by scanning tunneling microscopy. *Journal of Vacuum Science & Technology B*, 9(2):519–524, 1991.

[61] U. Kaiser, A. Schwarz, and R. Wiesendanger. Magnetic exchange force microscopy with atomic resolution. *Nature*, 446(7135):522–525, 2007.

[62] T. Yamaoka, K. Watanabe, Y. Shirakawabe, K. Chinone, E. Saitoh, M. Tanaka, and H. Miyajima. Applications of high-resolution MFM system with low-moment probe in a vacuum. *IEEE Transactions on Magnetics*, 41(10):3733–3735, Oct 2005.

[63] Y. Seo, P. Cadden-Zimansky, and V. Chandrasekhar. Low-temperature high-resolution magnetic force microscopy using a quartz tuning fork. *Applied Physics Letters*, 87(10):103103, 2005.

[64] NT-MDT. *Six essentials of high-quality MFM*, 2008. Available from http://www.ntmdt.com/data/media/files/applications/six_essentials_of-_mfm.pdf, [Accessed 2014-05-18].

[65] M. Jaafar, O. Iglesias-Freire, L. Serrano-Ramón, M. R. Ibarra, J. M. de Teresa, and A. Asenjo. Distinguishing magnetic and electrostatic interactions by a Kelvin probe force microscopy - magnetic force microscopy combination. *Beilstein Journal of Nanotechnology*, 2:552–560, 2011.

[66] J. Raabe, R. Pulwey, R. Sattler, T. Schweinböck, J. Zweck, and D. Weiss. Magnetization pattern of ferromagnetic nanodisks. *Journal of Applied Physics*, 88(7):4437–4439, 2000.

[67] T. Okuno, K. Shigeto, T. Ono, K. Mibu, and T. Shinjo. MFM study of magnetic vortex cores in circular permalloy dots: behavior in external field. *Journal of Magnetism and Magnetic Materials*, 240(1-3):1–6, 2002. 4th International Symposium on Metallic Multilayers.

[68] M. Jaafar, R. Yanes, D. Perez de Lara, O. Chubykalo-Fesenko, A. Asenjo, E. M. Gonzalez, J. V. Anguita, M. Vazquez, and J. L. Vicent. Control of the

chirality and polarity of magnetic vortices in triangular nanodots. *Physical Review B*, 81:054439, 2010.

[69] J. Šoltýs, Š. Gaži, J. Fedor, J. Tóbik, M. Precner, and V. Cambel. Magnetic nanostructures for non-volatile memories. *Microelectronic Engineering*, 110:474 – 478, 2013.

[70] S. H. Liou, R. F. Sabiryanov, S. S. Jaswal, J. C. Wu, and Y. D. Yao. Magnetic domain patterns of rectangular and elliptic arrays of small permalloy elements. *Journal of Magnetism and Magnetic Materials*, 226-230, Part 2(0):1270 – 1272, 2001. Proceedings of the International Conference on Magnetism (ICM 2000).

[71] S. Felton, K. Gunnarsson, P. E. Roy, P. Svedlindh, and A. Quist. MFM imaging of micron-sized permalloy ellipses. *Journal of Magnetism and Magnetic Materials*, 280(2-3):202–207, 2004.

[72] S. Getlawi, M. R. Koblischka, U. Hartmann, C. Richter, and T. Sulzbach. Patterning of permalloy thin films by means of electron-beam lithography and focused ion-beam milling. *Superlattices and Microstructures*, 44(4-5):699 – 704, 2008. E-MRS 2007 Symposium K-Nanoscale Self-Assembly and Patterning.

[73] K. Shigeto, T. Okuno, K. Mibu, T. Shinjo, and T. Ono. Magnetic force microscopy observation of antivortex core with perpendicular magnetization in patterned thin film of permalloy. *Applied Physics Letters*, 80(22):4190–4192, 2002.

[74] K. Sato, T. Yamamoto, T. Tezuka, T. Ishibashi, Y. Morishita, A. Koukitu, K. Machida, and T. Yamaoka. MFM observation of spin structures in nano-magnetic-dot arrays fabricated by damascene technique. *Journal of Magnetism and Magnetic Materials*, 304(1):10–13, 2006.

[75] L. Belliard, J. Miltat, A. Thiaville, S. Dubois, J. L. Duvail, and L. Piraux. Observing magnetic nanowires by means of magnetic force microscopy. *Journal of Magnetism and Magnetic Materials*, 190(1-2):1–16, 1998.

[76] Y. Henry, K. Ounadjela, L. Piraux, S. Dubois, J.-M. George, and J.-L. Duvail. Magnetic anisotropy and domain patterns in electrodeposited cobalt nanowires. *The European Physical Journal B - Condensed Matter and Complex Systems*, 20(1):35–54, 2001.

[77] T. Wang, Y. Wang, Y. Fu, T. Hasegawa, F. S. Li, H. Saito, and S. Ishio. A magnetic force microscopy study of the magnetic reversal of a single Fe nanowire. *Nanotechnology*, 20(10):105707, 2009.

[78] A. Schwarz and R. Wiesendanger. Magnetic sensitive force microscopy. *Nano Today*, 3(1-2):28 – 39, 2008.

[79] H. Hopster and H. P. Oepen, editors. *Magnetic Microscopy of Nanostructures*, volume XVIII of *NanoScience and Technology*. Springer, 2005.

[80] P. Fischer, M.-Y. Im, and B. L. Mesler. *High-Resolution Soft X-Ray Microscopy for Imaging Nanoscale Magnetic Structures and Their Spin Dynamics*, pages 7–37. Wiley, 2010.

[81] O. Fruchart. TEM for magnetism: challenges and competitors, 2013. Available from http://perso.neel.cnrs.fr/olivier.fruchart/slides/tech/tech-fruchart-magnmicro2013.pdf, [Accessed 2014-05-19].

[82] M. Futamoto, T. Hagami, S. Ishihara, K. Soneta, and M. Ohtake. Improvement of magnetic force microscope resolution and application to high-density recording media. *IEEE Transactions on Magnetics*, 49(6):2748–2754, 2013.

[83] K. Babcock, V. Elings, M. Dugas, and S. Loper. Optimization of thin-film tips for magnetic force microscopy. *IEEE Trans. Magn.*, 30(6):4503–4505, November 1994.

[84] C. Hyun, A. K. H. Lee, and A. de Lozanne. Focused ion beam deposition of $Co_{71}Cr_{17}Pt_{12}$ and $Ni_{80}Fe_{20}$ on tips for magnetic force microscopy. *Nanotechnology*, 17(3):921–925, 2006.

[85] O. Cespedes, A. Luu, F. M. F. Rhen, and J. M. D. Coey. Fabrication of magnetic force microscopy tips via electrodeposition and focused ion beam milling. *IEEE Transactions on Magnetics*, 44(11):3248–3251, Nov 2008.

[86] M. Rolandi, D. Okawa, S. A. Backer, A. Zettl, and J. M. J. Fréchet. Fabrication of magnetic force microscopy probes via localized electrochemical deposition of cobalt. *Journal of Vacuum Science & Technology B*, 25(5):L39–L42, 2007.

[87] F. Wolny, T. Mühl, U. Weissker, K. Lipert, J. Schumann, A. Leonhardt, and B. Büchner. Iron filled carbon nanotubes as novel monopole-like sensors for quantitative magnetic force microscopy. *Nanotechnology*, 21(43):435501, 2010.

[88] Z. Deng, E. Yenilmez, J. Leu, J. E. Hoffman, E. W. J. Straver, H. Dai, and K. A. Moler. Metal-coated carbon nanotube tips for magnetic force microscopy. *Applied Physics Letters*, 85(25):6263–6265, 2004.

[89] G. Yang, J. Tang, S. Kato, Q. Zhang, L. C. Qin, M. Woodson, J. Liu, J. W. Kim, P. T. Littlehei, C. Park, and O. Zhou. Magnetic nanowire based high

resolution magnetic force microscope probes. *Applied Physics Letters*, 87(12), 2005.

[90] S. H. Liou. Comparison of magnetic images using point and thin-film magnetic force microscopy tips. *IEEE Transactions on Magnetics*, 35(5):3989–3991, 1999.

[91] S.-H. Liou. Advanced magnetic force microscopy tips for imaging domains. In Y. Liu, D. J. Sellmyer, and D. Shindo, editors, *Handbook of Advanced Magnetic Materials*, pages 374–396. Springer, 2006.

[92] P. F. Hopkins, J. Moreland, S. S. Malhotra, and S. H. Liou. Superparamagnetic magnetic force microscopy tips. *Journal of Applied Physics*, 79(8):6448–6450, 1996.

[93] N. Amos, R. Fernandez, R.M. Ikkawi, M. Shachar, J. Hong, B. Lee, D. Litvinov, and S. Khizroev. Ultrahigh coercivity magnetic force microscopy probes to analyze high-moment magnetic structures and devices. *IEEE Magnetics Letters*, 1:6500104–6500104, 2010.

[94] M. Ohtake, K. Soneta, and M. Futamoto. Influence of magnetic material composition of $Fe_{1-x}B_x$ coated tip on the spatial resolution of magnetic force microscopy. *Journal of Applied Physics*, 111(7), 2012.

[95] Liou and Sy-Hwang. Advanced magnetic force microscopy tips for imaging domains. In Y. Liu, D. J. Sellmyer, and D. Shindo, editors, *Handbook of Advanced Magnetic Materials*, pages 374–396. Springer, 2006.

[96] K. Nagano, K. Tobari, M. Ohtake, and M. Futamoto. Effect of magnetic film thickness on the spatial resolution of magnetic force microscope tips. *Journal of Physics: Conference Series*, 303(1):012014, 2011.

[97] L. Folks and R. C. Woodward. The use of MFM for investigating domain structures in modern permanent magnet materials. *Journal of Magnetism and Magnetic Materials*, 190(1-2):28–41, 1998.

[98] A. Carl, J. Lohau, S. Kirsch, and E. F. Wassermann. Magnetization reversal and coercivity of magnetic-force microscopy tips. *Journal of Applied Physics*, 89(11):6098–6104, 2001.

[99] ASYMFMLM, 2014. Available from http://www.asylumresearch.com/-Probe/ASYMFMLM,Asylum, [Accessed 2014-04-17].

[100] MESP - Bruker AFM Probes, 2014. Available from http://www.brukerafmprobes.com/p-3309-mesp.aspx, [Accessed 2014-04-17].

[101] Magnetic force microscopy silicon-mfm-probes, 2007. Available from http://www.nanosensors.com/pdf/Magnetic_Force_Microscopy.pdf, [Accessed 2014-02-27].

[102] J. Babocký. *Creation of plasmonic micro- and nanostructures by electron beam lithography.* Bachelor's thesis. Brno University of Technology, Faculty of Mechanical Engineering, 2012. Supervised by Ing. Michal Kvapil, [in Czech].

[103] S. M. George. Atomic layer deposition: An overview. *Chemical Reviews*, 110(1):111–131, 2010.

[104] M. Staňo. *Fabrication of nanowires into porous alumina by electrolysis.* Bachelor's thesis. Brno University of Technology, Faculty of Mechanical Engineering, 2012. Supervised by Ing. David Škoda, Ph.D., [in Czech].

[105] M. S. Salem, P. Sergeliusand, R. Zierold, J. M. M. Moreno, D. Gorlitz, and K. Nielsch. Magnetic characterization of nickel-rich NiFe nanowires grown by pulsed electrodeposition. *Journal of Materials Chemistry*, 22:8549–8557, 2012.

[106] M. Pavera. Automation and control of multilayers deposition by IBS/IBAD. Master's thesis, Brno University of Technology, Faculty of Mechanical Engineering, 2011. Supervised by Ing. Michal Urbánek, Ph.D., [in Czech].

[107] O. Fruchart, A. Masseboeuf, J. C. Toussaint, and P. Bayle-Guillemaud. Growth and micromagnetism of self-assembled epitaxial fcc(111) cobalt dots. *Journal of Physics: Condensed Matter*, 25(49):496002, 2013.

[108] AFM tips PPP-FMR - NANOSENSORS, 2014. Available from http://www.nanosensors.com/PointProbe-Plus-Force-Modulation-Mode-Reflex-Coating-afm-tip-PPP-FMR, [Accessed 2014-04-10].

[109] L. Flajšman. *Design of the apparatus for the measurement of the magnetic properties of the micro and nanostructures.* Bachelor's thesis. Brno University of Technology, Faculty of Mechanical Engineering, 2013. Supervised by prof. RNDr. Jiří Spousta, Ph.D., [in Czech].

[110] Š. Višňovský. *Optics in Magnetic Multilayers and Nanostructures.* Optical Science and Engineering. CRC Press, 2006.

[111] P. Fischer, M.-Y. Im, S. Kasai, K. Yamada, T. Ono, and A. Thiaville. X-ray imaging of vortex cores in confined magnetic structures. *Physical Review B*, 83:212402, 2011.

LIST OF ABBREVIATIONS

AFM Atomic Force Microscopy

ALD Atomic Layer Deposition

BPW Bloch Point Wall (domain wall in a nanowire)

CE Counter Electrode

CEITEC Central European Institute of Technology

CNRS Centre Nationale de la Recherche Scientific

DC Direct Current (also static mode)

DW Domain Wall

EBL Electron Beam Lithography

EDX Energy-Dispersive X-ray spectroscopy

FD Finite Difference

FE Finite Element

FIB Focused Ion Beam

HDD Hard Disc Drive

IBS Ion Beam Sputter deposition

IPA IsoPropyl Alcohol

IPE Institute of Physicsl Engineering

KPFM Kelvin Probe Force Microscopy

LLG Landau-Lifschitz-Gilbert (equation)

LM Low (magnetic) Moment

MFM Magnetic Force Microscopy

MOKE MagnetoOptical Kerr Effect

MTXM Magnetic Transmission X-Ray Microscopy

NW NanoWire

OOMMF Object Oriented MicroMagnetic Framework

PEEM PhotoEmission Electron Microscopy

RE Reference Electrode

SCE Saturated Calomel Electrode

SEM Scanning Electron Microscopy

SEMPA Scanning Electron Microscopy with Polarization Analysis

SP-STM Spin-Polarized Scanning Tunnelling Microscopy

STXM Scanning Transmission X-Ray Microscopy

TEM Transmission Electron Microscopy

TW Transverse Wall (domain wall in a nanowire)

vdW van der Waals (interaction/force)

WE Working Electrode

XMCD Xray-Magnetic Circular Dichroism